Politecnico di Milano
Department of Physics
School of Industrial and Information Engineering
Master of Science in Engineering Physics

Characterization of a biomolecular source for attosecond pump-probe experiments

Supervisor:
Prof. Mauro Nisoli
Assistant Supervisor:
Dr. Rocío Borrego-Varillas

Author:
Gaspare Esposito
Matr. 899447

Academic Year 2019 - 2020

costruire è sapere, e potere,
rinunciare alla perfezione

– Niccolò Fabi

Contents

List of Figures

List of Tables

Abstract

Advances in ultrafast optics opened the possibility to experimentally access elementary molecular processes which, previously, could only be described by infering them from the final results of chemical reactions or perturbations. Femtosecond spectroscopies intend to follow real-time ultrafast nuclear dynamics. At a more fundamental level, the timescale relevant for processes at the atomic or molecular level is set by the motion of electrons. After the first experiment in which it was demonstrated the possibility of directly controlling electron localization inside a H_2 molecule on an attosecond timescale, the question that naturally arises if it can be extended to more complex molecules. Within this perspective, important efforts have been put into the understanding of a purely electron dynamics called *charge migration*. The application of attosecond methods to bio-relevant molecules may have tremendous applications in the transport of biological signals or molecular electronics.
In this context, I have worked on the characterization of a two-colour XUV-NIR pump-probe setup for attosecond spectroscopy. In particular, during this thesis I focused on the design of a molecular source able to generate gas-phase molecules and carry them to the interaction region inside a VMI spectrometer, where a static potential flies photofragments towards a detector where their mass spectrum is acquired. In addition, an upgrade of the beamline has been done to get a control over the stability of the XUV-NIR pulses delay up to a few tens of attoseconds.
This work consisted of the following tasks: (i) implementation of the molecular source; (ii) synchronization of the different signals triggering the electronics for the generation of the molecular beam and the mass spectra acquisition; (iii) characterization of the emission of the source and development of a technique to find the temporal overlap between the XUV and NIR pulses. Finally, preliminary mass spectra have been acquired and analyzed, also with the help of a simulation software in order to interpret the data.

Sommario

I progressi nel campo dell'ottica ultraveloce hanno aperto la possibilità di accedere sperimentalmente a processi molecolari elementari che, in precedenza, potevano solo essere dedotti dal risultato finale di reazioni chimiche o perturbazioni. Lo scopo della spettroscopia a femtosecondi è quello di seguire in tempo reale le dinamiche nucleari ultraveloci. Ad un livello più essenziale, la scala temporale rilevante per processi che avvengono a livello atomico o molecolare è regolata dal movimento degli elettroni. Dopo la prima evidenza sperimentale della possibilità di controllare direttamente, in una molecola di H_2, la localizzazione dell'elettrone nella scala degli attosecondi, ci si è chiesto se questa possibilità potesse essere estesa a molecole più complesse. In questa prospettiva, sono stati messi in atto importanti sforzi nella comprensione di una dinamica puramente elettronica chiamata *charge migration*. L'applicazione di tecniche ad attosecondi a molecole di interesse biologico potrebbe aprire la porta ad importantissime applicazioni nell'ambito del trasporto di segnali biologici o nel campo dell'elettronica molecolare.
In questo contesto, ho lavorato alla caratterizzazione di un setup per esperimenti di spettroscopia pump-probe XUV-NIR con risoluzione temporale ad attosecondi. In particolare, durante questa tesi mi sono concentrato sulla progettazione di una sorgente molecolare in grado di generare molecole in fase gassosa e portarle nella regione di interazione all'interno di uno spettrometro VMI, in cui un potenziale statico accelera i fotoframmenti verso un rivelatore dove viene acquisito il loro spettro di massa. Inoltre, mi sono occupato dell'ottimizzazione della linea per ottenere un controllo sulla stabilità del ritardo tra gli impulsi XUV-NIR fino a poche decine di attosecondi.
Questo lavoro si è articolato nei seguenti obiettivi: (i) l'implementazione della sorgente molecolare; (ii) la sincronizzazione dei diversi segnali che innescano la generazione del fascio molecolare e l'acquisizione degli spettri di massa; (iii) la caratterizzazione dell'emissione della sorgente molecolare e la ricerca di una tecnica per trovare la sovrapposizione temporale tra gli impulsi XUV e NIR. Infine, sono stati acquisiti spettri di massa preliminari, anche con l'aiuto di un software di simulazione per l'interpretazione dei dati.

Introduction

Attosecond pulses were first employed for the investigation of electron dynamics in atoms reporting important applications as the measurements of Auger relaxation and the real time observation of valence electron motion in krypton, the characterization of wave packets in helium, the measurement of delays in photoemission. The first application of attosecond pump-probe spectroscopy in molecules appeared in 2006, when the control of bound electron motion in D_2 by an infrared (IR) electric field was demonstrated; only a few years later, attosecond pulses were combined with IR fields to control the localization of the electronic charge distribution in H_2 and D_2 molecules and more recently the attosecond electronic-nuclear coupling dynamics in the dissociative ionization of H_2 were disclosed. These pioneering works opened the way to investigate many-electron diatomic and small polyatomic molecules, leading to important achievements such as the observation and control of the attosecond electron dynamics in CO, CO_2, O_2, C_2H_4, N_2O, H_2O and N_2 or the measurement of charge migration in phenylalanine. Due to the low photon flux of the attosecond pulses obtained by HHG, a typical time-resolved experiment uses an XUV attosecond pulse in combination with an intense few-cycle IR pulse. The detection scheme is based on the measurement of an observable such as the absorption of the XUV pulse (Attosecond Transient Absorption Spectroscopy), the fragments ions (Mass Spectroscopy) or the kinetic energy of the ejected electrons (Photoelectron Spectroscopy). XUV-pump/IR-probe approach preserves the temporal resolution while compensating for the weak intensity of the attosecond XUV pulse. In an XUV-pump/IR-probe experiment, the XUV pulse usually creates a coherent superposition of cationic states which drives a dynamics in the attosecond time scale. The probe pulse role in these experiments is to interfere with a system whose dynamics has been triggered by the pump pulse and is governed by the mechanisms whose laws are object of the purpose of the experiment.
One of the bottlenecks that is faced by this kind of technique is a precise control of the pump-probe delay due to the extreme temporal resolution that is required. A further challenging task is to transfer molecules into the gas

phase, given that XUV pulses require vacuum technology. During my thesis work, we have implemented a source which relies on the evaporation of sample molecules from a porous graphite powder matrix and a supersonic noble gas jet to carry them into the spectrometer chamber.
This thesis work presents the main characteristics of the setup and the preliminary results which have been achieved in order to characterize it and it is structured as follows.

Chapter One: Attosecond Spectroscopy
The first chapter is devoted to the description of two physical phenomena: the first, High-order Harmonics Generation (HHG) is useful to produce sub-fs XUV light pulses; the second, charge migration, is a useful model to describe the ultrafast electron dynamics happening in molecules the first instants after ionization. Moreover, a review of the main attosecond pump-probe experiments on molecules reported in the literature is presented.

Chapter Two: Beamline
In this chapter the beamline of the ELYCHE laboratory is presented, with a special focus on the XUV-NIR interferometer and on the VMI spectrometer.

Chapter Three: Biomolecular Source
A detailed description of the molecular source which has been mounted on the VMI spectrometer. Particular attention is paid to the design of the new oven used to evaporate molecules.

Chapter Four: Characterization of the BioSource
In this chapter the main steps through which the setup has been installed and optimized is presented. Its characterization in terms of the temporal profile of the molecular gas emission, the temporal overlap between the pump and probe pulses and the acquisition of preliminary mass spectra is presented.

Conclusions and Future Perspectives
Lastly, the main conclusions of this thesis work is presented, together with some future goals this setup has been built for.

Chapter 1

Attosecond Spectroscopy

1.1 High-Order Harmonics Generation

Time-resolved spectroscopy pushing to very short temporal scales requires light pulses which can be able to take a "snapshot" of a system with a temporal resolution as short as the required temporal scale. Reaching the attosecond time scale with a laser light pulse is not an easy task, and it required the development of a specific experiment. The purpose of this section is to present one simple theoretical model which explains this experimental tool, highlighting the properties of the resulting laser pulses.

1.1.1 Introduction

Combining the coherence and spectral properties of the laser light with the temporal resolution granted by a pulsed radiation has proven to be a very powerful tool to be applied to the study of matter. Laser oscillators can, in mode-locking regime, be able to produce laser pulses pushing their duration until tens of femtoseconds. Further spectral broadening stages can be useful to reach a duration of a few femtoseconds. However, in order to get sub-femtosecond pulses, the broadening of the spectrum given by these stages is not enough. Actually, the lowest possible duration of an electromagnetic pulse is ultimately given by its wavelength:

$$c = \lambda\nu = \frac{\lambda}{T} \tag{1.1}$$

so

$$T = \frac{\lambda}{c} \tag{1.2}$$

where c is the speed of light. Then, in order for a pulse to be as long as ≈ 100 as, the wavelength has to be around 30 nm. This means that the spectrum

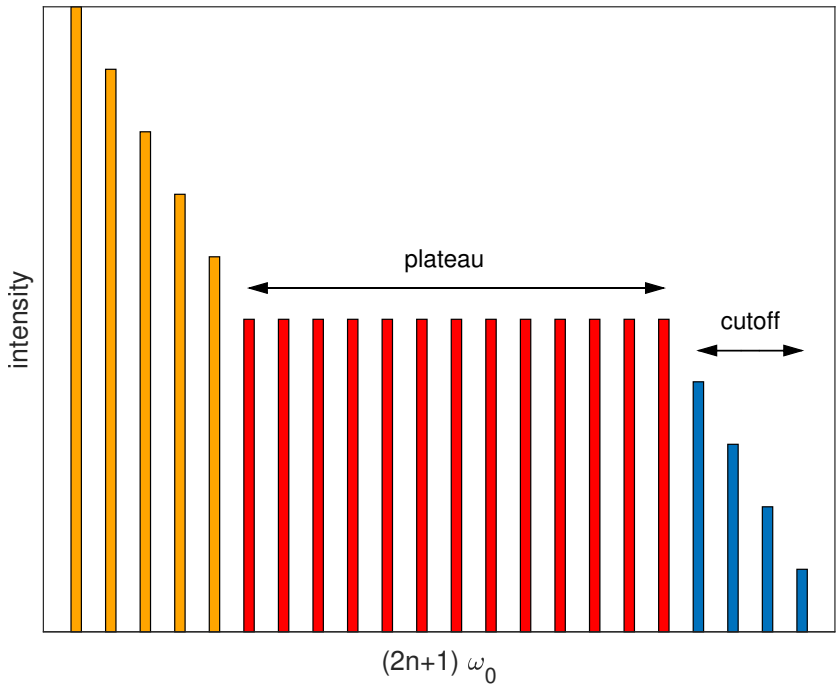

Figure 1.1: Shape of a typical spectrum generated by HHG

has to be broadened until it covers the XUV wavelengths. This is the purpose of the process called High-order Harmonic Generation.

1.1.2 Three Step Model

The High-order Harmonics Generation (HHG) is a highly non-linear phenomenon occurring when a short laser pulse with high energy (in a range around 10^{13} - 10^{15} W/cm^2) is focused into a gas medium. It allows to generate pulses in the XUV (eXtreme Ultra Violet) region of the spectrum starting from a strong IR (InfraRed) pulse. Usually, noble gases are involved in this process. Moreover, since it is a non-linear process, the non-linear polarization plays the main role. Then, noble gases being centrosymmetric, only the odd terms in the expansion of the polarization survive:

$$P = \epsilon_0(\chi^{(1)}E + \chi^{(2)}E^2 + \chi^{(3)}E^3 + ...) \tag{1.3}$$

where

$$\chi^{(2n)} = 0, \qquad n = 1, 2, 3... \tag{1.4}$$

Then, only odd harmonics of the fundamental frequency are generated. A typical spectrum produced by such a process is shown in Figure 1.1. At longer

wavelengths there's a region where the intensity of the harmonics decreases, followed by a *plateau* region, where the intensity is more or less constant, until it starts to decrease again, in a region called *cutoff*.
A simple model that can describe HHG is a semiclassical one called Three Step Model [21]. It allows to split the process into three parts:

1. Tunneling of the electron (ionization)
2. Motion of this electron in the continuum
3. Recollision

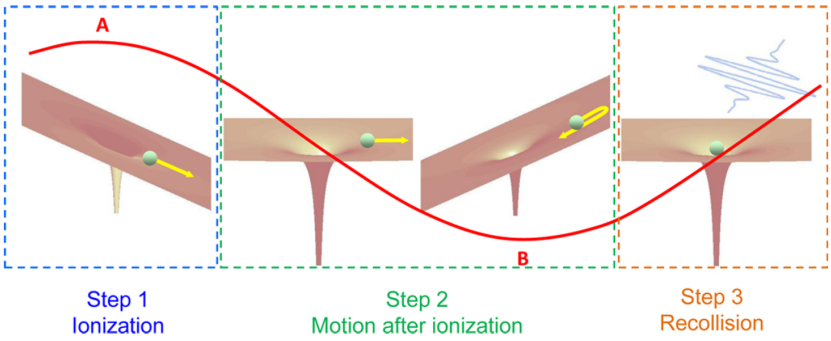

Figure 1.2: Graphical representation of the Three Step Model: the electron is treated as a wave when dealing with tunnel ionization, and as a particle when obeying Newton's 2^{nd} law during its motion. Image adapted from [21].

The first step is described by quantum tunneling of the electron, which sees a Coulomb potential that is strongly modified by the presence of an intense electric field, and then has a certain probability of overcoming the potential barrier and going into the continuum. It is a purely quantum effect since, classically, an infrared pulse could not ionize a noble gas, whose ionization energy is about one order of magnitude higher than the energy of the photon. Once free, the electron obeys Newton's 2^{nd} law, being accelerated away from the *parent ion*. After a quarter of optical cycle, the sign of the field changes and the electron is accelerated back to the original atom, where it can collide back recombining with its ion. The excess of energy, which counts as the ionization energy I_p plus the kinetic energy acquired during the free motion E_k can be emitted as a photon whose energy is associated to wavelengths in the XUV region of the spectrum. It is important to notice that this process happens only around the peaks of the IR electric field; this means that the generation occurs every half the optical cycle, producing a train of pulses.

The motion of the electron in the continuum can be modelled with Newton's law, assuming that the incoming field is monochromatic and linearly polarized in the x-direction:

$$\mathbf{E} = E_0 \cos(\omega_0 t)\mathbf{u}_x \tag{1.5}$$

where E_0 is the amplitude and ω_0 is the angular frequency of the field.
The electron obeys the equation:

$$\frac{d\mathbf{v}(t)}{dt} = -\frac{e\mathbf{E}(t)}{m} \tag{1.6}$$

Defining as t_i the instant of time when ionization occurs, we can set simple boundary conditions such as

$$\begin{cases} x(t_i) = 0 \\ \mathbf{v}(t_i) = 0 \end{cases} \tag{1.7}$$

that allow to solve the equation of motion, obtaining both the position and the velocity of the electron as a function of time:

$$\mathbf{v}(t) = -\frac{eE_0}{m\omega_0}[\sin(\omega_0 t) - \sin(\omega_0(t_i)]\mathbf{u}_x \tag{1.8}$$

$$x(t) = \frac{eE_0}{m\omega_0^2}[\cos(\omega_0 t) - \cos(\omega_0 t_i) + \omega_0(t - t_i)\sin(\omega_0 t_i)] \tag{1.9}$$

Then, defining as t_r the recombination instant of time, the equation

$$x(t_r) = 0 \tag{1.10}$$

defines the value of t_r, which will depend on t_i, as it is clear from Eq. 1.9. This equation has not an analytical solution, but it can be numerically solved, finding the relation between ionization and recombination times, as shown in Figure 1.3. It can be shown that the recombination is possible only for $0 \leq \omega_0 t_i \leq 80°$ (that is $0 \leq t_i/T_0 < 0.22$) and for $180° \leq \omega_0 t_i \leq 260°$ (that is $0.5 \leq t_i/T_0 < 0.72$). Notice that, in the interval of t_i/T_0 shown in Figure 1.3, the earlier the ionization occurs, the longer is the recombination time. Moreover, the recombination time is uniquely determined by the ionization time.
Knowing the velocity as a function of time allows to know the kinetic energy of the electron when it recombines:

$$E_k = \frac{1}{2}mv^2(t_r) = \frac{1}{2}m\frac{e^2E_0^2}{m\omega_0^2}[\sin(\omega_0 t_r) - \sin(\omega_0 t_i)]^2 \tag{1.11}$$

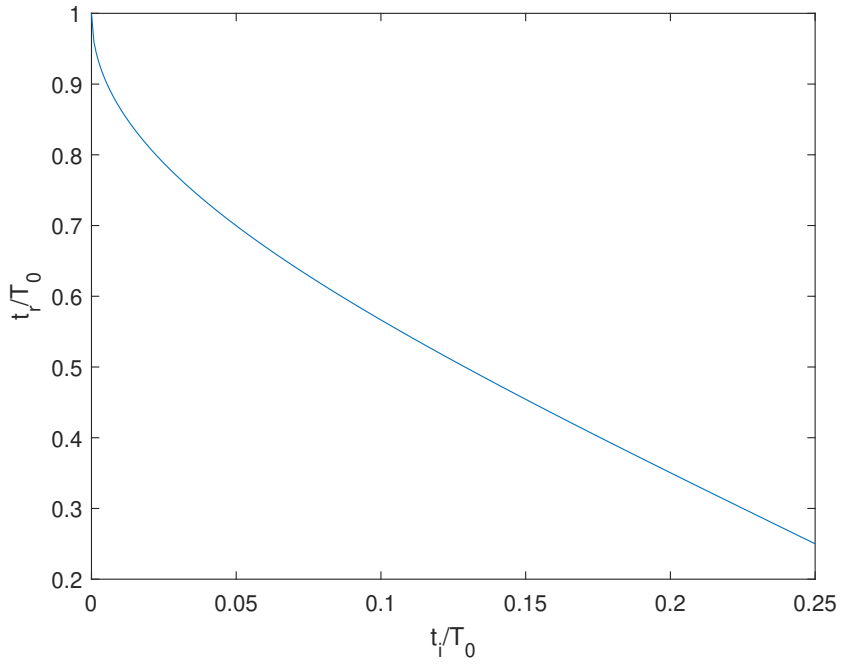

Figure 1.3: Relationship between ionization time instant and recombination time instant. Both axis are normalized with respect to the optical cycle T_0.

Then, by defining the *ponderomotive energy* as $U_p = \frac{1}{4}\frac{e^2 E_0^2}{m\omega_0^2}$, we can write the kinetic energy as

$$E_k = 2U_p[\sin(\omega_0 t_r - \sin(\omega_0 t_i)]^2 \tag{1.12}$$

Its behaviour is shown in Figure 1.4. The maximum of the kinetic energy is obtained in a point where $E_k \simeq 3.17U_p$, meaning that the cutoff photon energy (and thus photon frequency) is at

$$\hbar\omega_{cutoff} \simeq I_p + 3.17U_p \tag{1.13}$$

Since $U_p \propto I_0\lambda_0^2$, it is possible to move the cutoff further in energy by acting on the intensity or on the wavelength. From the graph it is also possible to see that the electron can follow, depending on the ionization time, a *long* path or a *short* path. The long paths correspond to $0 \leq t_i/T_0 < 0.05$ since the maximum of the kinetic energy is at $t_i/T_0 \simeq 0.05$.
Finally, it is important to notice that different wavelengths are emitted at different times: the emitted harmonics have then an intrinsic chirp, called *attosecond chirp*:

$$C = \frac{d\omega}{dt} \tag{1.14}$$

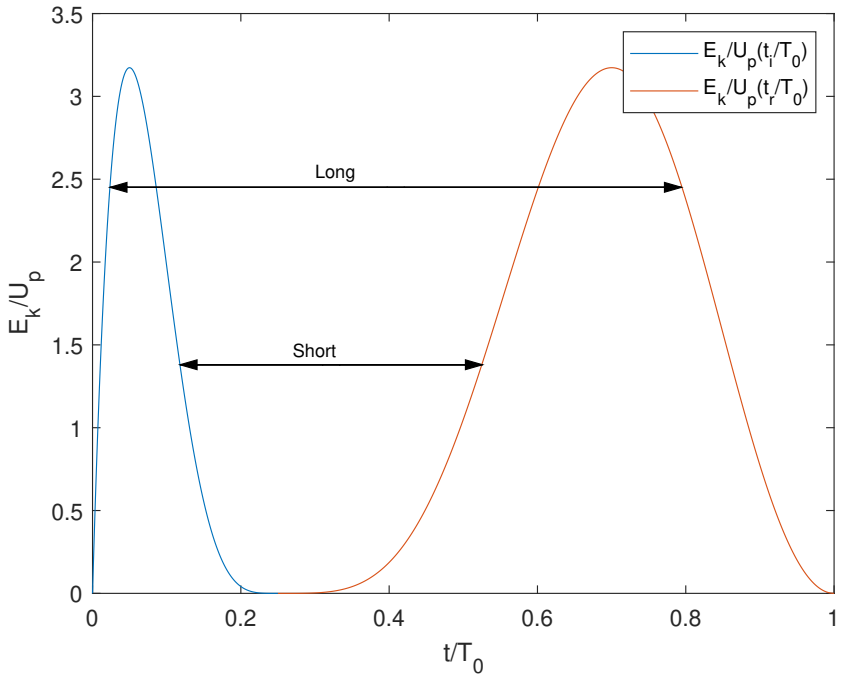

Figure 1.4: Kinetic energy of the recolliding electron normalized to the ponderomotive energy, as a function of both ionization and recombination time.

1.2 Charge Migration

The setup described in Chapters 2 and 4 aims at producing light pulses short enough to suddenly ionize and observe with a very short time resolution the response of atoms or molecules. The experimental observation of the ultrafast dynamics of electrons can tremendously increase our knowledge of the various effects involved in the mechanisms which trigger, for example, chemical reactions. One of the most interesting ultrafast physical phenomena which can be investigated through attosecond spectroscopy is the purely electronic dynamics of the electron wave packet during the first few femtoseconds after ionization. This physical process is named *charge migration* [2] [11].
The purpose of this section is to present a theoretical description of this phenomenon, introducing the main approximations which will allow us to get a picture of the basic mechanisms which lead this dynamics.

1.2.1 Introduction

Chemical reactions represent processes in which bonds between atoms are formed and broken, or in which the molecule undergoes structural changes. Therefore, they involve both a motion of the nuclei and a reorganization of the

electronic cloud of a molecule. A quantum approach which fully described the dynamics of the whole molecule, including both the electrons and the nuclei is analytically impossible. In fact, a quantum mechanical description comes from solving the time-dependent Schrödinger equation:

$$i\hbar\frac{\partial\psi((r),t)}{\partial t} = \hat{\mathcal{H}}(\mathbf{r})\psi(\mathbf{r},t) \tag{1.15}$$

In order to solve it, a molecular hamiltonian needs to be built. This can be done by assuming electrons and nuclei to be point-like charged particles interacting via Coulomb electrostatic interaction. The hamiltonian which comes from this assumption, by the way, is not analitically solvable and some approximations need to be implemented. One of the oldest one is the so called Born-Oppenheimer approximation: since the electrons are much lighter than the nuclei, it is reasonable to assume that they can follow the nuclear motion adiabatically, that is by instantaneously adapting to the nuclear geometry. This assumption is very important since it allows to decouple the electronic and nuclear motion.
By solving the Schrödinger equation in this framework, the energy structure depicted in Figure 1.5 is obtained. A vibrational and rotational energy levels structure, corresponding to the motion of the nuclei, is there for each electronic level. The separation between the electronic levels is of some eV, while the inner vibrational levels are split by some meV. According to the time-energy uncertainty principle:

$$\Delta E\Delta t \geq \hbar/2 \tag{1.16}$$

the vibrational levels spacing corresponds to a dynamic in the range of ps-fs while for the electronic states it falls into the region of attoseconds. This justifies the need of an attosecond time resolution in the case of an investigation of the molecular electronic dynamics.
The description of a many-electrons system, however, can not be analitically addressed. A further approximation is needed, and one of the most known ones is the Hartree-Fock (HF). According to this approximation it is possible to assume each electron to move independently in the mean field of the remaining electrons. This way the hamiltonian becomes a sum of one-electron hamiltonians and the wave function a product of one-electron wave functions, called *orbitals* ($\varphi_i(\mathbf{r})$). It is important to notice that this approximation is made to remove the correlation between the electrons which introduced mixed terms into the hamiltonian making the time-independent Schrödinger equation impossible to be analytically solvable. Anyway, the fermionic nature of these particles leads to the a form of correlation. In fact, the many-electrons

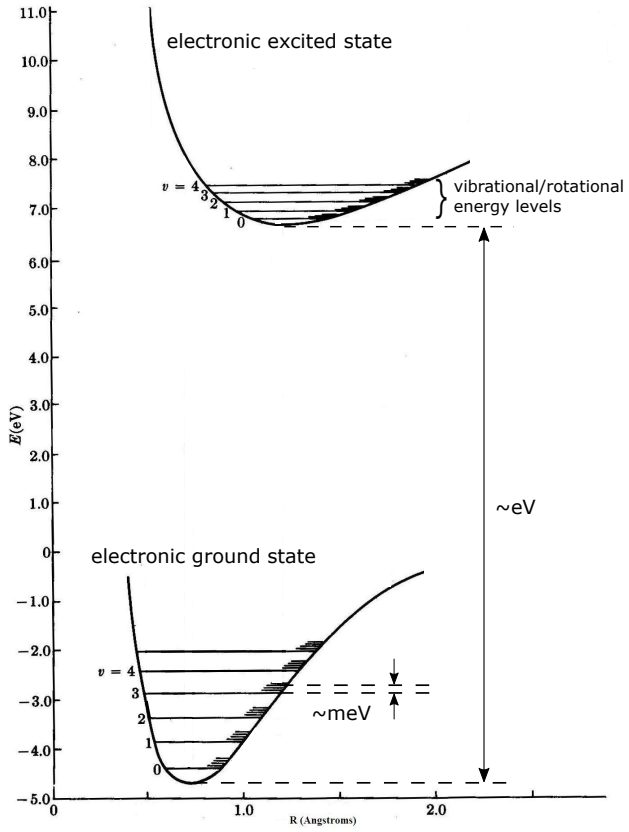

Figure 1.5: Sketch of the electronic levels, with the vibrational levels corresponding to the electronic ground state and excited state. The spacing between the electronic levels is of the order of the eV, while the distance between one vibrational level and another in in the meV scale.

wavefunction needs to be antisymmetrized, and this leads to a form of the electronic ground state of the molecule known as the Slater determinant:

$$|\phi_0\rangle = \frac{1}{\sqrt{N!}} \begin{vmatrix} \varphi_1(\mathbf{r_1}) & \dots & \varphi_N(\mathbf{r_1}) \\ \vdots & \ddots & \vdots \\ \varphi_1(\mathbf{r_N}) & \dots & \varphi_N(\mathbf{r_N}) \end{vmatrix} \tag{1.17}$$

This picture of electrons which can occupy orbitals is the common one used to describe a lot of physical and chemical phenomena.
Since, as discussed, it is possible to describe the motion of the electrons by assuming the nuclei fixed, it is interesting to study the case of a pure electronic dynamics initiated by a coherent population of electronic states triggered by ionization. The reason why it is interesting to theoretically describe this situation is that, being able to ionize and observe the behaviour of a molecule

within a short time (i.e. with an attosecond resolution) in laboratory, it will be possible to compare the theory with the experimental results.
As it will be discussed in the next section, the theory will rely on the so-called *sudden* approximation. We will assume that the ionized electron is removed from the system at a much shorter time scale with respect to that of the triggered electron dynamics. In other words, we neglect the interaction between the removed electron and the remaining ionic core. This approximation works well if the pulse is very short in time, within the attosecond time scale, and if its photon energy lies well above the ionization potential, such that the ionized electron possesses a high kinetic energy and can fastly leave the interaction volume.
Working in this framework it will be shown that, due to the correlation between electrons, the removal of one electron from a molecular orbit will lead to a coherent population of cationic states and this will launch ultrafast, pure electron dynamics. The hole left by the electron removed through ionization may then migrate through the system before the nuclear dynamics sets in, and this process is called *Charge Migration*, to distinguish it from the usual *Charge Transfer* driven by nonadiabatic coupling between the electron and nuclear motion.
In the next section a methodology which allows to describe the correlation-driven charge migration will be presented.

1.2.2 Theoretical Background

This analysis aims at following the electron dynamics after a sudden ionization. One possible way to trace this dynamics is by evaluating the density of the initially created hole, or the *hole density*, defined as:

$$\begin{aligned} Q(\mathbf{r},t) &= \langle\psi_0|\hat{\rho}(\mathbf{r},t)|\psi_0\rangle - \langle\phi_i|\hat{\rho}(\mathbf{r},t)|\phi_i\rangle = \\ &= \rho_0(\mathbf{r}) - \rho_i(\mathbf{r},t) \end{aligned} \tag{1.18}$$

where $\hat{\rho}$ is the local density operator, and

- $|\psi_0\rangle$ is the ground state of the neutral molecule, and so $\rho_0(\mathbf{r})$ is the time-independent ground state density of the neutral system
- $|\phi_i\rangle$ is the initially prepared cationic state, which is not an eigenstate of the cation, and so $\rho_i(\mathbf{r},t)$ is a time-dependent quantity.

Since $Q(\mathbf{r},t)$ describes the difference in densities of a system with n particles with respect to one having $n-1$ particles, the following normalization condition is valid:

$$\int Q(\mathbf{r},t)d\mathbf{r} = 1 \tag{1.19}$$

During the whole analysis atomic units will be used ($e = m_e = \hbar = 1$). By defining $\hat{\mathcal{H}}$ as the cationic hamiltonian, it is possible to rewrite $\rho_i(\mathbf{r}, t)$ in the Heisenberg picture as:

$$\rho_i(\mathbf{r}, t) = \langle \phi_i | e^{i\hat{\mathcal{H}}t} \hat{\rho}(\mathbf{r}) e^{-i\hat{\mathcal{H}}t} | \phi_i \rangle \tag{1.20}$$

As already discussed, the initially prepared cationic state $|\phi_i\rangle$ is not an eigenstate of the cationic hamiltonian. Anyway it is possible to define as $\{|I\rangle\}$ a complete set of cationic eigenstates, such that they are solution of the time-independent Schrödinger equation

$$\hat{\mathcal{H}} |I\rangle = \mathcal{E}_I |I\rangle \tag{1.21}$$

where the eigenvalues $\mathcal{E}_I$ are the ionization energies corresponding to the state $|I\rangle$. By inserting into Eq. 1.20 the identity operator, defined as $\sum_I |I\rangle \langle I|$, the time-dependent component of $Q(\mathbf{r}, t)$ becomes:

$$\begin{aligned} \rho_i(\mathbf{r}, t) &= \sum_{I,J} \langle \phi_i | I \rangle \langle I | e^{i\hat{\mathcal{H}}t} \hat{\rho}(\mathbf{r}) e^{-i\hat{\mathcal{H}}t} | J \rangle \langle J | \phi_i \rangle = \\ &= \sum_{I,J} \langle \phi_i | I \rangle \langle I | \hat{\rho}(\mathbf{r}) | J \rangle \langle J | \phi_i \rangle e^{i\mathcal{E}_I t} e^{-i\mathcal{E}_J t} = \\ &= \sum_{I,J} x_J^* \rho_{IJ}(\mathbf{r}) x_J e^{-i(\mathcal{E}_J - \mathcal{E}_I)t} \end{aligned} \tag{1.22}$$

where we have defined

- $x_I = \langle \phi_i | I \rangle$ as the transition amplitude with respect to the initial cationic state $|\phi_i\rangle$
- $\rho_{IJ}(\mathbf{r}) = \langle I | \hat{\rho}(\mathbf{r}, 0) | J \rangle$ as the charge density matrix between the states $|I\rangle$ and $|J\rangle$

One can assume, without loss of generality, that both x_I and ρ_{IJ} are real quantities, thus obtaining

$$\begin{aligned} \rho_i(\mathbf{r}, t) &= \sum_{I,J} x_I \rho_{IJ}(\mathbf{r}) x_J \cos((\mathcal{E}_J - \mathcal{E}_I)t) = \\ &= \underbrace{\langle \phi_i | \rho(\mathbf{r}, 0) | \phi_i \rangle}_{\rho_i(\mathbf{r}, 0)} - \underbrace{\sum_{I,J} x_I \rho_{IJ}(\mathbf{r}) x_J [1 - \cos((\mathcal{E}_J - \mathcal{E}_I)t)]}_{\Delta\rho(\mathbf{r}, t)} \end{aligned} \tag{1.23}$$

Then the hole density becomes

$$Q(\mathbf{r}, t) = \rho_0(\mathbf{r}, 0) - \rho_i(\mathbf{r}, 0) + \Delta\rho(\mathbf{r}, t) \tag{1.24}$$

where the first two terms, being time-independent, describe the density of the initially created hole while the third one describes the migration of the charge driven by the electron correlation.
In order to proceed, it is possible to exploit the second quantization representation of the density operator with a one-particle orbital basis of the molecule $\{\varphi_p\}$:

$$\hat{\rho}(\mathbf{r}) = \sum_{p,q} \varphi_p^*(\mathbf{r})\varphi_q(\mathbf{r})\hat{a}_p^\dagger \hat{a}_q \tag{1.25}$$

where $\hat{a}_p^\dagger$ and $\hat{a}_p$ are the creation and annihilation operators, respectively. The creation operator $a_p^\dagger$ creates an electron in the orbital φ_p while the annihilation operator removes an electron from the same orbital.
Within this representation the three terms contributing to the hole density as in Eq. 1.24 become:

$$\rho_0(\mathbf{r}, 0) = \sum_p |\varphi_p|^2 n_p \tag{1.26}$$

$$\rho_i(\mathbf{r}, 0) = \sum_{p,q} \varphi_p^* \varphi_q \, \langle \phi_i | \hat{a}_p^\dagger \hat{a}_q | \phi_i \rangle \tag{1.27}$$

$$\Delta\rho(\mathbf{r}, t) = \sum_{p,q} \varphi_p^* \varphi_q \sum_{I,J} x_I \, \langle I | \hat{a}_p^\dagger \hat{a}_q | J \rangle \, x_J [1 - \cos((\mathcal{E}_I - \mathcal{E}_J)t)] \tag{1.28}$$

Substituting these terms into the hole density expression, it takes the form of

$$Q(\mathbf{r}, t) = \sum_{p,q} \varphi_p^*(\mathbf{r})\varphi_q(\mathbf{r}) N_{pq}(t) \tag{1.29}$$

where $N_{pq}(t)$ are the matrix elements of $\mathbf{N}(t)$, which we will call the *hole density matrix* and n_p is the occupation number of orbital φ_p in the ground state. The hole density matrix elements are defined as:

$$\begin{aligned} N_{pq} = &\langle \psi_0 | \hat{a}_p^\dagger \hat{a}_q | \psi_0 \rangle - \langle \phi_i | \hat{a}_p^\dagger \hat{a}_q | \phi_i \rangle + \\ &+ \sum_{I,J} x_I \, \langle I | \hat{a}_p^\dagger \hat{a}_q | J \rangle \, x_J [1 - \cos((\mathcal{E}_I - \mathcal{E}_J)t)] \end{aligned} \tag{1.30}$$

The migrating hole charge is then described in time by the time-dependent matrix $\mathbf{N}(t)$ in the time-independent natural orbital basis $\{\varphi_p\}$. The diagonalization of this matrix leads to

$$Q(\mathbf{r}, t) = \sum_p |\tilde{\varphi}_p(\mathbf{r}, t)|^2 \tilde{n}_p(t) \tag{1.31}$$

where both the resulting eigenvalues $\{\tilde{n}_p(t)\}$ and the eigenfunctions $\{\tilde{\varphi}_p(\mathbf{r}, t)\}$ depend on time, and it comes from the time-dependence of $\mathbf{N}(t)$. The eigenfunctions $\{\tilde{\varphi}_p(\mathbf{r}, t)\}$ are called *natural charge orbitals* and the corresponding

eigenvalues $\{\tilde{n}_p(t)\}$ are their *hole occupation number*. Because of the normalization condition in Eq. 1.19, the hole occupation number satisfies the condition:

$$\sum_p \tilde{n}_p(t) = 1 \tag{1.32}$$

Unlike the previously defined $\{n_p\}$, the occupation numbers for the ground state, the hole occupation number $\tilde{n_p}(t)$ is a time dependent quantity, describing at each time t which part of the charge of the created hole is in the natural charge orbital $\tilde{\varphi}_p$.
If the ionization of the neutral system is described by the removal of one electron from one specific molecular orbital φ_i, at time $t = 0$ the density of the created hole is rather simple, having $\tilde{n}_i(t = 0) = 1$ and $\tilde{n}_{p\neq i}(t = 0) = 0$, so that the hole density matrix is diagonal having only one nonvanishing element $N_{ii}(t = 0) = 1$ and

$$Q(\mathbf{r}, 0) = |\tilde{\varphi}_i(\mathbf{r})|^2 \tag{1.33}$$

In the description depicted above, it is implicit that the process of ionization and rearrangement of the electronic cloud is neglected. This is the heart of the already described *sudden* approximation and it is valid in the limits cited above.
In order to simplify the expression in Eq. 1.30 it is useful to make some further assumptions. In the HF framework, if we assume also the ground state $|\psi_0\rangle$ to be weakly correlated, i.e. $|\psi_0\rangle \approx |\phi_0\rangle$, the first term of the N_{pq} expression becomes:

$$\langle\phi_0|\hat{a}_p^\dagger \hat{a}_q|\phi_0\rangle = n_p\delta_{pq} \tag{1.34}$$

As far as the second term of the equation is regarded, an assumption regarding the initial state is needed. The easiest and more natural assumption can be an initial cationic state created via the removal of an electron from a single orbital, such that

$$|\phi_i\rangle = \hat{a}_i\,|\phi_0\rangle \tag{1.35}$$

The initial state could also be constructed by a removal of an electron from a linear combination of Hartree-Fock states, anyway the choice we have made will be useful to unambiguously identify the basic mechanisms leading to charge migration which, due to the linearity of the time-dependent Schrödinger equation, will keep working also in the case of other choices. Within this assumption, the second term of the equation can be written as

$$\langle\phi_0|\hat{a}_i^\dagger \hat{a}p^\dagger \hat{a}_q\hat{a}_i|\phi_0\rangle = n_p\delta_{pq} - \delta_{pi}\delta_{qi} \tag{1.36}$$

and then the expression for N_{pq} becomes

$$N_{pq}(t) = \delta_{pi}\delta_{qi} + \sum_{I,J} x_I \langle I|\hat{a}_p^\dagger \hat{a}_q|J\rangle x_J[1 - \cos((\mathcal{E}_I - \mathcal{E}_J)t)] \tag{1.37}$$

The last opened question has to do with the cationic eigenstates $|I\rangle$. Also here, the exact cationic eigenstates and eigenvalues are not known and some approximations have to be done.
The simplest approximation we can use is to assume, as before, the HF ground state $|\phi_0\rangle$. Moreover, we can use as a cationic state the $1h$ configuration, which means

$$|I\rangle = \hat{a}_k |\phi_0\rangle \tag{1.38}$$

With regard to the cationic eigenvalues, the ionization energies can be taken as just the energies ε_k of the HF orbitals, according to Koopmans' theorem. The hole density matrix will therefore become

$$N_{pq} = \delta_{pi}\delta_{qi} + x_p x_q n_p n_q[1 - \cos((\varepsilon_p - \varepsilon_q)t)] \tag{1.39}$$

where it is possible to see that the time-dependent component survives only if both the involved orbitals are occupied ($n_p, n_q \neq 0$) Anyway, within this approximation the transition amplitude reduce to a Kronecker delta, since

$$x_p = \langle \phi_i|I\rangle = \langle \phi_0|\hat{a}_i^\dagger \hat{a}_p|\phi_0\rangle = \delta_{ip} \tag{1.40}$$

Then also $x_q = \delta_{iq}$ and so the time-dependent component of the hole density matrix vanishes:

$$N_{pq} = \delta_{pi}\delta_{qi} \tag{1.41}$$

This is the result of the Hartree-Fock and Koopmans' approximations, which correspond to a situation where electronic correlation effects are completely neglected, being in an independent-particles framework. This allows us to draw the first result of this theoretical discussion: in absence of electron correlation and relaxation the hole charge will not move from the orbital in which it has been originally created. In other words, no charge migration will take place. This is the reason why charge migration is addressed as a process solely driven by electron correlation.
Since many effects can contribute to the electron dynamics driven by electron correlation, it is useful to examinate cases in which the dynamics is governed by a single mechanism. In order to understand those simple mechanisms it is useful to consider a typical ionization spectrum of a molecule, since it has been shown that there is an intimate relationship between this spectrum and the dynamics triggered by the removal of one electron from a particular

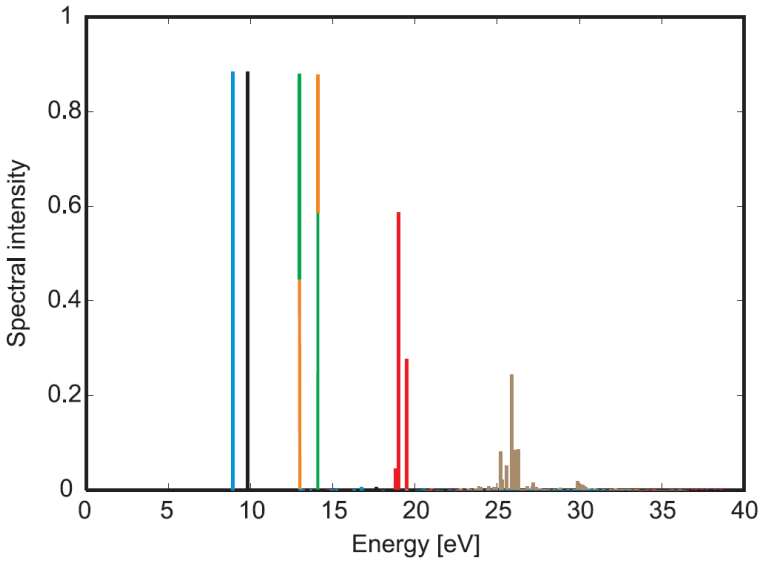

Figure 1.6: A typical ionization spectrum. The left, highest lines correspond to the *main* lines. The lines in red are the so-called *satellite* lines, while the weakest lines to the right are the lines corresponding to the inner valence shell. Adapted from [13].

orbital. It is made of lines, each corresponding to a cationic eigenstate $|I\rangle$, positioned at the corresponding ionization energies $\mathcal{E}_I$ and whose amplitude is given by the modulus squared of the transition amplitude $x_I = \langle I|\hat{a}_i|\psi_0\rangle$. Computing ionization spectra at fixed nuclear geometry with computational quantum chemistry tools, it is possible to observe that:

- in case of absence of correlation (independent particle model) a finite series of lines appears, each with amplitude one, and one for every orbital occupied in the ground state ϕ_i. Their position corresponds to the orbital energies ε_i, according to Koopmans' theorem.

- if correlation effects are weak, as it usually is for the outer valence shells' orbitals, the spectrum is made of *main lines* which have a large overlap with the $1h$ configuration. In this case the molecular orbital picture is still valid. In Figure 1.6, they correspond to the lines on the left.

- if correlation effects get stronger, *satellite lines* appear, representing excitations on top of ionization. Their amplitude will be of course lower since $2h1p$ configurations are not so well overlapped with the $1h$ configuration. They are the red lines in Figure 1.6. In this case it is important to distinguish between two type of satellite lines: if both holes

differ from the $1h$ orbital of the main line, the satellites are addressed as *correlation satellites*. Otherwise, they are called *relaxation satellites*

- if the correlation effects are very strong, like in the inner valence, this distinction between main and satellite lines does not exist anymore and the spectrum is composed by a quasi-continuum of relatively small amplitude lines.

In the following section three basic charge migration mechanisms which has been identified will be presented.

1.2.3 Basic Charge Migration Mechanisms

We will discuss three basic mechanisms, depending on the structure of the ionic states.

(i) **Hole-mixing**
In this case we consider two lines in the spectrum corresponding to ionic states which are linear combinations of two $1h$ configurations. More specifically,

$$|I\rangle = \alpha \hat{a}_i |\phi_0\rangle + \beta \hat{a}_j |\phi_0\rangle \tag{1.42}$$

$$|J\rangle = \beta \hat{a}_i |\phi_0\rangle - \alpha \hat{a}_j |\phi_0\rangle \tag{1.43}$$

where, due to orthonormality of the states, $\alpha^2 + \beta^2 = 1$.
In this case the hole density matrix takes the form of

$$\mathbf{N}(t) = \begin{bmatrix} 1 - 2(\alpha\beta)^2[1 - \cos(\omega t)] & (\alpha^2 - \beta^2)\alpha\beta[1 - \cos(\omega t)] \\ (\alpha^2 - \beta^2)\alpha\beta[1 - \cos(\omega t)] & 2(\alpha\beta)^2[1 - \cos(\omega t)] \end{bmatrix} \tag{1.44}$$

The diagonalization of this matrix leads to the hole occupation number

$$\tilde{n}_{i/j}(t) = \frac{1}{2} \pm \frac{1}{2}\sqrt{1 - 4(\alpha\beta)^2 \sin^2(\omega t)} \tag{1.45}$$

which represents the occupation of the natural charge orbitals $\tilde{\varphi}_i$ and $\tilde{\varphi}_j$ during time. It is important to remember that the natural charge orbitals are, at every time instant t, a different linear combination of the HF orbitals φ_i and φ_j. Then the effect of a two hole-mixing leads to an oscillation between the two natural charge orbitals occurring with an angular frequency $\omega = \mathcal{E}_I - \mathcal{E}_J$.

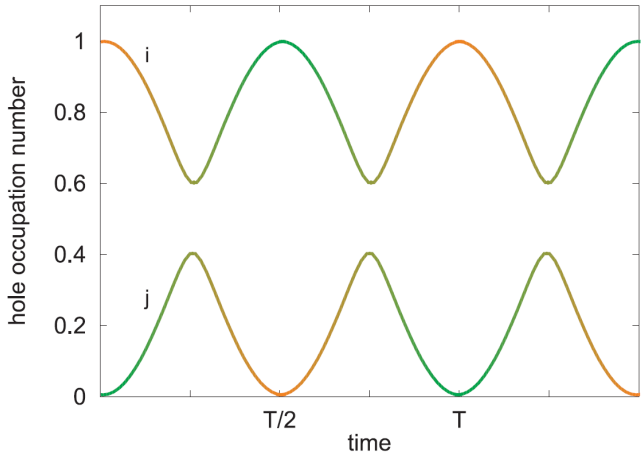

Figure 1.7: The orange colour represents a greater component of the initially ionized orbital φ_i into the natural charge orbital, while the green one represents a bigger weight for φ_j. It is possible to see that every half of a period the character of both natural charge orbitals swaps. Adapted from [11].

The result is shown in Figure 1.7, where the colors represent the weight of the two HF orbitals to the natural charge orbital. It is possible to see that the character of the i and j natural charge orbitals change every half of a period. More specifically, we can see that the initially ionized orbital φ_i loses its charge within the first half of the period, transferring it to the other orbital involved in the hole mixing. This process goes on periodically, and if the orbitals φi and φi are spatially located in different regions of the molecule, this oscillation will reflect on an oscillation of the electronic cloud through the molecule.

(ii) **Dominant-satellite**

Let us now consider the case in which two ionic states corresponding to a main state and a satellite have overlap with the original $1h$ configuration. Since the satellite line corresponds to an excitation on top of ionization, the two states will now have the following expression:

$$|I_m\rangle = \alpha \hat{a}_i |\phi_0\rangle + \beta \hat{a}_a^\dagger \hat{a}_k \hat{a}_l |\phi_0\rangle \tag{1.46}$$

$$|I_s\rangle = \beta \hat{a}_i |\phi_0\rangle - \alpha \hat{a}_a^\dagger \hat{a}_k \hat{a}_l |\phi_0\rangle \tag{1.47}$$

where the $i, j, \ldots$ indices refer to occupied orbitals (or holes) while the $a, b, \ldots$ indices refer to the unoccupied virtual orbitals. Here, the terms $\alpha \hat{a}_i |\phi_0\rangle$ correspond to the $1h$ configuration, while the terms $\alpha \hat{a}_a^\dagger \hat{a}_k \hat{a}_l |\phi_0\rangle$ refer to the two-hole-one-particle ($2h1p$) configuration which indicate that after the removal of one electron another one is excited to a virtual orbital. Also here $\alpha^2 + \beta^2 = 1$.

In this case we need to split the discussion into the correlation satellite case and relaxation satellite case.
If $\varphi_i \neq \varphi_k \neq \varphi_l$, i.e. we are into the correlation satellite case, the hole occupation number for the natural charge orbitals become:

$$\tilde{n}_i(t) = 1 - 2(\alpha\beta)^2[1 - \cos(\omega t)] \tag{1.48}$$

$$\tilde{n}_k(t) = \tilde{n}_k(t) = -\tilde{n}_a(t) = 2(\alpha\beta)^2[1 - \cos(\omega t)] \tag{1.49}$$

where $\omega = \mathcal{E}_{I_m} - \mathcal{E}_{I_s}$ and, as before, φ_i is the orbital where the first ionization takes place. This result is shown in Figure 1.8, where it is possible to observe a periodic behaviour with a period determined by the energy difference between the states $\mathcal{E}_{I_m}$ and $\mathcal{E}_{I_s}$. The hole is initially created in the orbital φ_i, then a further excitation from the orbital φ_l (or φ_k) will accompany the migration of the hole to the orbital φ_k (or φ_l). Also here, depending on the spatial properties of the orbitals involved, the hole can migrate through the molecule.

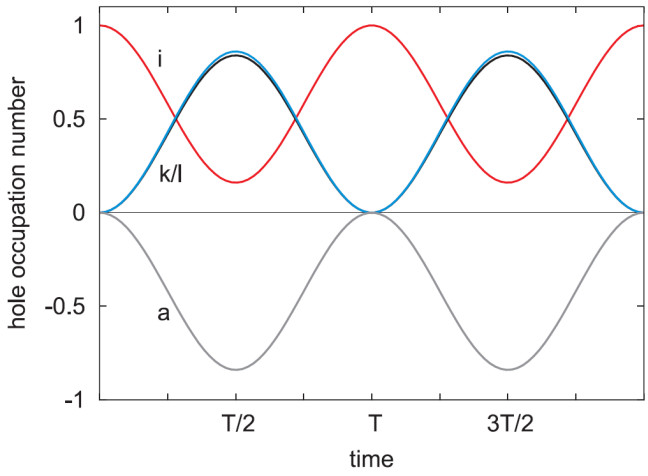

Figure 1.8: Correlation satellite case. The oscillation of the occupation number corresponding to the orbital φ_i is accompanied by the oscillating excitation from one of the two φ_k and φ_l orbitals to the orbital φ_a. Adapted from [11].

Otherwise, if either $k = i$ or $l = i$, meaning that we are in the relaxation satellite case, the situation is different. Assuming for example to be in the situation where $l = i$, the hole occupation numbers will be:

$$\tilde{n}_i(t) = 1 \tag{1.50}$$

$$\tilde{n}_k(t) = -\tilde{n}_a(t) = 2\alpha\beta \sin^2(\omega t/2) \tag{1.51}$$

In this case the hole remains localized in the orbital φ_i where it was originally created, while an oscillating excitation and deexcitation takes place between the orbitals φ_k and φ_a, as depicted in Figure 1.9.

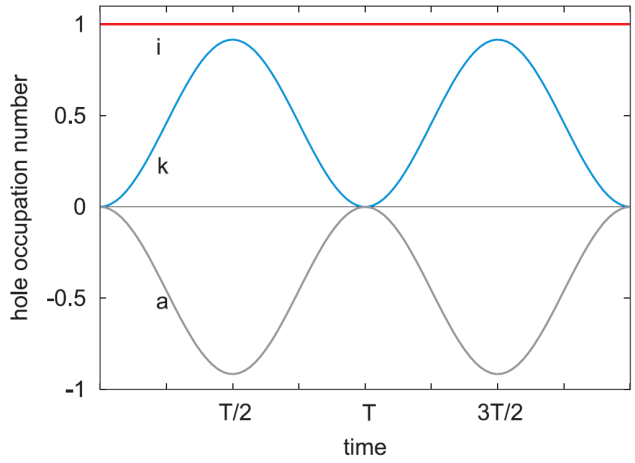

Figure 1.9: Relaxation satellite case. The hole remains localized in the orbital where it was initially created, but an oscillating behaviour is observed between the orbitals φ_k and φ_a. Adapted from [11].

(iii) **Breakdown of the molecular orbital picture case**
Considering the case in which the electron correlation effects are quite strong and the molecular orbital picture is not a feasible model anymore, which is the case of the inner-valence region of the spectrum, the situation is completely different. Supposing that the quasi-continuum of states which is there in this region of the spectrum has a Lorentzian shape, the initially created hole will decay exponentially. The process through which this charge is lost depends on whether the states are below or above the double ionization threshold. If they lay above the double ionization threshold, in fact, there is the possibility for an electron coming from a higher orbital to fill the hole while a secondary electron is ejected from another orbital to the continuum, in an Auger-like mechanism. Otherwise, this possibility is not there, so the charge will be spread among many orbitals being spread uniformely over the whole cation.

These are the basic mechanism through which it is possible to simulate the dynamics of the electronic cloud of an ionized molecule in time. It is important to notice that the charge migration mechanisms, implying a dynamic of the electrons, change the effective potential seen by the nuclei and then can trigger nuclear motion, which, in turn, is responsible for the charge transfer mechanisms. So, by the comparison of the theoretical results with the ultrafast pump-probe experiments the hope is to get an increasingly detailed knowledge of the charge migration dynamics which could, possibly, allow to also manage the charge transfer.

1.3 Pump-Probe Ultrafast Spectroscopy of Bio-Relevant Molecules

In pump-probe experiments driven by ultrafast pulses, a system is prepared by creating a coherent superposition on intermediate states (pump pulse) and then, controlling the delay of the probe pulse, to look at a signal in time which corresponds to the interference between the different pathways leading to the final states. However, scientists faced, since the beginning, several theoretical aspects and experimental issues which needed (and still do need) time and efforts to be solved [15].
The first experiment showing an effect which was probably attributable to charge migration was performed on polypeptide molecules. By using UV nanosecond pulses Weinkauf et al. [32] were able to show that local ionization by excitation of a cromophor at the C-end of the molecule leads also to fragment ions originating from the N-end of the polypeptide. Since the observation did not depend on the actual length of the polypeptide, it was concluded that the underlying mechanism must be of pure electronic nature happening on an ultrafast timescale, in which nuclear motion does not play a role. This result was achieved with steady-state ion spectra and nanosecond laser pulses. The dynamics of the observed process were hence not investigated in this study. Because of the apparent success of this experiment, however, advances in the ultrafast optics field and, most of all, in the attosecond science field, since pure electronic phenomena occur on that time scale, pushed towards the study of this charge propagation in time.
As described in Section 1.2, charge migration relies on the sudden creation of a coherent superposition of hole states. Moreover, when electron correlation plays a role, this superposition of states is not an eigenstate of the cation. The result is a non-stationary state, leading to dynamical effects. However, the role of the nuclear dynamics remains important since it can govern the final trapping of the charge. This opens the possibility to control the site at which the charge finally localizes and then, potentially, the chemical reaction which may follow, such as a dissociation of the bond at which the positive charge is localized. This interpretation is supported by theoretical quantum chemical calculations which aimed at demonstrating the possibility of controlling the reactivity of a couple of peptides by the means of the hole non-stationary states [24]. It was discussed the possibility for these states to impede the usual vibrational energy redistribution in some peptides and the theoretical results were compared with the previously described experimental works.
Further theoretical hole migration investigations were performed on various molecules, which were usually organic molecules or molecules of biological

interest, since the possibility to control their reactivity teases, for obvious reasons, scientists' ideas. Predictions on N-methylacetamide showed a hole dynamics from one side to the other one of the molecule within a few femtoseconds [7] and the analysis of these process on DNA bases such as glycine showed dynamics corresponding to different times corresponding to different conformers [12].
On the experimental side, pump-probe spectroscopy has been used in a two-colour scheme where an XUV isolated attosecond pulse (IAP) or attosecond pulse train (APT) was used as the pump and a near-infrared (NIR) pulse as the probe. The reason why not too many attosecond pump-attosecond probe beamlines have been implemented is that the intensity of the attosecond pulses which can be generated up to now is still too low. Since the molecular sample is usually in gas-phase and some wavelengths can be non-resonant with the energetic levels, very high intensities are needed.
The XUV-NIR pump-probe approach has however some drawbacks. First of all, the ultrafast XUV pulses have intrinsically a large bandwidth, and this implies being resonant with usually a lot of different transition energies. Moreover the high intensity of the IR probe may drastically alter the molecular potential landscape, thus preventing the photo-physics of the bare molecule.
A first attosecond pump-probe experiment in molecules was performed using the simplest molecule in nature, that is the hydrogen molecule H_2. It was performed with co-polarized pump and probe pulses where the NIR few-cycle probe pulse perturbed the remaining electron in the H_2^+ ion. Depending on the XUV-NIR delay, the fragment moved preferentially upward/downward with respect to the polarization axis. This means that, depending on this delay, there was a preference for the bound electron to move towards one or the other hydrogen nucleus [25]. Here, two mechanisms have shown to be responsible for this effect: one related to the entaglement between the ejected electron and the molecular ion wavefunctions and the other one involving the coupling between the electronic and nuclear degrees of freedom. By further theoretical studies in Xe it has been shown that the coherence between hole states can be reduced by interchannel coupling, which, besides affecting the hole populations, also enhances the entanglement between the photoelectron and the remaining ion [22]. This further proved the need of a high energy ionizing pulse so that the kinetic energy of the emitted photoelectron is very high and the electron rapidly moves away from the molecule (as in the framework of the *sudden* approximation, see Section 1.2).
More recently, an experiment on a larger and more complex molecule, phenylalanine, has been performed in our laboratories at Politecnico di Milano [3]. Phenylalanine is an α-aminoacide with a benzyl group as a side chain (see

Figure 1.10).
The two-colours pump-probe experiment employed a sub-300 as pulse with photon energies between 15 and 35 eV as a pump and a 4 fs VIS/NIR pulse as a probe, with a photon energy around 1.77 eV. The mechanism employed to evaporate and carry the phenylalanine molecules to the interaction region was different with respect to the one which we implemented (see Section 3.2) and relied on the evaporation of the amino acid molecules from a thin metallic foil performed by a continuous wave laser. The attosecond pump pulse focused in the interaction region ionized and excited the phenylalanine molecules and, as expected, a rich fragmentation pattern was observed upon ionization with XUV pulses. When the femtosecond VIS/NIR pulse is added, a double-charged immonium ion ($^{++}NH_2$-CH-R) is produced also, since the absorption of several IR photons can surmount the double ionization threshold. Then, the experiment consisted of the measurement of this double-charged photofragment yield as a function of the XUV-NIR delay. The result was, on a long time scale, an exponential decay with a rising time of about 10 fs and a decay constant of about 25 fs. However, between 15 and 25 fs after the XUV ionization an oscillation superimposed on the exponential decay was clearly observable. These oscillations period was about 4.3 fs. Quantum chemical calculations on phenylalanine showed that the highest vibrational frequency correspond to the X-H stretching mode, and it implies oscillations with a period around 9 fs. This suggested that the observed oscillation come from a purely electronic dynamical effect.
The spectral properties of the XUV pulse were then modified by inserting an indium foil into the beampath, thus getting a spectrum centered at 15 eV and with a FWHM of 3 eV; the components at higher energies were then strongly weakened. In this case, almost no signal for the dication was found. This suggested that the dication formation comes from an IR few-photons process from a highly excited state of the cation to the lowest states of the dication, confirmed by the theoretical computation of the cation energy levels. A pulse with a spectrum centered at significantly lower energies, such as the one just described, was not able to excite the cation to high-enough energy states and thus the dication could only be generated through a much less probable IR multiphoton process.
The experimental result was then compared with the computed result by plotting the spectral components of the resulting signal as a function of the pump-probe delay. Simulations were performed by assuming a coherent superposition of the $1h$ cationic states neglecting the higher-order processes leading to correlation satellites (see Section 1.2.3). The comparison gave satisfactory results, especially for the spectral component with period 4.3 fs described before. This matching was even more impressive considering that

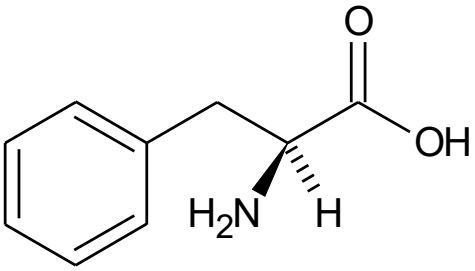

(a) Structural formula of phenylanine

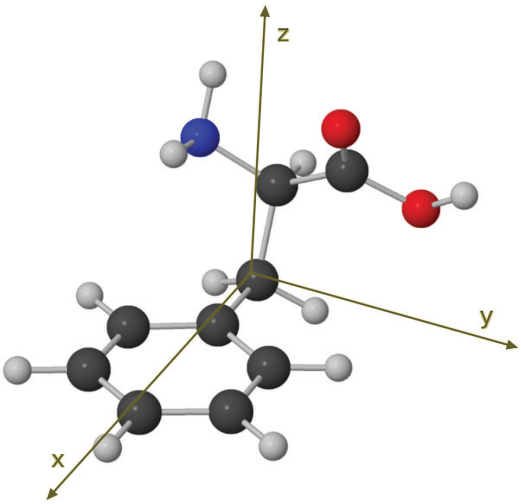

(b) 3D representation of phenylanaline. The grey dots represent H atoms, the black ones C atoms, the blue one N atom, the red one O atom. Adapted from [3]

Figure 1.10: Representations of phenylanaline. It is an α-aminoacid where a central α-carbon atom is connected to a carboxyl group (-COOH), an amine group (-NH_2), a hydrogen atom and to a side chain which is, in this case, a benzyl group. The conformer in (b) was the most abundant one at the temperature conditions of the experiment (around 430 K), as theoretical computations showed.

the simulations did not take into account the interaction with the NIR pulse. Oscillation with this period were observed, in simulations, around the amine group site. It was then possible to conclude that resulting periodic behaviour observed in the experiment originated from the absorption of the probe pulse by the amine group.

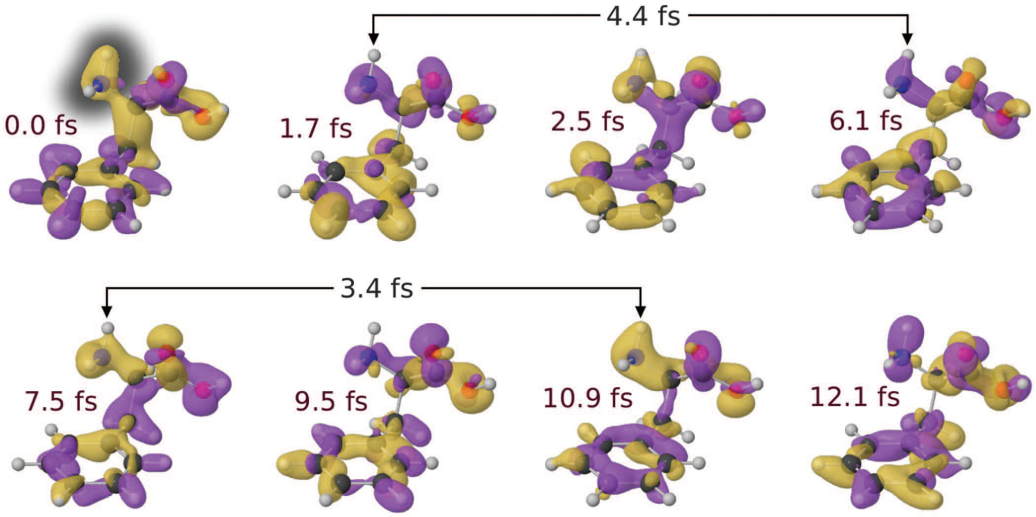

Figure 1.11: Computed charge redistribution along the phenylalanine molecule, at different times after the XUV ionization. The yellow clouds correspond to a relative eccess of positive charge, while the purple a lack of positive charge. Adapted from [3].

A different kind of experimental approach which proved to be useful to trace charge migration in molecules relies on the temporal resolution provided by the subcycle nature of the HHG process (see Section 1.1). Actually, by selecting only short trajectories, each emitted harmonics corresponds to a unique electron transit time in the continuum. Then, by analyzing the properties of these harmonics (their amplitude and phase) one can trace the hole density of a molecule in time: this technique is referred as HHS (high-harmonic spectroscopy). This is what has been done on iodoacetylene molecules by Kraus et al. [10]. By impulsively orienting this linear molecule, they were able to distinguish between quasi-field-free charge migration and laser-induced charge migration. In the first case, when the ionizing laser was perpendicular to the axis of the molecule, the strong-field-induced hole was found to be localized on the iodine site, moving toward the acetyle site in about 930 as. Since population transfer was absent by symmetry, this was regarded as a charge migration effect.
In the latter case, when the incoming laser came from a direction parallel to the alignment of the molecules, it was found on the acetylene site, and since iodine ionization is dominant in this case, the hole was created on a different

site with respect to the ionization site. This could seem counter intuitive, but it was coherent with the state at lowest energy for the cation, and suggests that the initial phase of the hole wavepacket depends on the orientation of the molecule with respect to the incoming laser field. Moreover, it was demonstrated for the charge migration process to be influenced by the laser field. This opens the possibility to localize the hole in a certain site of the molecule, especially by using laser pulses with subcycle-controlled waveform.

Chapter 2

Beamline

In this chapter an overview of the whole experimental setup used in the *Elyche* (ELectron-scale dYnamics in CHEmistry) laboratory is presented. The chapter is divided into six sections, each of them dealing with a different stage of the setup.
First, an overview of the whole setup is presented in the scheme of Figure 2.1.

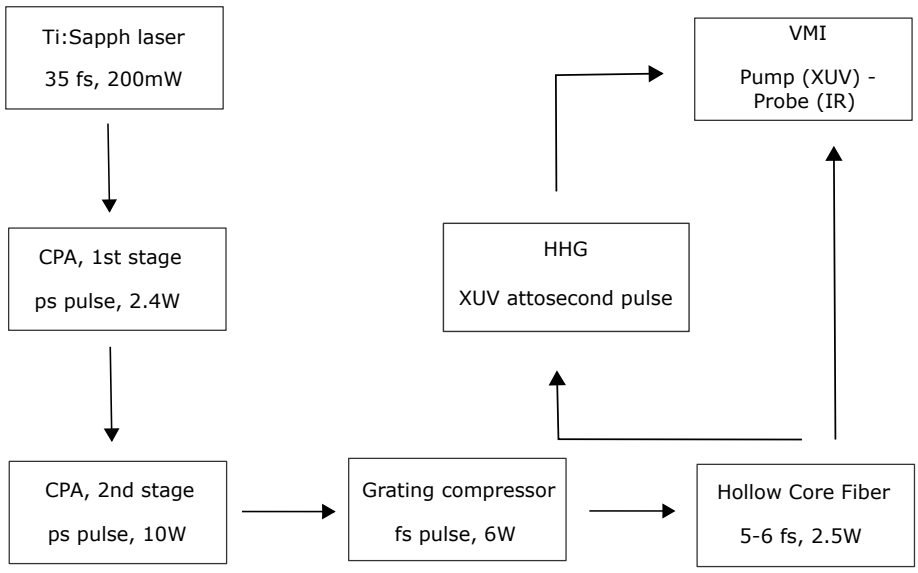

Figure 2.1: Block scheme of the whole setup.

A commercial Ti:Sapphire (Ti:Sa) laser emits, in mode-locking regime, pulses with a temporal duration of is around 35 fs and power around 200 mW,

horizontally-polarized. Through two amplification stages, based on the CPA (*Chirped Pulse Amplification*) scheme, a power of about 6 W is achieved. A further compression of the pulses up to 5-6 fs is possible thanks to a hollow core fiber and a set of chirped mirrors.
A fraction of the beam (70%) is sent to generate XUV radiation by the process of High-order Harmonic Generation. This provides attosecond pulses that will be used to excite the molecule (pump pulses). The rest of the beam (30%) is used as a probe. Both pump and probe are recombined in a phase-stabilized interferometer and directed into the target chamber.

2.1 Laser Source

2.1.1 Amplification Stage

In 1985 Gérard Mourou and Donna Strickland proposed a new technique whose aim was to get high energy, ultrashort pulses [27]. They were able to overcome a problem which could have limited the advances in ultrafast optics: the shorter the time duration of the pulse, the higher the peak intensity, leading to a damage of the active medium. This technique is called Chirped Pulse Amplification (CPA) and was awarded the 2018 Nobel Prize in Physics. The idea behind it is sketched in Figure 2.2. First, the pulse is sent

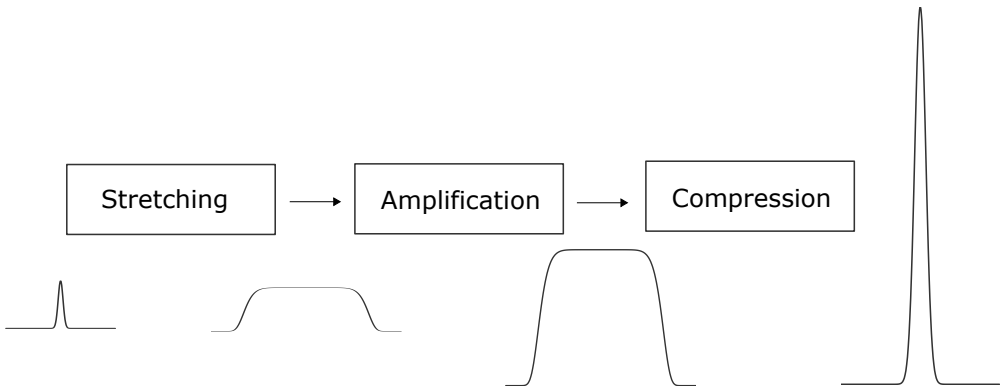

Figure 2.2: Block scheme of the Chirped Pulse Amplification (CPA) technique. An idea of the temporal behaviour of the pulse is sketched in each passage.

through a dispersive medium and thus it is stretched in time. This way, the spectrum of the pulse is not affected, but the peak power decreases. Then, amplification is performed on the stretched pulse avoiding damages of the

crystal. Finally, the pulse is compressed coming back to its original duration but with a higher energy.
The laser source used in the *Elyche* is a commercial system from *FemtoLasers Produktions GmbH* company, *FemtoPower Pro V CEP*. A Ti:Sa oscillator, *Femtosource Rainbow*, generates 25 fs, 200 mW pulses in mode-locking regime. Then, it goes into a 9-pass multipass amplifier (pre-amplifier), where a *Photonics Industries* frequency-doubled Nd:YLF Q-switched, 527 nm laser is used as a pump. The output power of this stage is about 2.4 W. In a second two-pass amplifier (booster) the power is increased up to 10 W. After the booster, a double grating compression stage is used to get a short, high energy pulse. In this stage, negative second order dispersion is achieved thanks to the spatial separation of different wavelengths given by the diffraction grating.

2.2 CEP Stabilization

In order to be able to generate single attosecond pulses, the laser needs to have the carrier-envelope phase stabilized [9]. This phase plays a role in HHG: for example, in the ionization gating technique it is essential that one peak of the electric field coincides with the maximum of the envelope, such that one single peak has enough intensity to generate an attosecond pulse.
In this laser system, Carrier-Envelope Phase (CEP) stabilization is performed by two stabilization stages. The first one consists of a f_0 - f interferometer, installed just outside the oscillator cavity and it's able to lock the offset frequency at 1/4 of the oscillator repetition frequency. The other one is a f - $2f$ interferometer installed at the end of the laser system which compensates for the slow CEP drifts.

2.3 Hollow Core Fiber

The amplified pulse is then focused into a Hollow Core Fiber to widen its spectrum, through the physical process called Self-Phase Modulation. After presenting the theoretical treatment, I will describe the experimental setup.

2.3.1 Self-Phase Modulation

The Hollow Core Fiber technique was proven to be suitable for compression of short pulses of high energy [20]. The physical principle behind it is the so called Self Phase Modulation. It is a third order non-linear effect, occurring when an electromagnetic field goes through a medium which has a $\chi^{(3)} \neq 0$. If

we assume that the field is oscillating at angular frequency ω, the non-linear polarization of the medium can be written as:

$$\begin{aligned} P &= P_{lin,\omega} + P_{nonlin,\omega} = \\ &= \epsilon_0 \chi_{lin} E_0 + \epsilon_0 \chi_{nonlin,\omega} |E_0|^2 E_0 = \\ &= \epsilon_0 E_0 [\chi_{lin} + \chi_{nonlin,\omega} |E_0|^2] = \epsilon_0 E_0 \chi_{tot} \end{aligned} \tag{2.1}$$

where we assume a linear polarization of the incoming field, with an amplitude of the incoming electric field equal to E_0 and χ_{nonlin} is a coefficient depending both on the pulsation ω and on the strength of the third order non-linearity.
Then the squared of the refractive index n^2, equal to the relative permittivity $\epsilon_r = 1 + \chi_{tot}$, can be written as

$$n^2 = 1 + \chi_{tot} = \underbrace{1 + \chi_{lin}}_{n_0^2} + \chi_{nonlin} |E_0^2| \tag{2.2}$$

and then, through a Taylor expansion of the squared root, we can get

$$n \simeq n_0 + n_2 I \tag{2.3}$$

because the intensity of the electric field I is proportional to $|E_0^2|$. The coefficient coming from the Taylor expansion n_2, is called *non-linear refractive index* as it quantifies the variation of the refractive index with the intensity of the pulse. Then, the wave vector can be defined as

$$k = \frac{\omega_0}{c} n \tag{2.4}$$

where ω_0 is the central frequency and c is the speed of light. If the pulse is propagating along z, the phase is defined as

$$\phi = \omega_0 t - kz = \omega_0 t - \frac{\omega_0}{c} nz \tag{2.5}$$

and then the instantaneous angular frequency becomes

$$\omega = \frac{d\phi}{dt} = \omega_0 - \frac{\omega_0}{c} z n_2 \frac{\partial I}{\partial t} \tag{2.6}$$

This means that the broadening of the spectrum with respect to ω_0 depends on the partial derivative with respect to time of the intensity of the pulse:

$$\Delta\omega \equiv -\frac{\omega_0}{c} z n_2 \frac{\partial I}{\partial t} \tag{2.7}$$

Its behaviour in the case of a pulse with a gaussian envelope is sketched in Figure 2.3, where it is also possible to see the up-chirp of the resulting pulse.

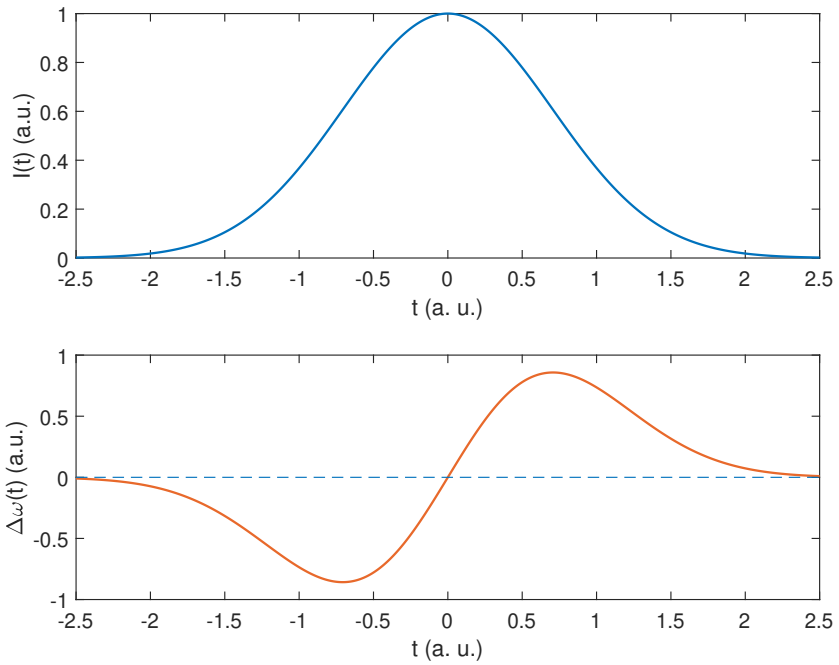

Figure 2.3: Self Phase Modulation on a pulse. The shape of intensity determines a range of new frequencies, up-chirped.

2.3.2 Experimental Setup

The Hollow Core Fiber used for this setup is a made of fused silica, with a length of 90 cm and an internal diameter of 320 μm. The spot size of the beam being coupled into the fiber is, in the focus, around 230 μm, which ensures the best coupling efficiency for the EH_{11} mode [19].
In order to get the correct spot size, a telescope reduces the beam diameter, then a converging mirror focuses it in the entrance of the fiber. Moreover, the fiber is mounted on two slits which allow to move the fiber on the orthogonal plane. This allows serves for the fine alignment and for the proper selection of the correct mode that is coupled into it.
The coupling of the beam into the fiber is kept stable during time by monitoring the beam alignment through a 4-quadrants photodetector placed as in Figure 2.4 and adjusting it accordingly. This photodetector receives, in the focal position, a small fraction of the beam which is reflected by a 95:5 beam splitter. A feedback stabilization system moves a piezo mirror placed before the converging mirror in order to keep the beam aligned. Otherwise, the fiber could be damaged or some power could be lost.
A drawback of the Hollow Core Fiber technique is the loss of power due to multiphoton ionization and optical filamentation, happening mainly at the

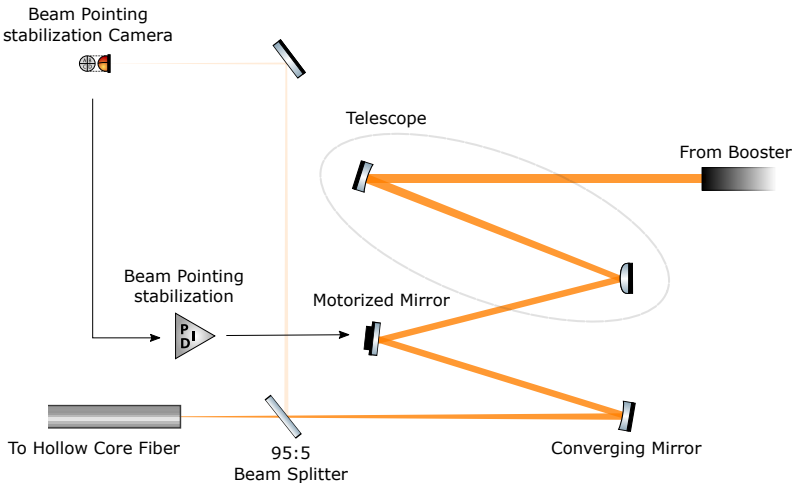

Figure 2.4: Path of the beam from the Booster output to the hollow core fiber. A telescope and a converging mirror set the spot size in the beam waist, while a feedback controller stabilizes the position of the beam at the entrance of the fiber.

entrance of the fiber, close to the focus of the beam. For this reason it is necessary to keep the entrance of the fiber at a sufficiently low pressure. To achieve this, the gas is injected at the output of the fiber, while the vacuum pump is connected to the entrance of the fiber, as seen in Figure 2.5. In this way the density of the gas through the chamber has a gradient, increasing along the direction of the beam: this configuration is called *differential pumping*. The pressure of He at the output of the fiber with this configuration is around 1 bar.

Figure 2.5: *Differential Pumping* scheme. The gas in injected close to the output of the fiber, while near to the entrance pressure is lower. Adapted from [30].

Figure 2.6 shows an example of spectral broadening performed in the lab. After the spectral broadening performed by the fiber, the pulse is chirped and needs to be compressed. For this purpose, there is a set of chirped mirrors before the XUV-IR interferometer. The aim is to get a pulse duration which

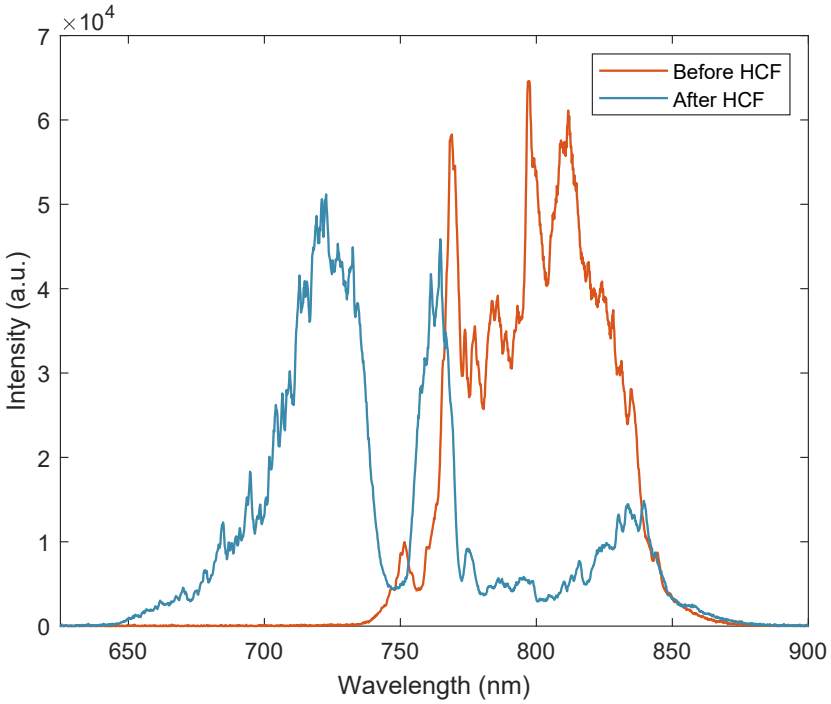

Figure 2.6: Spectra taken before and after the Hollow Core Fiber. It is possible to notice the spectral broadening performed by self-phase modulation phenomenon.

is as close as possible to the transform-limited one, which can be obtained by the spectrum. In fact, by assuming a gaussian envelope of the pulse, it is possible to derive:

$$\Delta\nu\Delta\tau \simeq 0.44 \tag{2.8}$$

where $\Delta\nu$ is the FWHM of the spectrum in frequency and $\Delta\tau$ the FWHM of the pulse envelope, in time. Given the shape of the spectrum, this relationship sets the shortest possible pulse.
A method to characterize the pulse after the chirped mirrors, in order to understand if our compression stage is working well enough, is to use the FROG technique, as explained in Appendix A. In the example shown here, we used the SHG-FROG. The pressure in the fiber was not very high (around $5 \cdot 10^{-1}$ mbar at the entrance of the fiber) such that the pulse was not the shortest we could achieve. In Figure 2.7 there is an example of a spectrogram taken in our laboratory. This spectrogram, analyzed through the iterative algorithm of FROG, gives a temporal shape of the electric field of the pulse. The result is shown in Figure 2.8, where the FWHM of the pulse was around 17 fs. However this setup can produce, by changing the gas pressure in the Hollow Core Fiber, evenr shorter pulses, with a duration of a few femtoseconds.

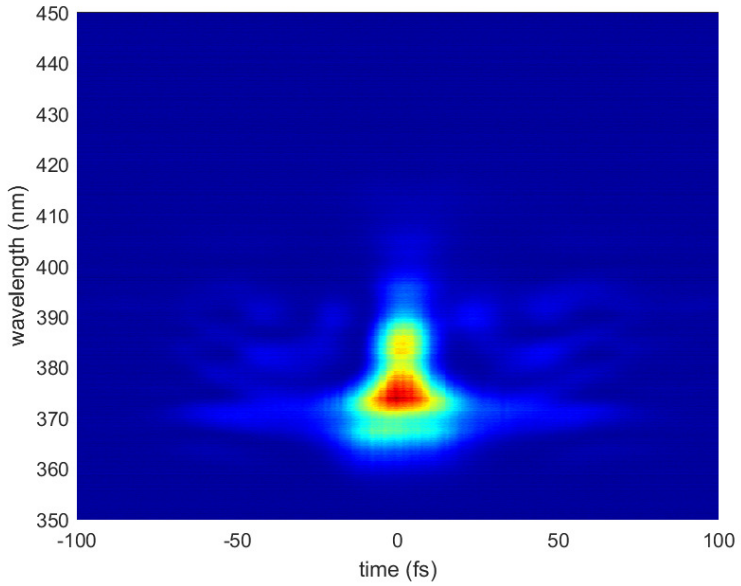

Figure 2.7: Example of a spectrogram, taken by using the second-harmonic FROG technique.

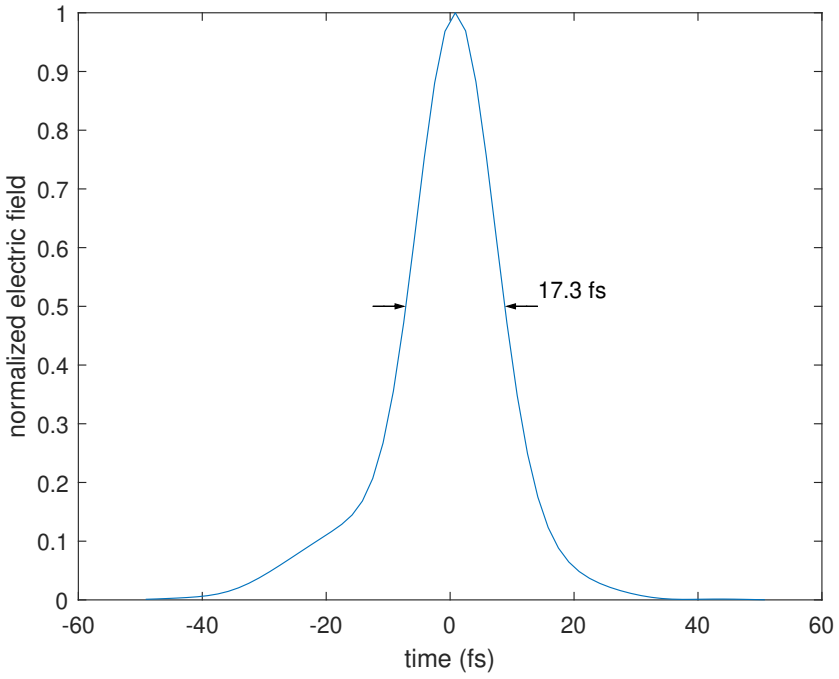

Figure 2.8: Example of reconstruction of a pulse through the FROG technique. This was not the shortest possible pulse we can obtain with a hollow core fiber, having a duration of around 17 fs.

2.4 XUV-IR Interferometer

After the broadening of the spectrum performed by the Hollow Core Fiber, the pulse is chirped and needs to be temporally compressed. This job is done by a set of chirped mirrors. Then, the beam is split into two parts: 70% of it is sent to the HHG chamber where it will generate XUV photons, while the remaining 30% is just propagated in order to be recombined to perform pump-probe experiments. The length of the IR branch can be modified by

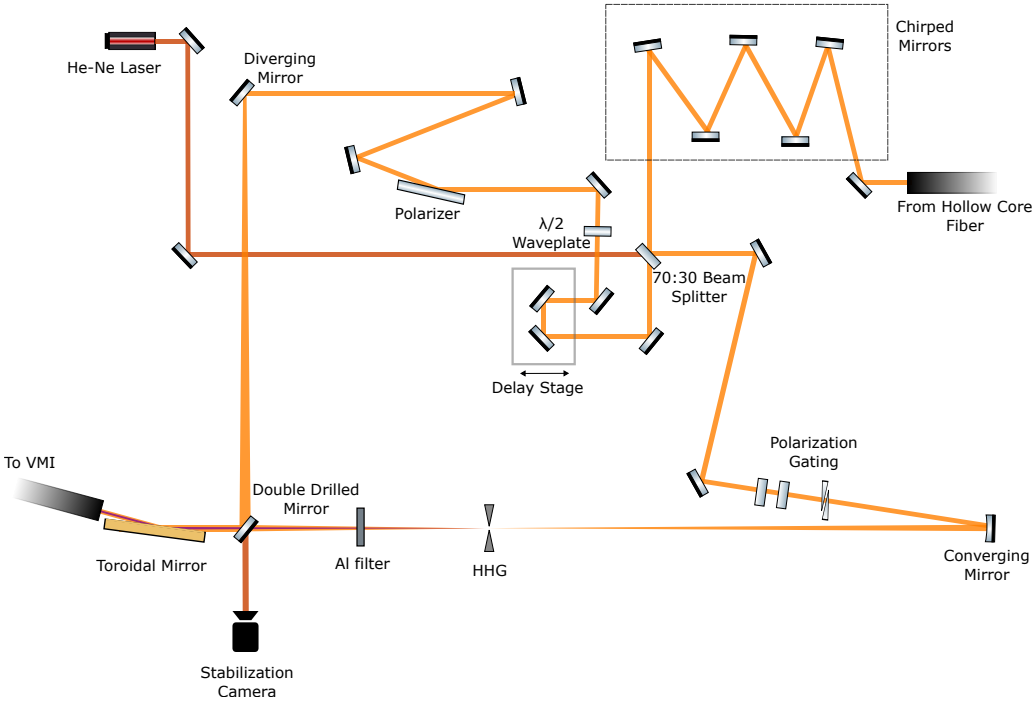

Figure 2.9: Setup sketch from hollow core fiber to VMI.

moving a delay stage, where a piezo motor provides a fine tuning of the delay. A $\lambda/2$ waveplate combined with a linear polarizer allows to control the power of the beam in this branch. In the XUV branch, a converging mirror focuses the beam in the position of the HHG cell. Before a converging mirror, a set of a birefringent quartz plate and a $\lambda/4$ waveplate allow for generating a single attosecond pulse through the Polarization Gating technique. A couple of fused silica wedges, placed after them, are used to compensate the dispersion while generating a single attosecond pulse. The gas cell for the HHG is mounted on a motorized stage, which allows for a fine alignment of the gas jet with the focus of the beam.

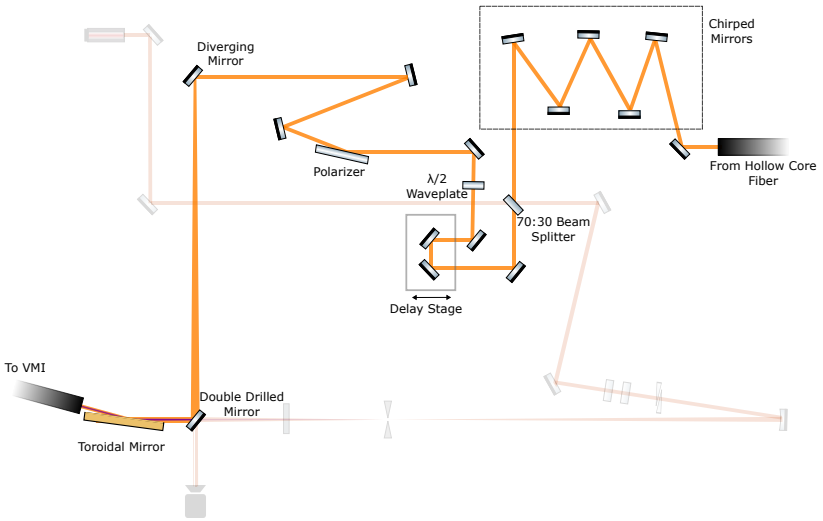

(a) IR path

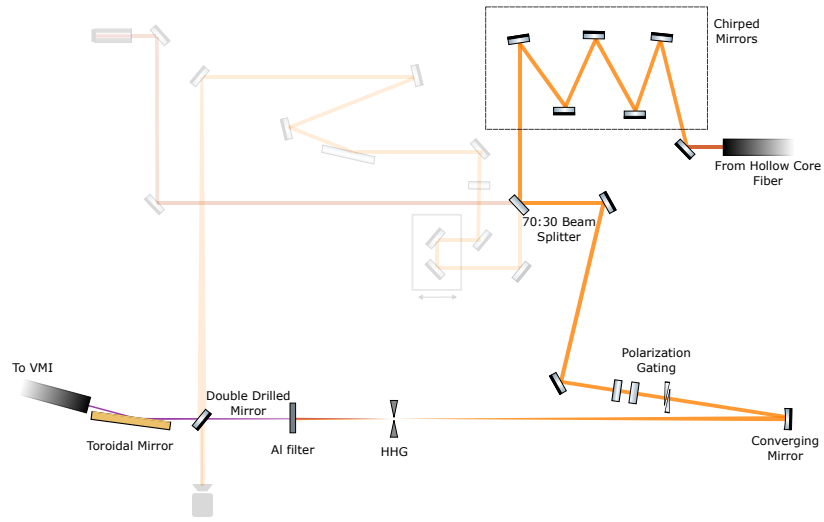

(b) XUV path

Figure 2.10: Sketches of the IR and XUV path. They are split by a beam splitter and recombined by a double drilled mirror before being focused by a toroidal mirror.

Harmonic Order	Photon Energy (eV)
11	17.48
13	20.66
15	23.84
17	27.02
19	30.20
21	33.38
23	36.56
25	39.74
27	42.92

Table 2.1: Values of photon energy of different odd harmonics of the fundamental frequency. In our setup, the wavelength of the IR radiation used for HHG is around 780 nm corresponding to a photon energy of 1.59 eV. This leads to photon energies listed in this table.

2.5 Delay Stabilization

To compensate the relative variation of the lengths of the XUV and IR branches, an interferometric approach is used. We used a He-Ne laser, with a wavelength of 633 nm, which follows the same path as the main beam in the XUV-IR interferometer.
Since on the XUV branch an Al filter is needed to cut the residual IR coming from the HHG, the He-Ne laser beam wouldn't be able to reach the double-drilled mirror too. For this reason, we mounted the Al filter on a drilled piece of glass, such that the external part of the beam in still able to pass through the glass, not being blocked by the Al filter. This way, just a ring of the He-Ne beam reaches the double drilled mirror. Anyway, this is enough to interfere with the spot of the beam coming from the other branch which passes through the hole of the double-drilled mirror.
The recombined beams are then sent to a camera. In the region where they are overlapped, they produce interference fringes. Those fringes move with the variation of the difference of the path length, and a PID feedback system allows for following these variations and compensate for them. As part of this thesis, we developed a program with the LabView platform whose purpose was to follow those fringes and reduce as much as possible the RMS phase shift. Some screenshots of this program are shown in Figure 2.12, where it is possible to see the interference pattern of the He-Ne laser, a plot of these fringes and their Fourier transform. Also, the behaviour of the phase shift in time during the stabilization is shown.
The feedback system made use of the delay stage, which is a slit whose move-

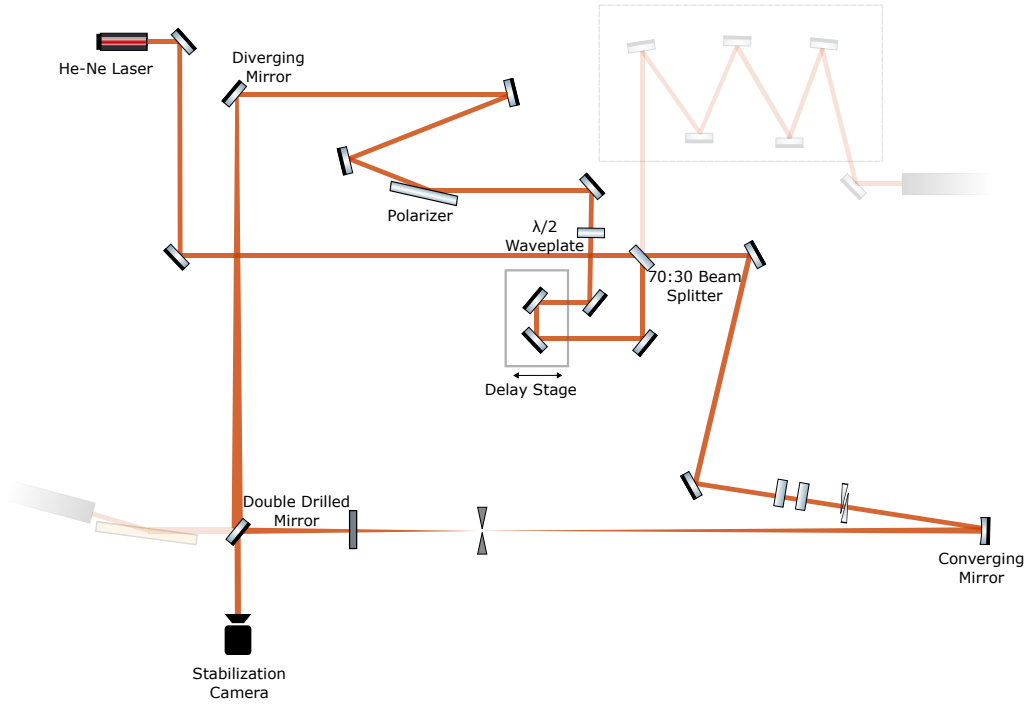

Figure 2.11: HeNe interferometer for delay stabilization.

ments can be finely controlled. Together with a tuning of the parameters of the PID controller, allowed us to obtain a stabilization of the pump-probe delay of the order of few tens of attoseconds, which is enough for attosecond time-resolved experiments like the ones which this setup has been built for. In Figure 2.13 it is possible to see a measurement of the residual phase shift during about 3.5 hours, while the stabilization was active. The residual phase shift RMS in time is, in this example, around 23 as.

2.6 VMI Spectrometer

2.6.1 Experimental Setup

The Velocity Map Imaging (VMI) spectrometer relies on a static electric field used to accelerate ions or electrons, sending them to a detector. The structure used to generate the electric field is shown in Figure 2.14. The laser beam passes between the extractor and repeller, perpendicular to the gas jet. The voltages of both extractor and repeller can be adjusted in order to get different focusing properties out of this structure. At the end of the flight tube, a 2D position sensitive detector allows to also get information about

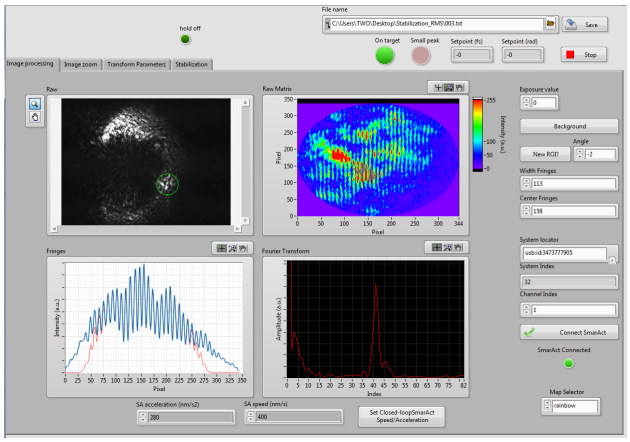

(a) In this page it is possible to see the image on the camera, the plot of the fringes and its Fourier transform.

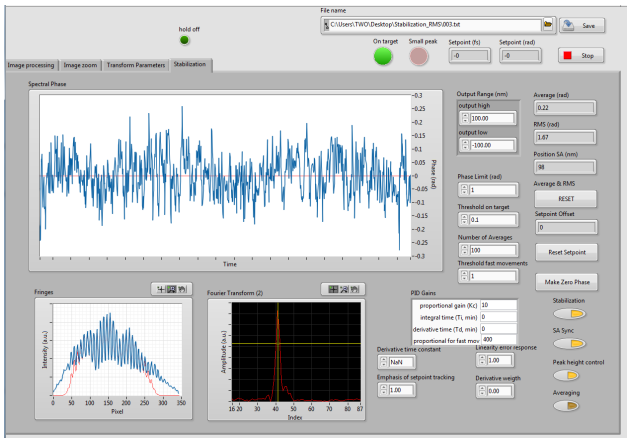

(b) In this page there's a plot of the phase shift during time, while stabilized.

Figure 2.12: Screenshots of the program we used to acquire, analyze and follow the fringes coming from the interference of the He-Ne.

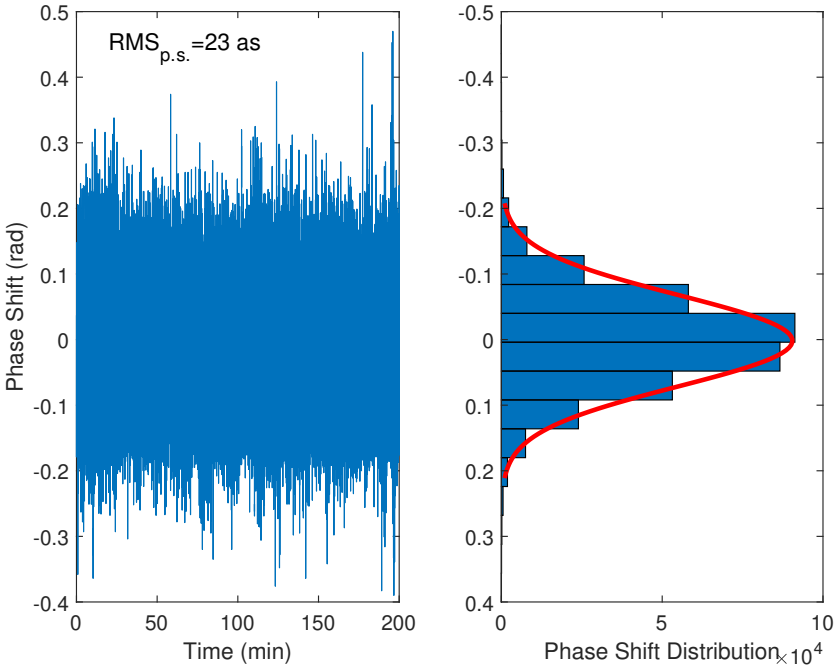

Figure 2.13: Residual phase shift during stabilization.

the angular distribution of emitted electrons. It consists of a phosphor screen, coupled with a MCP which ampifies the signal coming from the laser-particle interaction. A CCD camera is placed in front of the screen in order to acquire and analyze the images.
In our VMI the MCP has a diameter of 75 mm and it is able to operate in two ways: in *DC-mode* or *gating-mode*. In *DC-mode* the MCP-out and phosphors are driven with constant voltages around 1.8 kV and 3.8 kV, values which ensure the best gain that it can support. In the *gating mode*, the MCP-out and phosphor are kept at 1 kV less. Then, in a finite time window, typically around 200 ns, a 1 kV step is applied. A capacitor between MCP-out and phosphor keeps the voltage difference between them constant. Finally, by measuring the current flowing through the phosphors, it is possible to follow the charge collection in time to obtain a Time-Of-Flight spectrum of the emitted particles. This operation mode is therefore useful to select only fragments with a certain m/q ratio. This is the case of ions TOF measurements when a photofragmentation experiment is performed in a bio-relevant molecules, as explained in Chapter 4.

2.6.2 Working Principle

Let's assume the reference frame in Figure 2.15. The z-axis is the axis of

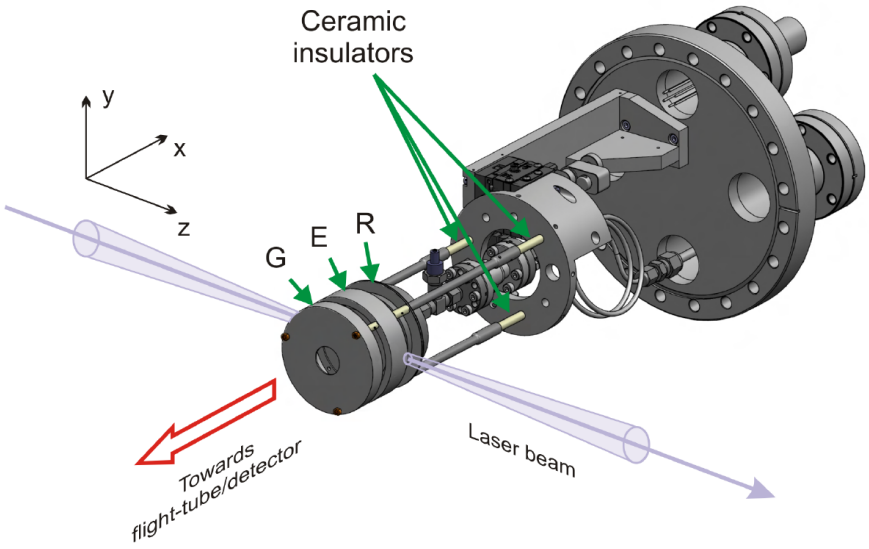

Figure 2.14: Structure of the electrostatic lens of VMI. It is made of a repeller (R), an extractor (E) and a ground plate (G). The laser beam passes between the extractor and the repeller. Adapted from [18]

propagation of the laser beam, while the x-axis is the direction of propagation of the photofragments. The assumption behind the following model is a cylindrical symmetry of the $v_{3D,yz}$ velocity, that means that the polarization of the light is along y. When a particle with mass m and charge q is emitted in the interaction region, it gets accelerated by the extracting field along the x-direction, thus not changing its component on the y-z plane. Then, particles with the same y-z initial velocity are focused on the same circle of radius

$$R = v_{3D,yz}t \tag{2.9}$$

Then, if V_s is the voltage difference between the interaction region and the detector, it is possible to write v_x as

$$v_x = \sqrt{\frac{2qV_s}{m}} \tag{2.10}$$

Then, since the acceleration region is much smaller then the length of the tube, it is possible to assume that

$$t \simeq \frac{L}{v_x} = L\sqrt{\frac{m}{2qV_s}} \tag{2.11}$$

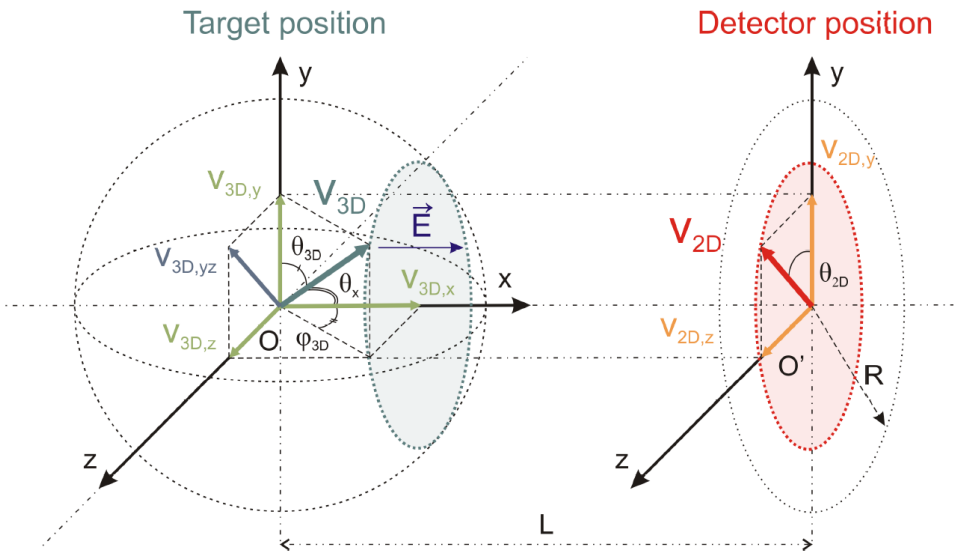

Figure 2.15: Reference system used to model the propagation of the electrons or photofragments from the interaction region to the 2D detector. Adapted from [18]

and then

$$R = v_{3D,yz} L \sqrt{\frac{m}{2qV_s}} = L\sqrt{\frac{T_0}{qV_s}} \tag{2.12}$$

where T_0 is the initial kinetic energy on the y-z plane.
From Eq. 2.11 it is possible to see that the VMI is useful to get Time-Of-Flight spectra, because the arrival time is proportional to mass-to-charge m/q ratio. For example, in a pump-probe experiment on biomolecules the useful information is a TOF spectrum done with ions. The VMI can then work also in this case. Eq. 2.12, instead, shows why the 2D image on the phosphors screen provides an additional information: the radius of the circle where the photofragments are focused depends on the square root of the initial kinetic energy on the plane parallel to the plane of the 2D detector.

2.6.3 Abel Inversion

In order to retrieve the 3D spatial distribution of emitted electrons/ions from the 2D image obtained as previously described, it is possible to exploit a mathematical tool provided by the Abel transform.
In order to understand the geometrical meaning of this transform, let's start with a the 2D Abel transform. To be coherent with the expansion in the three-dimensional case that will follow, let's consider two axis that form a

$x - z$ plane and a function $f(x, z)$ which is circularly symmetric:

$$f(r) = f(\sqrt{x^2 + y^2}) \tag{2.13}$$

By defining an integral

$$F(z) = \int_{-\infty}^{+\infty} f(\sqrt{x^2 + y^2})dx \tag{2.14}$$

a function is obtained which only depends on the y coordinate and which represents the sum of the contribution of the function at a given z, scanning all the possible values of x. By applying a simple substitution to this integral, where $r^2 = x^2 + z^2$, and so $x = \sqrt{r^2 - z^2}$, the integral becomes

$$F(z) = 2\int_{|z|}^{+\infty} f(r)\frac{r}{\sqrt{r^2 - z^2}}dr \tag{2.15}$$

which represents the 2D Abel transform written in terms of the distance r with respect to the origin.
A generalization of this transform in the three-dimensional case, and more specifically in the case of interest for the VMI spectroscopy, is the one described in Figure 2.15. Assuming a cylindrical symmetry of the initial velocity v_{3D}, with the symmetry axis parallel to the plane of the detector, on the $x-z$ plane, at a fixed y value, the situation is exactly the two-dimensional that was previously described, where the function that describes the initial velocity of the photofragments/photoelectrons is circularly symmetric and the symmetry coordinate is $\rho = x^2 + z^2$. So it is possible to define, for each slice at a fixed value of the y-coordinate, to define an Abel projection

$$G_n(z) = 2\int_{|z|}^{+\infty} f(\rho)\frac{\rho}{\sqrt{\rho^2 - z^2}}d\rho \tag{2.16}$$

which represents the 2D image collected on the detector of the VMI. By applying, slice by slice, the inverse Abel transform:

$$f_n(\rho) = \frac{1}{\pi}\int_{\rho}^{+\infty} \frac{dG_n(z)/dz}{\sqrt{z^2 - \rho^2}}dz \tag{2.17}$$

where n is the index which scans each slice. Then, by applying this inverse transform it is possible to retrieve the initial 3D distribution of velocity. Anyway, the numerical integration of the integral in Eq. 2.17 is not trivial, due to the derivative at the numerator and to the singularity of the integrand.

2.6.4 Abel Inversion Through Legendre Polynomial Expansion

One possible way to perform the inversion of two-dimensional images is interesting since it immediately connects with the physics of this process. The photoemission is a result of the interaction between matter and light, and it is known that the angular distribution can be expanded as in terms of Legendre polynomials, where the highest-order polynomial is determined by the order of the multi-photon ionization process [18]. So, the 3D moment distribution can be described as

$$\mathbb{P}_{3D}(v_{3D}, \theta_{3D}, \varphi_{3D}) = \sum_l a_l(v_{3D}) P_l(\cos(\theta_{3D})) \tag{2.18}$$

By exploiting the normalization of this distribution, through

$$\begin{aligned} &\iiint \mathbb{P}_{3D}(v_{3D}, \theta_{3D}, \varphi_{3D}) v_{3D}^2 \sin(\theta_{3D}) d\theta_{3D} d\varphi_{3D} dv_{3D} = 1 = \\ &= \iint \mathbb{P}_{3D}(v_{3D}, \theta_{3D}) d\theta_{3D} dv_{3D} \end{aligned} \tag{2.19}$$

it is possible to obtain the three-dimensional angular distribution as a function of only v_{3D} and θ_{3D}, as

$$\mathbb{P}_{3D}(v_{3D}, \theta_{3D}) = 2\pi v_{3D}^2 \sum_l a_l(v_{3D}) P_l(\cos(\theta_{3D})) \sin(\theta_{3D}) \tag{2.20}$$

Exploiting the fact that

$$\mathbb{P}_{3D}(v_{3D}, \theta_{3D}) d\theta_{3D} = \mathbb{P}_{3D}(v_{3D}, \cos(\theta_{3D})) d(\cos(\theta_{3D})) \tag{2.21}$$

we can also retrieve the angular distribution as a function of $\cos(\theta_{3D})$ instead of θ_{3D}:

$$\mathbb{P}_{3D}(v_{3D}, \cos(\theta_{3D})) = 2\pi v_{3D}^2 \sum_l a_l(v_{3D}) P_l(\cos(\theta_{3D})) \tag{2.22}$$

This last expression, together with $\mathbb{P}_{3D}(v_{3D}, \theta_{3D}, \varphi_{3D})$ are constant, as a function of $\cos(\theta_{3D})$ in the first case and θ_{3D} in the last one, for isotropic angular distribution. Conversely, $\mathbb{P}_{3D}(v_{3D}, \cos(\theta_{3D})) \sim \sin(\theta_{3D})$, always for isotropic angular distribution. Considering now the detector plane, it is possible to connect v_{2D} to two components of v_{3D}:

$$\begin{cases} v_{3D,y} = v_{2D} \cos(\theta_{2D}) \\ v_{3D,z} = v_{2D} \sin(\theta_{2D}) \end{cases} \tag{2.23}$$

where θ_{2D} is the angle with respect to the y axis on the impingement plane. Also here it is possible to describe the 2D projection as a superposition of Legendre polynomials, using different weights:

$$\mathbb{P}_{2D}(v_{2D}, \theta_{2D}) = \sum_l b_l(v_{3D}) P_l(\cos(\theta_{2D})) \tag{2.24}$$

where, due to cylindrical symmetry, even though $\theta_{2D} \in [0, 2\pi)$, the 2D momentum distribution is identical in $\theta_{2D} \in [0, \pi)$ and in $\theta_{2D} \in [\pi, 2\pi)$.
So, according to the description developed up to here, the Abel projection becomes a transformation between $\mathbf{a}$ and $\mathbf{b}$

$$\mathbf{b} = \mathbf{M}\mathbf{a} \tag{2.25}$$

where $\mathbf{a}$ and $\mathbf{b}$ are the vectors containing the weigths for each order of the Legendre polynomials and $\mathbf{M}$ is the transformation matrix, which only depends on the number of velocity points and on the maximum order of polynomials, not depending on the specific experiment. So, once $\mathbf{M}$ and $\mathbf{M}^{-1}$ have been determined, they can be used to invert any image. In fact, the 3D Legendre polynomial expansion can be easily determined through

$$\mathbf{a} = \mathbf{M}^{-1}\mathbf{b} \tag{2.26}$$

In order to derive $\mathbf{M}$ analytically, one can observe that v_{2D} and the projection of v_{3D} along the y axis are, respectively

$$\begin{cases} v_{2D} = v_{3D}\cos(\theta_x) \\ v_y = v_{3D}\cos(\theta_{3D}) \end{cases} \tag{2.27}$$

To find a connection between the 3D distribution and its projection on the two-dimensional detector, let's consider the incremental flux that is detected around a point defined by v_{2D} and θ_{2D}:

$$\delta S_{2D} = \mathbb{P}_{2D}(v_{2D}, \theta_{2D}) v_{2D} \delta v_{2D} \delta\theta_{2D} \tag{2.28}$$

Its equivalent on the 3D sphere is given by

$$\delta S_{3D} = \mathbb{P}_{3D}(v_{3D}, \theta_{3D}, \varphi_{3D}) v_{3D} \delta\theta_x v_{2D} \delta\theta_{2D} \tag{2.29}$$

Since $\delta S_{2D} = \delta S_{3D}$,

$$\mathbb{P}_{2D}(v_{2D}, \theta_{2D}) = v_{3D} \frac{\delta\theta_x}{\delta v_{2D}} \mathbb{P}_{3D}(v_{3D}, \theta_{3D}, \varphi_{3D}) \tag{2.30}$$

and this expression defines the matrix $\mathbf{M}$. Then the procedure to retrieve the 3D distribution from a 2D projection is clear:

1. Cast the 2D results as a superposition of Legendre polynomials, that is find the set of b_l

2. Invert $\mathbf{b}$ through $\mathbf{a} = \mathbf{M}^{-1}\mathbf{b}$ thus finding the set of weights that define the Legendre polynomial expansion of the 3D momentum distribution

It is known that for a process where charged particles are created as a result of light-matter interaction the angular distribution can be written in terms of the so called β-moments:

$$\mathbb{P}(E, \cos(\theta)) = \sigma(E)\Big[1 + \sum_{n\geq 2} \beta_n(E) P_n(\cos(\theta))\Big] \tag{2.31}$$

where the β-moments are defined, according to the discussion developed up to here, as

$$\beta_n = \frac{a_n(v_{3D})}{a_0(v_{3D})} \tag{2.32}$$

and $\sigma(E)$ is the cross-section of the process. Once again, by retrieving the set of $\{a_n(v_{3D})\}$ it is possible to retrieve the angular distribution of photoemission.

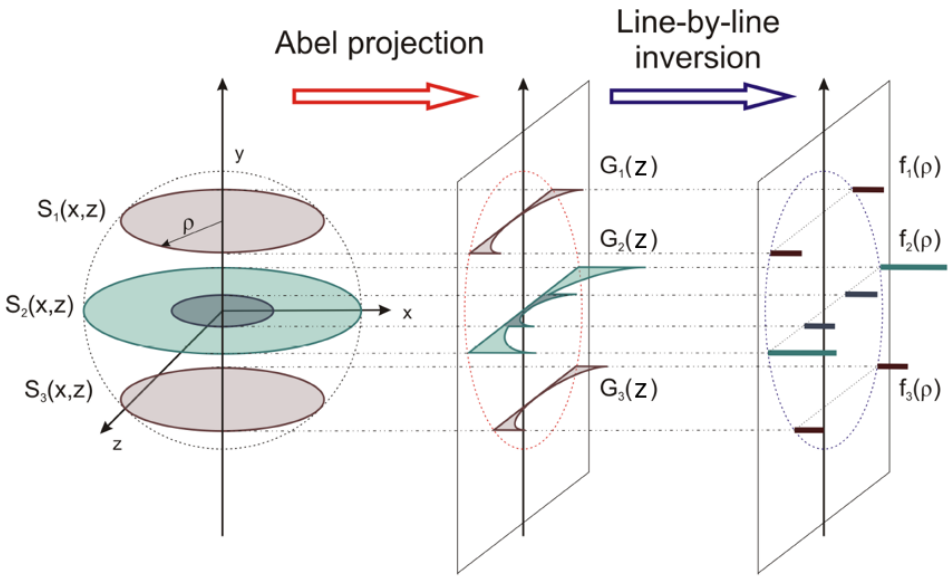

Figure 2.16: Sketch of the Abel projection. Adapted from [18]

Chapter 3

Biomolecular Source

In this chapter the part of the experimental setup devoted to the generation of gas phase biomolecules jet is presented. Starting from the motivation for experiments in gas phase, the focus will move to the design of the biomolecular source and to the way the molecular jet is generated. Finally, some experiments whose objective was to characterize the source are shown.

3.1 Aim

Life sciences deal with processes which regulate the biological mechanisms of life itself. A lot has been understood, such as which molecules are involved in many of these processes. Among them it is possible to recognize processes where the interaction between a molecule and light is relevant, such as photosynthesis or the interaction between the DNA and UV or X-ray light. This is exactly what can be investigated with laser light, which provides a quite wide range of tunability of the spectrum and makes both a static and a time-resolved analysis possible. As far as our work is concerned, ultrashort laser pulses allow to follow the electronic motion of relevant biological molecules after a light-induced perturbation, and this could be of great importance for the development of the previously cited branch of science since it could make possible to understand, and ultimately steer, the reactions involved in biological mechanisms. Although the natural medium of most of these molecules is water-based, it is also extremely interesting to understand their behaviour in an isolated environment, such as in gas phase. This allows for (i) simplifying the understanding of the dynamics as interactions with the solvent are inhibited; (ii) providing a testbed for theoretical tools. This knowledge will, hopefully, help the understanding of biomolecular assemblies and, eventually, *in-vivo* structures.

The idea of studying molecules of biological interest in the gas phase, such as DNA bases or amino acids is quite new and was made feasible by technological developments, including ultrafast spectroscopy [26]. By using ultrafast laser pulses, it is possible to study the intramolecular processes in time, following them with the correct time resolution. Ha-Thi et al., for example, were able to discover an ultrafast intersystem crossing in copper porphyrins, a characteristic structure of hemoproteins which have a metal containing porphyrines as cofactors, and this was something unprecedented for organic molecules [29]. They made use of a VMI, concluding that, even though the resolution was worse than a TOF spectrometer, it provides a better efficiency for weak signals such as those coming from molecules. A decay time of the order of 100 fs was observed with the same kind of experimental setup in metalloporphyrins [16].
Bringing intact molecules in the gas phase is a challenging goal. Actually, most of the molecules of biological interest are non-volatile compounds. Moreover, they usually decompose upon heating. Then specific vaporization methods have to be used. Different techiniques have been implemented in order to transfer the molecules in the interaction region into the gas phase. For example, *soft vaporization* methods such as Electro-Spray Ionization (ESI) produce a gas of singly or multiply charged ions. Matrix Assisted Laser Desorption Ionization (MALDI) releases molecules from small charged droplets. An alternative is given by Laser Desorption/Ionization methods (LDI), such as Laser Induced Thermal Desorption (LITD), which was used in our laboratory in order to perform experiments with phenylalanine [3] and tryptophan [14]. Another technique consists of an aerosol thermodesorption (TD), which produces a lower molecular density and a strong water background signal. The method we used in our laboratory is an oven-based Resistive Heating (RH), which allows to get neutral molecules in the interaction region.
After having been evaporated through the oven-based heating, the molecules have to be carried to the interaction region. This can be done in two ways: in the case of *effusive* sources the molecules are not guided by any gas jet but they just effuse into the experimental volume, collimated by a beam collimator. Here, the distribution of the velocity of the molecular beam is quite wide and, due to the heating process, most of the molecules are not anymore in the lowest-energy conformation, which could be detrimental from the experimental point of view. An alternative is given by *nozzle* sources, where a supersonic gas jet acts as a carrier for the molecules. This is the case in our experimental setup, where a noble gas like helium or argon was used for the jet. A nozzle source is a more effective one, since the supersonic expansion of the noble gas not only carries the molecules but also cools them down by inelastic collisions, in which the internal energy of the molecules is converted

into kinetic energy of the noble gas atoms. This is important in order to deal with a molecule in its ground state during a pump-probe experiment.

3.2 Setup

3.2.1 Oven and Valve

A preliminary version of a biomolecular source has been employed in our laboratory for experiments with phenylalanine and tryptophan [6]. As part of this thesis, I have helped to build a new design of the source with a different oven and a diverse approach to vaporize the molecules. With this new design we aimed at overcoming some of the drawbacks of the former system. For example the nozzle could easily clog since, if the heating was too fast, the hot molecular vapour coming to the colder nozzle could condense. The concept of this new oven is to mix the molecule with graphite powder and press it under 2-2.5 ton with a hydraulic press, thus creating a pellet. All around the pellet, a Thermocoax metallic resistive coil is used to heat the sample up to $150 - 250$ °C, depending on which molecule has to be analyzed. It is important to notice that the temperature was measured with a Thermocoax thermocouple placed in a hole on the metallic plate below the oven. Even though this method doesn't provide the exact temperature of the sample, it is a good and replicable reference.

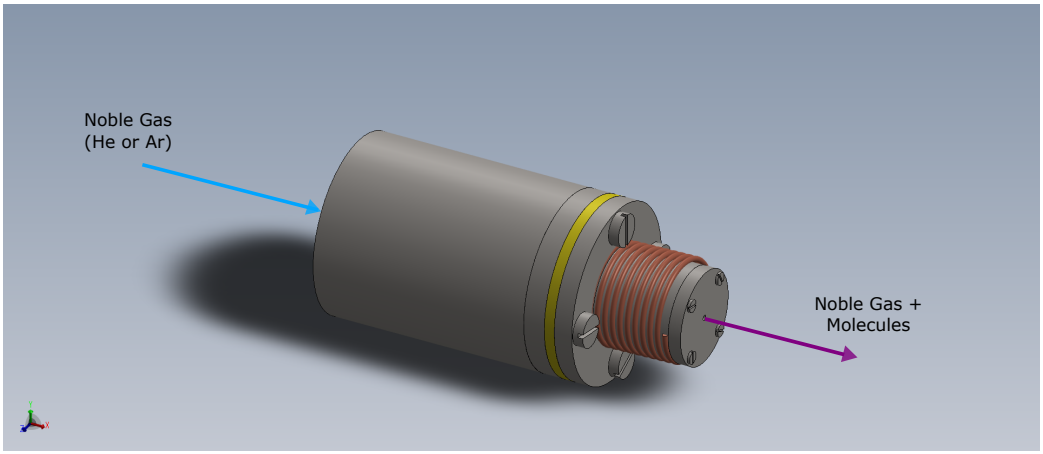

Figure 3.1: Here it is shown the mounted valve and oven system. The pressured noble gas coming from the bottle enters the oven when the pulsed valve is open, collects the molecular vapour inside the oven and brings it outside the source, where it will pass through the skimmer and will finally reach the interaction chamber. In light blue, the noble gas beam. In purple, the molecular beam.

Since the pulsed valve has a temperature working range which does not go beyond 100 °C, an insulator plate is placed between the oven and the valve. Initially, in order to try keeping the temperature of the valve as low as possible, we mounted a water cooling system around the metallic shield which covers the pulsed valve. This system consisted of a coil made with a copper tube, in order to maximize the thermal conduction with the metallic shield. Anyway, this system was quite bulky and created some problems during the daily setup of the source. For this reason we decided to use it only when it is absolutely necessary to cool the valve and, even without this system, we didn't observe any misfunctioning in the valve when the temperature of the oven raised up to $\sim$ 250 °C.
As far as electronic control is concerned, the Parker valve operates at a maximum repetition rate of 100 Hz, which is synchronized with the laser. Details on the electronics, synchronization scheme and data acquisition are discussed in Chapter 4.

3.2.2 Nozzle Source

The effectiveness of a nozzle source has been shown by Lietard et al. [17], by characterizing the velocity distribution of a gas jet driven by either helium or argon and recording photoionization images of hydroxypyridine with a VMI. Both the oven and the detection scheme were technically the same as in our laboratory. Raw photoionization images acquired with a VMI and gated to observe the signal coming only from the molecule are shown in Figure 3.3. They were taken with a pressure of helium/argon of 6 bar at the valve, and the different images correspond to different delays between the aperture of the valve and the acquisition of the signal, going from 0.2 to 30 ms. By analyzing those images it was possible to obtain a map of the velocity distribution of hydroxypyridine molecular beam, as shown in Figure 3.4. Those images show many differences in the distribution between helium and argon, even being the pressure in the reservoir equal. Anyway they both show, until about 0.3 ms, a distribution around 200 m/s corresponding to an effusive beam. When the valve opens and the pulse reaches the interaction region, the molecular beam driven by helium shows a peak at a much higher velocity with respect to argon, around 1800 m/s while argon peak is around 500 m/s. Moreover the distribution in the case of helium is much narrower, indicating a lower final temperature. In both cases, after the peak the width of the distribution widens, indicating that the final temperature will be higher.
The analysis at short delays showed a feature at high velocities followed by a depletion of the high velocity component until about 1 ms. This surprising feature seems to indicate the presence of a shockwave in the oven immediately

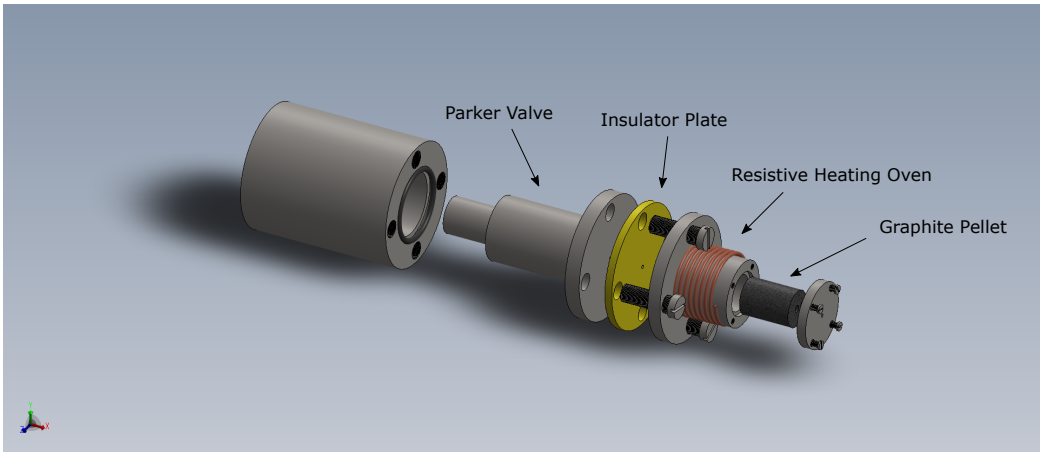

(a) Exploded view of the pulsed valve and oven. It is possible to distinguish the valve, the insulator plate and the heating coil around the pellet.

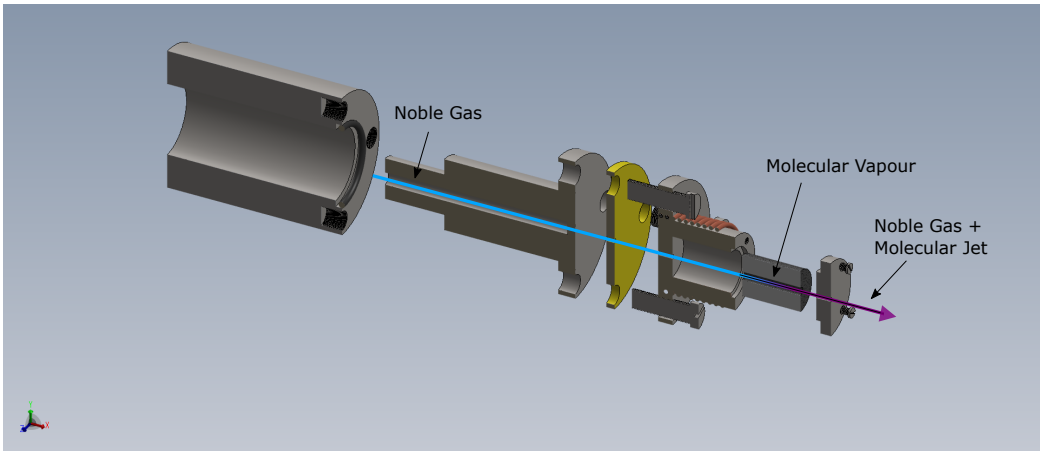

(b) Exploded cross section view of the valve and oven system. In light blue, a drawing of the path of the noble gas. In purple, the noble gas and molecules jet. The gas coming from the valve meets the molecular vapour inside the graphite pellet and brings it outside.

Figure 3.2: Exploded views of the whole valve and oven system.

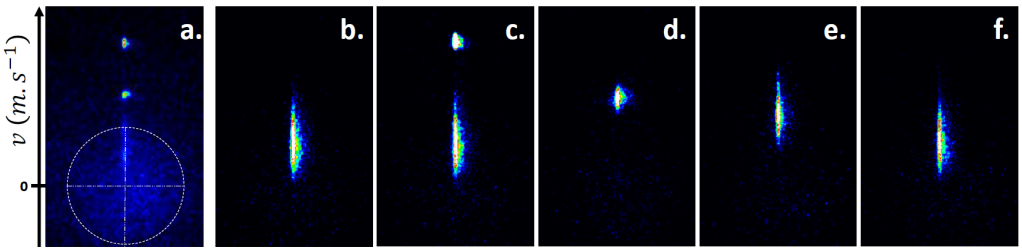

Figure 3.3: Raw PI hydroxipyridin images acquired at variable delay with respect to the valve opening. Carrier gas was argon at 6 bar. The images were gated so that only the signal coming from the molecule was recorded. Adapted from [17].

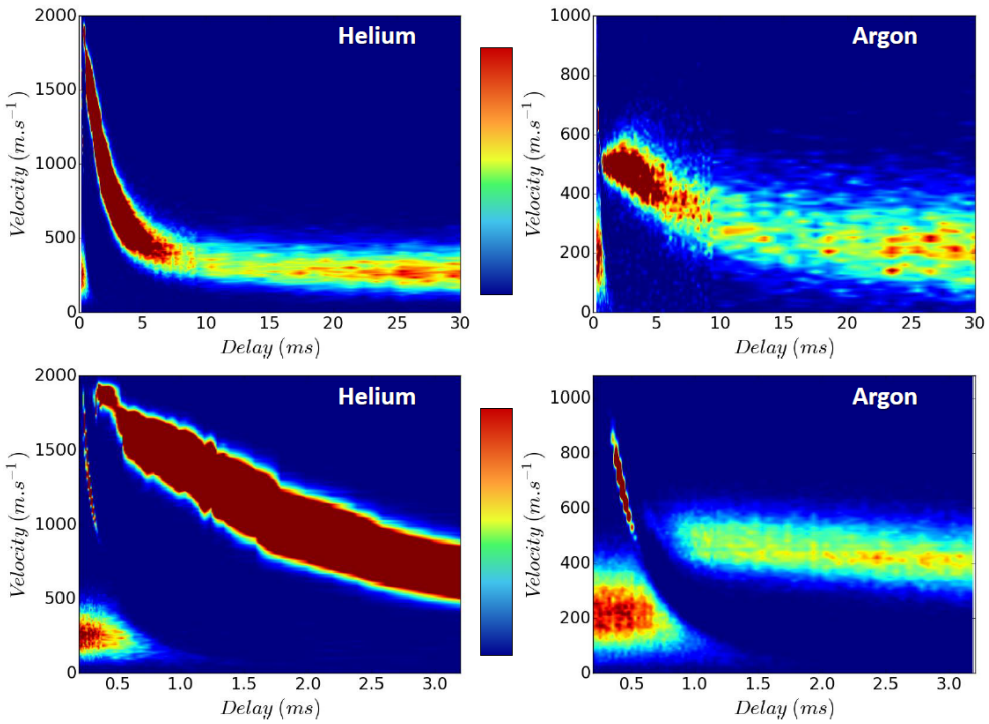

Figure 3.4: Velocity distribution maps of the molecular beam as a function of the delay with respect to valve opening. The lower images show a zoom around the first milliseconds after the aperture of the valve. Adapted from [17].

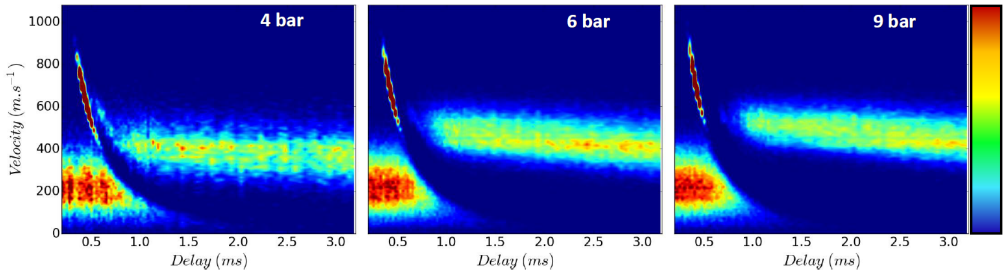

Figure 3.5: Map of the velocity distribution at short delays at different reservoir pressures. The images were recorded with a pressure of 4, 6 and 9 bar.

after the valve opening.
Finally, the dependence of this distribution on the reservoir helium/argon pressure was analyzed. The result obtained with pressures of 4, 6 and 9 bar is shown in Figure 3.5. As expected, the average velocity slightly increases and an increase in the velocity corresponding to the shockwave is also observed. This work have shown that nozzle sources are effective and narrow velocity distributions can be obtained, especially by working at a short delay (i.e. few ms) with respect to the valve opening.

3.2.3 Graphite Pellet

The reason why it is so important to find a matrix material is that most of the molecules of biological interest are non-volatile compounds, and they usually decompose upon heating. A matrix material, then, minimizes the risk of occluding the nozzle. A good material for such a purpose should be apolar, unreactive, a good heat conductor and should allow to be easily compressed. Moreover, it should not vaporize in the working temperature range scanned during the experiment. Graphite, for example, complies with all this requirements and has already been tested as a good matrix material for fragile molecules [23]. It does not vaporize until 1000 °C and its porousness makes the vaporization of molecules possible. Moreover, graphite protects the heated compound from oxidation.
In our setup, the graphite pellet is built with a hole in the center corresponding to the outlet of the valve, such that the gas coming from this valve passes through the hole. When the oven is heated up, the molecules vaporize in the center of the pellet so that the gas jet carries them away from it. The path of the gas jet is described in Figure 3.2. The pellet was prepared by mixing the graphite powder with the molecule, with a ratio of about 10% molecule - 90% graphite. In our experiments, we mixed $200 - 300$ μg of molecular powder

with around 2 g of graphite.
The heating of the sample is provided by a Thermocoax resistive coil and the temperature is measured by a Thermocoax thermocouple. In order to keep the temperature constant during the experiment, both the thermocouple and the resistive coil are connected to a controller. By setting a temperature, this system opens and closes the resistive coil circuit when the temperature goes beyond or below the set point, respectively. The minimum deviation of the temperature which is needed to open or close the circuit is settable, with a minimum value of 0.1 °C.

3.2.4 Service and VMI Chambers

The valve and oven are mounted on the lower end of the biomolecular source (see Figure 3.7). This source is mounted inside a service chamber, shown in Figure 3.6. The service chamber is mounted on the top of the VMI chamber, where the interaction between the laser pulses and molecules happens. For this reason, a manipulator on the biomolecular source allow to shorten or extend the length of the source. This way, it is also possible, when needed, to close a gate valve. This valve isolates the VMI chamber with respect to the service chamber, which is important since the two chambers are both kept in high vacuum and, in order to periodically change the sample, the service chamber has to be opened frequently. Since the delicate components of the VMI chamber, such as the MCP, should always be kept in high vacuum (around 10^{-7} - 10^{-8} mbar) to lower the risk of damaging it, we minimize the number of times the VMI is vented thanks to this valve.
When a new sample had to be reinstalled in the oven in order to be analyzed, the oven was retreated from the skimmer using the manipulator until the whole source was above the level of the gate valve. This valve was then closed and the service chamber vented. Once the sample was mounted in the oven, the source was put inside the service chamber again and the pressure brought back to high vacuum (around 10^{-7} mbar). When the pressure of the service and VMI chambers were similar, the gate valve could be opened and the source was lowered close to the skimmer, which is placed between the two chambers and is used to select the central part of the molecular jet, as explained in the next chapter. The alignment between the oven and the skimmer is achieved with a translation stage with two degrees of freedom on the top of the source.

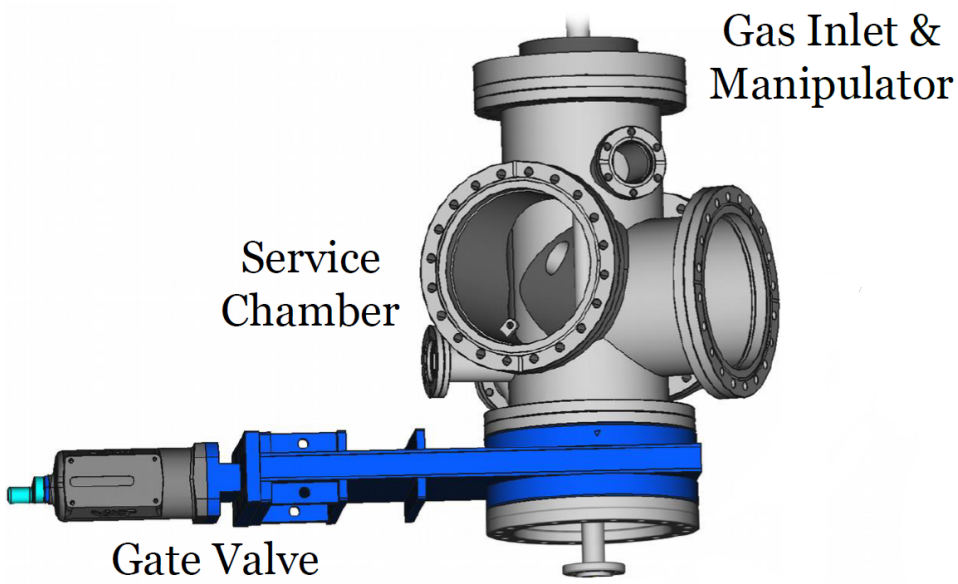

Figure 3.6: 3D view of the service chamber, which is built in order to be mounted above the VMI. The gate valve, drawn in blue, can keep the two chambers isolated. Adapted from [6]

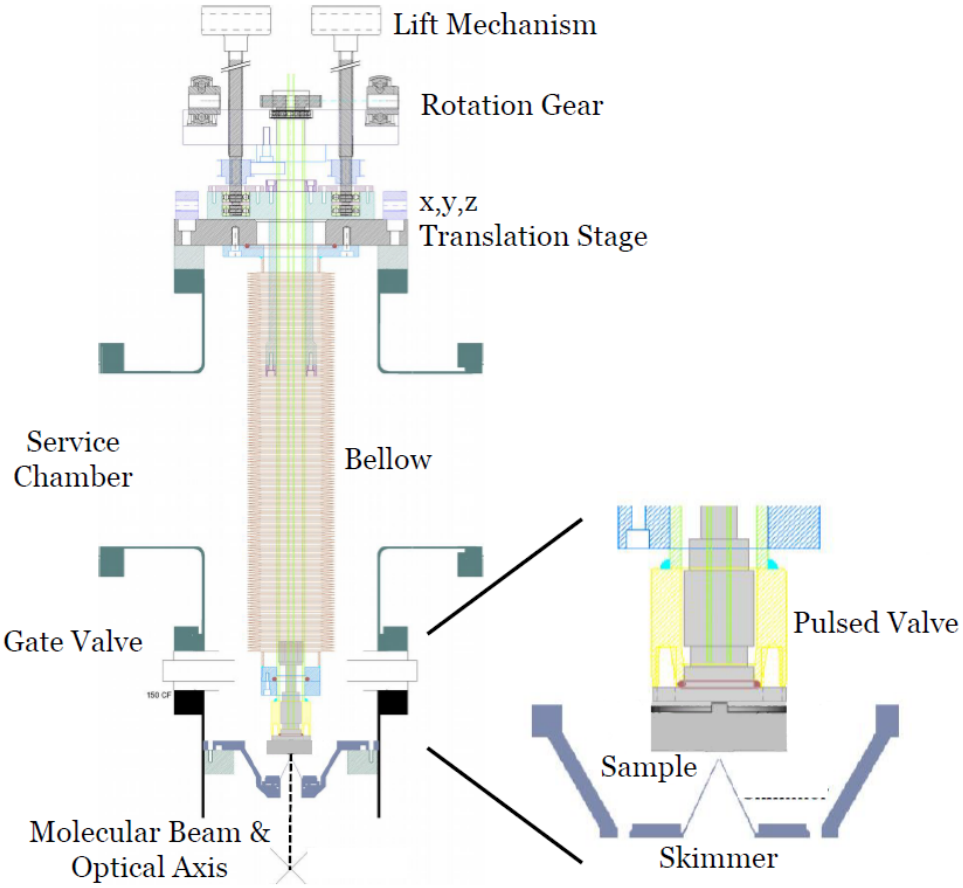

Figure 3.7: Drawing of the biosource. Adapted from [6]

Chapter 4

Characterization of the BioSource

This chapter is devoted to the description of the experiments that we performed in order to characterize the source, once mounted. More specifically, the chapter will be divided into various sections, dealing with:

- the electronics used to connect and synchronize the various components
- the synchronization between the laser pulse and the acquisition trigger
- the characterization of the gas jet produced by the pulsed valve
- the calibration of the overlap between the pump and the probe signals
- the conversion of a TOF spectrum into a mass spectrum
- the use of a simulation program (SIMION) to discuss the mass spectrum calibration and to optimize the time resolution of the spectrometer
- dot

4.1 Signal Synchronization

The experiments of pump-probe described in Chapter 1 require an impressive temporal resolution. A crucial condition to perform experiments with an attosecond time resolution is to be able to synchronize the laser pulse with, at first, the gas valve used to produce high-order harmonics in the HHG process.
The reason why it is used a pulsed valve to produce the gas jet used for the HHG process is that the pressure in the vacuum chamber where the process happens can be kept low enough not to damage the turbo vacuum pump, still guaranteeing a good gas density in the focal spot of the IR laser

pulse. Usually, in the working condition, the pressure in the chamber was kept around 2×10^{-3} mbar.
Since the laser pulses emission from the oscillator is not exactly at 1 kHz and is not predictable, as it is not predictable the phase of this periodic emission, the triggering signals used to drive the components of the line which must be synchronized with the laser pulse have to come from a direct detection. This is done by a photodiode placed as in Figure 4.1. The compressed pulse coming from the Hollow Core Fiber impinges on a dielectric mirror, thus letting a little portion of the beam pass through it. This loss impinges on a photodiode, and the signal detected by the photodiode is sent, as a trigger, to a first delay generator from Stanford. Thanks to this device, it is possible to delay an output trigger signal (whose shape can be chosen) with a precision up to the picosecond time scale. This makes possible to synchronize the emission of the gas jet pulse in the HHG chamber with the laser pulse by just looking at the XUV spectrum, since a good synchronization means a better efficiency for the process. The triggering signal for the HHG generation will have a repetition rate of about 1 kHz, since each incoming laser pulse is used for the high-order harmonic generation.
The first delay generation stage is then connected to a second one, which is used for the synchronization between the laser pulse used to ionize and probe the molecules under investigation and the gas jet driven by the Parker valve, used to bring the molecules into the interaction zone. Since this valve works with a mechanical system, its working frequency cannot be too high and in particular it can't exceed 100 Hz. For this reason, the delay between the triggering signal coming from the first delay stage and the output signal of the second one is set such that only one out of ten electronic pulses is selected. This output signal at 100 Hz is then sent to the driver of the Parker valve as a trigger signal. The duration of this signal, which is chosen to be a differential TTL signal, is settable through the Stanford delay generation stage and sets the duration of the gas jet pulse out of the Parker valve. The analysis of the shape of this gas jet is left to the following section. The choice of the duration of the gas pulse, together with the pressure of the noble gas at the input of the Parker valve, is crucial to find the best compromise between a good density of the molecular gas in the focal point of the laser beam and a low enough pressure in the bioscource and VMI chambers not to damage the turbo vacuum pumps and the microchannel plate. The good working conditions we found are listed in Table 4.1. These parameters helped us not to generate discharges in the conductive channels of the microchannel plate, which can occur when the density of gas in regions with high potential differences, such as the conductive channels, is enough to produce the effect of the dielectric breakdown. Moreover, the turbo vacuum pumps didn't shut

molecular gas pulse duration	$\approx 300\ \mu$s
biosource chamber pressure	$\approx 5 \times 10^{-4}$ mbar
VMI chamber pressure	$\approx 10^{-6}$ mbar

Table 4.1: Working conditions on the biomolecular source

off because of excessive stress of their engines.
This Stanford delay stage is connected to a last one, which has to adjust the delay of the signal who triggers the acquisition board used to collect the TOF data from the VMI detector. The 100 Hz signal coming from the second delay stage is sent to the acquisition board and delayed such that the time window of acquisition matches the arrival time of the photofragments. Moreover, a challenging task is represented by the synchronization of the

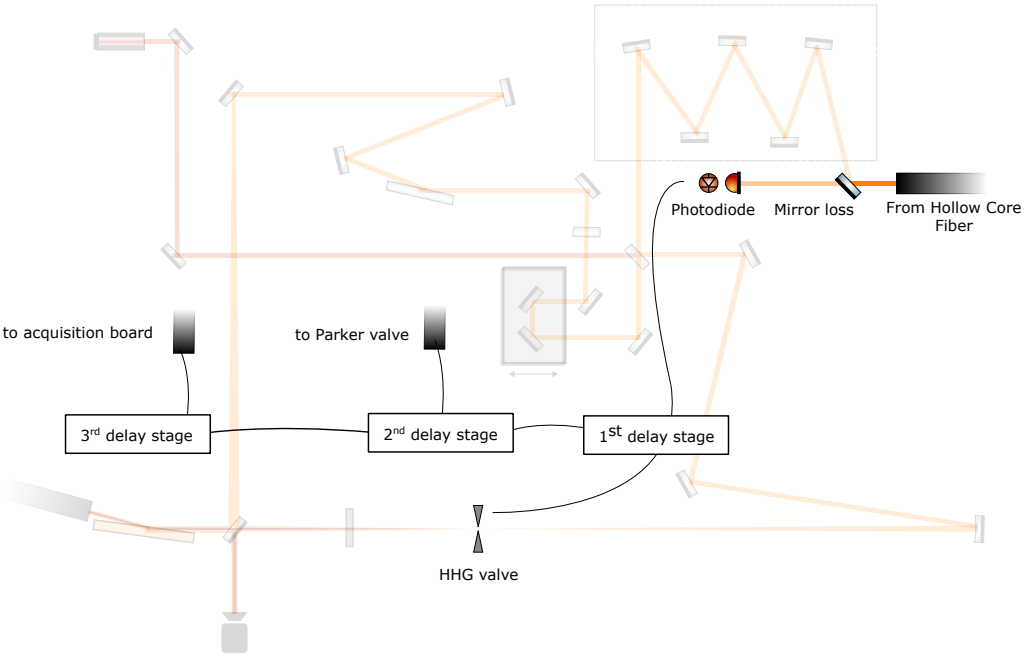

Figure 4.1: Sketch of the connections between different components of the beamline which allow to synchronize them. The signal detected by the photodiode drives all these signals which are delayed by three delay stages, according to what is needed in each beamline stage.

acquisition time window with the correct laser pulse. Since the laser pulses generated in the HHG process have a repetition rate of 1 kHz while the Parker valve can only work at a frequency of 100 Hz, only one out of ten laser shots will probe the higher molecular gas density, as depicted in Figure

4.2. What it has been observed is that the molecular gas density does not go to zero within 1 ms, that is the time occurring between one laser shot and the following one, but after a peak corresponding to the Parker valve opening it reaches a value which does not change significantly before the following gas jet pulse, as shown in Section 4.3. By scanning the delay of the Parker valve opening in rough steps over the full range of 10 ms, the correct laser pulse synchronized with the latter can be identified. Subsequently, the delay can be finely tuned for synchronizing the laser pulse with the maximum gas density in the interaction region by a fine scan over 1 ms.
What has been said so far does not take into account the superposition between the XUV pump pulse and the IR probe one, which will be discussed in Section 4.4.

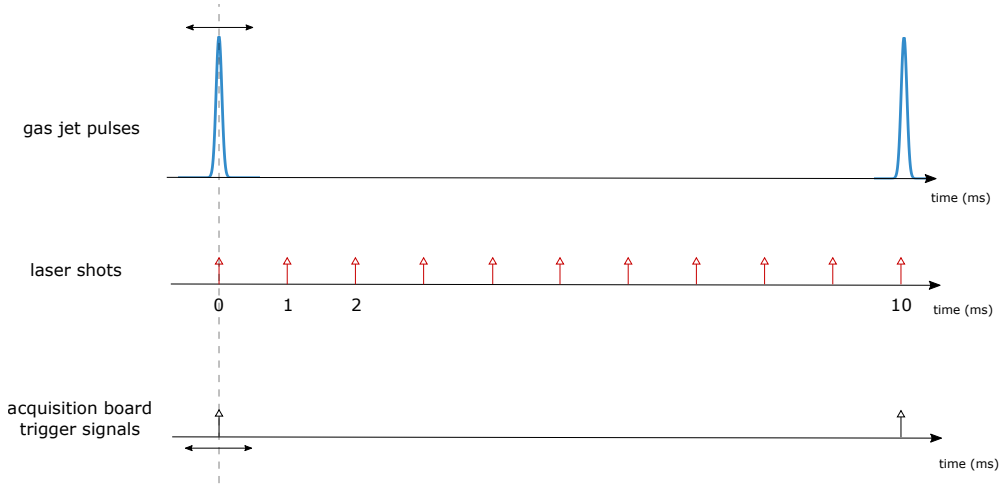

Figure 4.2: Sketch of the synchronization issue between the laser burst, the gas jet pulse which drives the molecular vapour and the trigger which drives the acquisition board. As it is depicted by the arrows, the controllable signals are the driver of the gas jet pulse and the triggering signal of the acquisition board.

4.2 Spectra Acquisition

As described in Chapter 2, the VMI spectrometer works by collecting the photoelectrons or photofragments generated by the interaction of the matter with the laser light. Those charged particles are accelerated by a set of metallic plates and the collection of these particles is entrusted to a microchannel plate (MCP), which is able to multiply the intensity of the signal by using the kinetic energy of the incoming electrons or photofragments to emit an

electron which, thanks to a strong electric field, produces a cascade of electrons that propagates through the channel. As a result, the signal of just one charged particle has been turned into a cloud of electrons.
Since the VMI has been designed to observe and analyze the spatial properties of the photoemission, the intrinsic spatial information incoming from the MCP, which amplifies the signal in micro-channels, is preserved by revealing the signal on a phosphor screen. A potential difference is applied between MCP and the screen such that the kinetic energy of the electrons impinging on the screen produces the image to be analyzed. Besides I will discuss the different approaches that can be used to acquire the temporal information.

(i) Detection with a photomultiplier tube: with a photomultiplier tube places such that it acquires the luminous signal coming from the phosphors screen, subsequently amplifying it. We noticed that this method resulted in a very poor resolution, mainly due to an exponential tail with a long decay time probably caused by the lifetime of phosphors or the electronics of the photomultiplier tube. The resulting TOF peak is the one in blue in Figure 4.3.

(ii) Detection from the potential of the phosphors screen: when a bunch of electrons coming from the MCP hits the phosphors screen it generates a spike on the potential of the phosphors screen. By detecting this spike, it is possible to get the temporal spectrum of the photofragments or photoelectrons generated by the interaction between light and molecules. The detection of this signal was observed to generate narrower peaks, and so with a better temporal resolution. An example is the red peak in Figure 4.3.

As predictable, the most intense peak is the one corresponding to helium (He), as it can be observed in Figure 4.5. Helium is the carrier gas we used, and its density is higher than any other component of the molecular gas jet. By keeping some parameters, like the Parker valve opening time and the helium pressure at the input of the valve, constant, we can expect this density to be constant during time. This could suggest to exploit this element to normalize the spectra taken at different times, being able to observe a dependence of the intensity of each photofragment on the time delay between XUV and IR photons.

4.3 Gas Jet Temporal Shape

Since the VMI spectrometer requires to work in ultra-high vacuum conditions, a trade-off between a high density of the molecular beam and a low

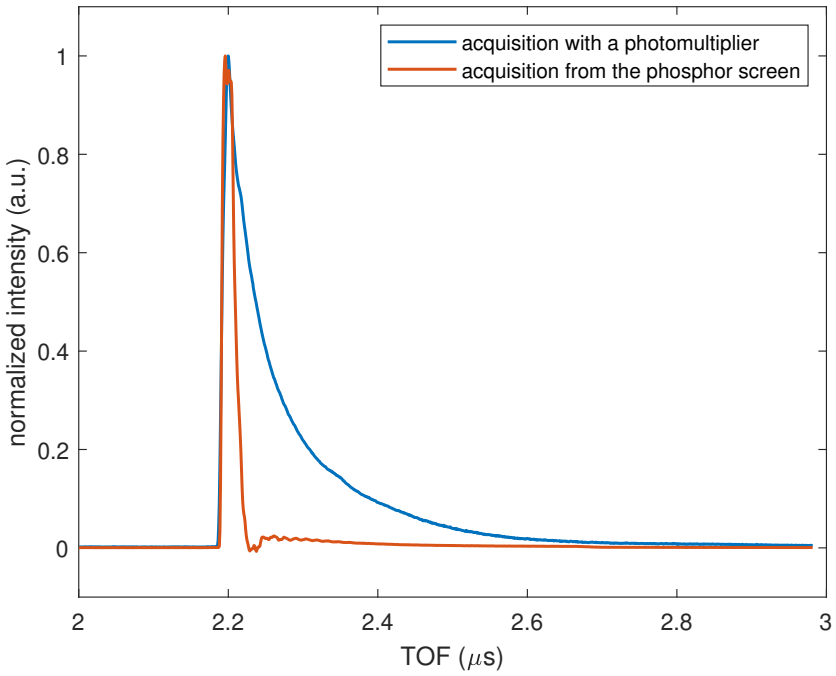

Figure 4.3: Normalized TOF peaks for helium ions. One is taken with a photomultiplier which is placed in front of the phosphors screen, the other is acquired directly from the voltage signal of the phosphor screen. It is observed that the second approach gives a much better signal shape.

pressure of the VMI chamber has to be made. One possibility based on the fact that laser shots come every millisecond is to use a pulsed valve to drive the molecular beam periodically. This pulsed emission is entrusted to a Parker valve, as discussed in Chapter 4.
For characterizing the emission of this valve it is possible to analyze the TOF spectra acquired at different delays between the laser shot and the valve trigger signal. We performed this experiment with the XUV pulse only, since there was no need to probe the excited molecules. Moreover, since the purpose was just to characterize the valve and there was no need to introduce into the VMI chamber a molecule to be tested, the oven was not mounted. During these tests, we used argon.
The XUV laser shot, together with the acquisition of the TOF spectra performed with the VMI, revealed the gas which was in the chamber at the time of the laser burst. Of course we expected the main component to be argon, but it was possible to observe also ions coming from nitrogen, oxygen and water (see Figure 4.5) which are residuals gas coming from the air which fills the chamber every time it is vented. These ions have been exploited, since their density in the chamber is constant for various delays between the laser

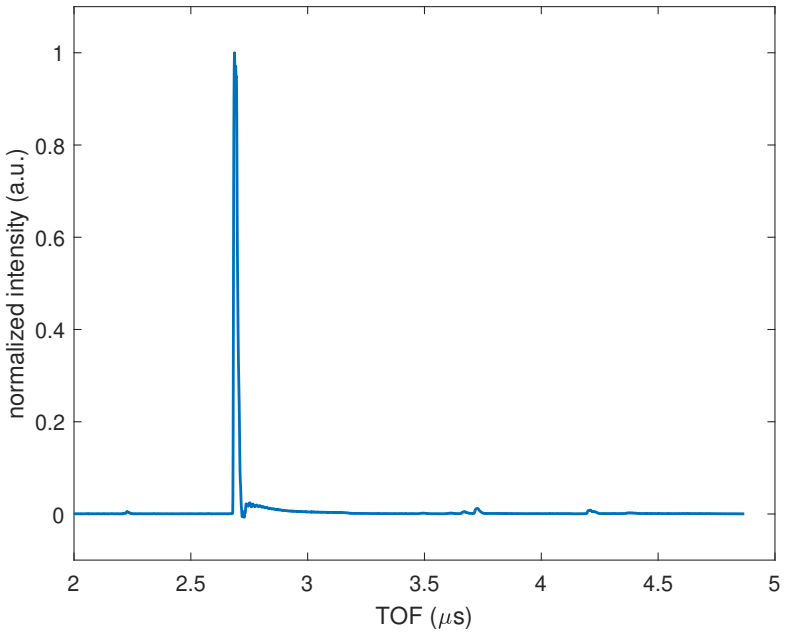

(a) TOF spectrum taken from the phosphor screen

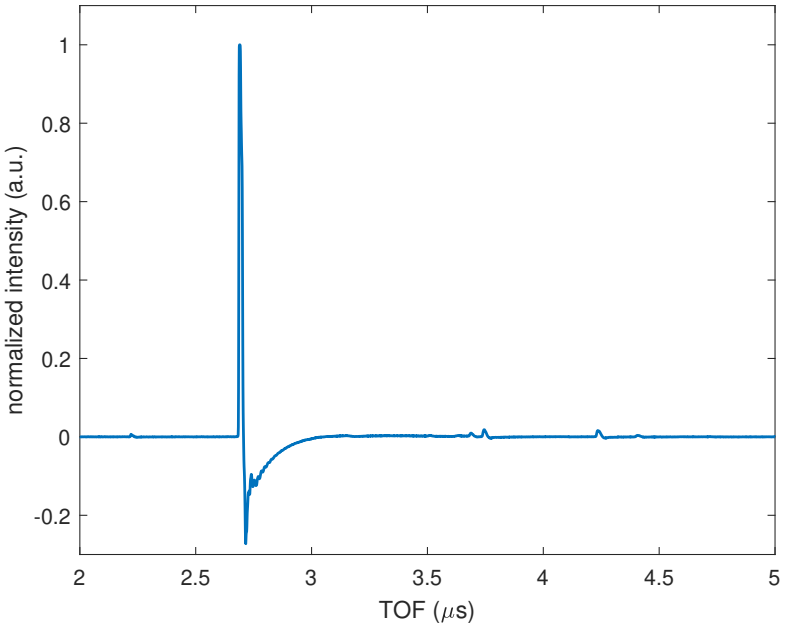

(b) TOF spectrum taken with an amplifier

Figure 4.4: TOF spectra shape comparison between the one taken directly from the loss of the phosphor screen voltage and the one amplified with the help of an amplifier. This introduces a negative overshoot which has to be fixed with a processing of the data.

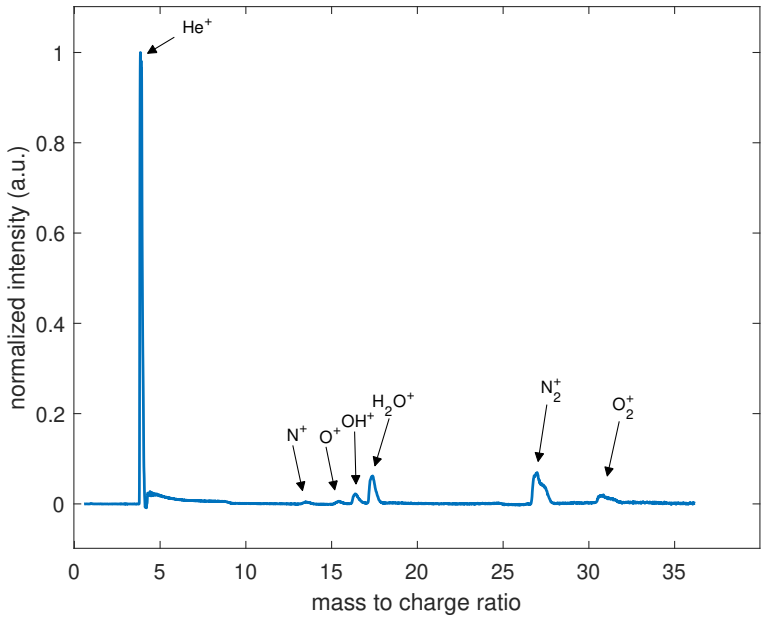

(a) Mass spectrum taken from the phosphor screen. Each peak is labelled with the name of the corresponding ion

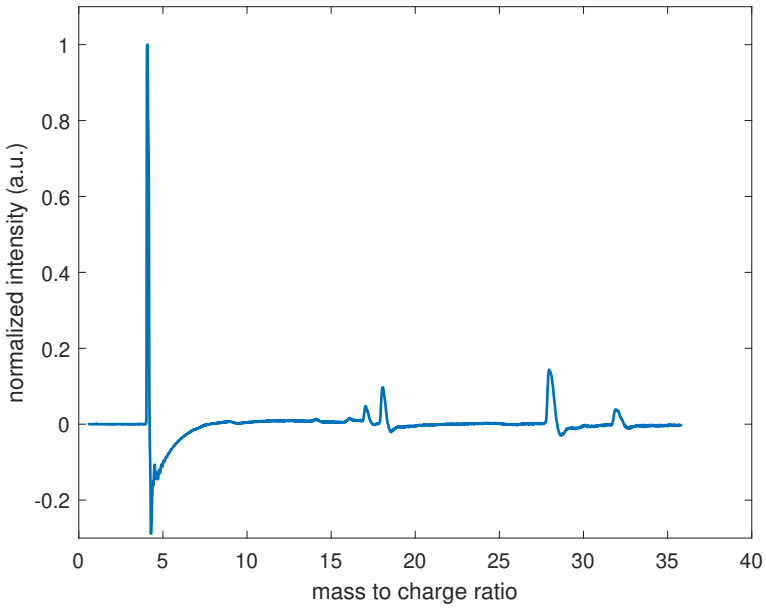

(b) Mass spectrum taken with an amplifier

Figure 4.5: Mass spectra shape comparison between the one taken directly from the loss of the phosphor screen voltage and the one amplified with the help of an amplifier. It is possible to observe the same overshoot as in the TOF spectra.

shot and the valve opening time, while the Argon one is not. In order to do that, the integral of the peak in the TOF spectrum has been computed to estimate the density of a particular component of the gas in the interaction chamber.
In the working conditions, as described in Section 4.1, the valve works at a frequency of 100 Hz, emitting one gas jet every ten laser shots. Moreover we usually worked with 300 μs opening times. However, since in this way the time between two gas jets is too short, the contrast between the signal coming from the jet and the background is not good enough to get a good reconstruction of the temporal profile of the jet. For this reason, we made this analysis by emitting one jet every 30 ms.
The result of this analysis is shown in Figure 4.6. The yellow dashed line corresponds to the baseline, chosen as the mean of the first two points of the profile between the rising edge. It is possible to observe that this profile is asymmetric, since the tail at the end of the pulse is at a value larger than the baseline. This is because the argon ejected by the valve needs a time longer than the hundreds on μs shown in the graph time to be completely pumped out of the chamber. Moreover, the red line shows how the nitrogen density is not affected by the gas jet. This means that the density of these components in the vacuum chamber have reached a stationary value which is, by the way, at least one order of magnitude lower than the argon one.
A further analysis of this shape can be done with a fit of the gas density as a function of time. I used *Matlab* to fit it with a gaussian function with three free parameters a, b and c:

$$\text{gas density} = ae^{(\frac{\text{time}-b}{c})^2} \tag{4.1}$$

and computed the FWHM of the resulting fit function as:

$$\text{FWHM} = 2c\sqrt{\log 2} \tag{4.2}$$

For a pulse length set at 300 μs, a full width at half maximum (FWHM) of approximately 175 μs is found. The result is shown in Figure 4.7. This, together with the regular shape of the pulse, suggests that the Parker valve works as expected.

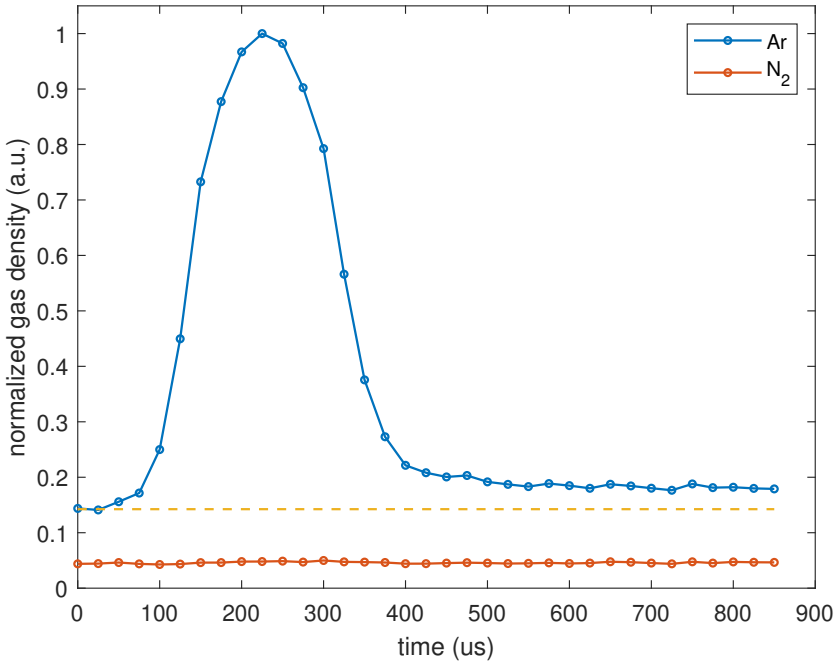

Figure 4.6: Normalized gas density obtained as the integral of the peaks of helium and nitrogen ions. The dashed line represents the baseline signal taken before the rising edge of the signal. The constant nitrogen signal highlights the fact that the residual atmospheric gas inside the VMI chamber is constant and does not change when the helium gas jet is introduced into the chamber.

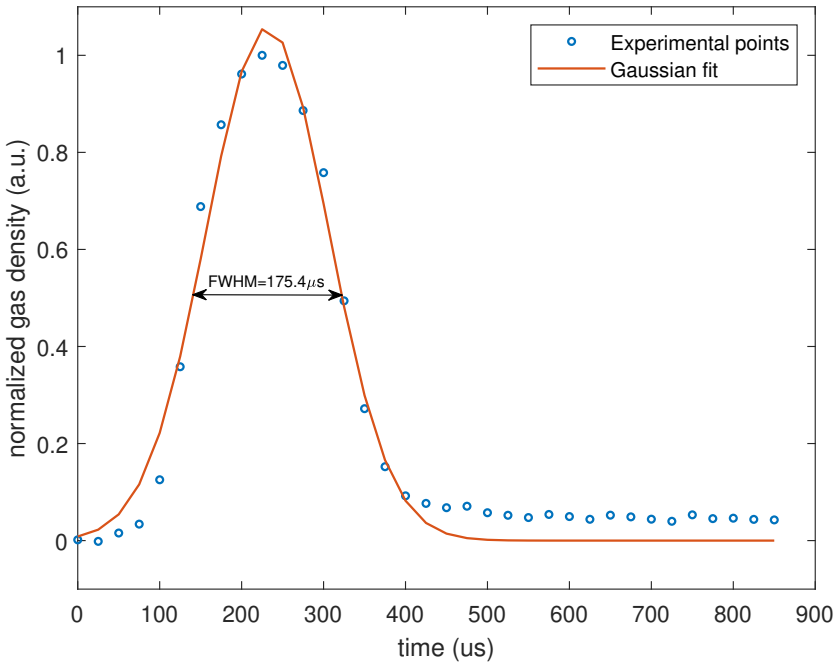

Figure 4.7: Gaussian fit of the jet shape of helium obtained as the integral of the TOF peak of helium, as computed with a *Matlab* fit with three free parameters. It shows a shape in a good agreement with the experimental points and whose FWHM is around one half the set jet temporal duration.

4.4 Pump-Probe Temporal Superposition

Attochemistry purpose is to investigate intramolecular dynamics occurring on a time scale which goes below one femtosecond. The pump-probe approach developed in the experiments performed with this setup relies on the excitation of the molecule with an XUV pulse into a superposition of cationic states, followed by an IR one. The variable delay between the two pulses could make it possible to probe the electronic charge movement in the molecule, since different photofragments will be generated upon interaction with the probe pulse depending on how the electronic density has redistributed itself. For this reason, it is of crucial importance to find the temporal overlap between the two pulses. By doing this, it will be possible to set different delays between the pulses, thus probing with the IR pulse different electronic charge configurations. Different techniques can be adopted in order to achieve this result.
One possibility is given by an experiment firstly shown by Herrmann et al. [8]. This method exploits the ionization of helium performed by a multi-photon process induced by an XUV photon followed by one or more IR photons. If the XUV radiation is mainly composed of harmonics whose energy is below the ionization potential of helium, which is around 24.59 eV, ionization from states below the IP will only occur by absorption of at least one more photon from the IR probe pulse. The intensity of the helium signal detected from the TOF spectrum will therefore strongly depend on the delay between the pump and probe signal. More specifically, it should rapidly increase around the zero-delay, showing then oscillations given by the quantum interference between the two paths which can lead to helium ionization, that are the direct ionization by the harmonics with energy above the ionization threshold and the multiphoton ionization given by XUV and IR photons.
As shown in Figure 4.8, the maximum of the yield corresponds to the zero delay between the XUV and IR pulses. Around the zero it is possible to observe strong oscillations at 2ω (twice the pulsation of the IR field) while, for large negative delays, the yield becomes flatter but larger than the one observed at large positive delays, when the APT comes after the IR pulse. In order to achieve this result the intensity of the generating field of XUV radiation was adjusted such that the spectrum was dominated by harmonics 13 and 15 which, as shown in Table 2.1, have an energy below the ionization potential of helium.
An analysis in the spectral domain, followed by a gaussian fit, was used to determined the zero-delay position (black curves). In red, it is shown the total absorption probability of the XUV radiation integrated in energy from 19 to 35 eV whose frequency domain analysis followed by a gaussian fit leads to a

different zero-delay result. However, the agreement between the two results was very good, with a shift of less than one femtosecond.
In order to test this experiment in our laboratory, we firstly tried to observe the same behaviour with the whole XUV spectrum which is usually produced by our setup, where the most intense harmonics are the 15^{th} to 19^{th}. However, the amount of radiation with an energy higher than the ionization potential was so high that it was not possible to observe any significative change in the yield by varying the delay between the APT and the IR pulse.
Then we tried to remove as much as possible the higher order harmonics by using a Sn filter which was already mounted on the motorized rotating device where there is also the Al filter (see Figure 2.9). It was then easy to introduce this filter in the beamline and we obtained a spectrum centered at lower energies. The observed He yield is shown in Figure 4.9, where it is possible to notice that there are no 2ω oscillations, even if there is a rapid downhill front as expected. The lack of oscillations does not make possible to find a precise measurement of the T_0, which is the only result we wanted to obtain from this experiment. Moreover, the Sn filter which was already mounted next to the beamline was not mounted on a hollow disc of glass as the Al filter is: this made impossible toactively stabilize the delay as depicted in Section 2.5, since the IR residual radiation coming from the HHG stage cannot reach the drilled mirror and the interferometric measurement of the delay can't be performed.
The difficulties encountered by following the first approach led us to consider another possible way out, which is provided by a well-known technique used to characterize an attosecond pulse, called Reconstruction of Attosecond Beating By Interference of Two-photon Transition (RABBITT). As described in Appendix B, this technique relies on the quantum interference between different paths which can lead to the population of the sidebands. For this reason, it can be exploited to find the temporal overlap between the two pulses. Moreover, the setup needed to perform a RABBITT test is the same used to perform the pump-probe experiments. For the detection of electrons, the polarity of the extraction field in the VMI spectrometer must simply be inverted. This makes this approach feasible.

4.5 Analysis of the Mass Spectra

As shown in Section 4.2, the acquired data need to be processed in order to be able to extract meaningful information from them. The calibration consists of the following steps: (i) removal of the baseline; (ii) normalization with respect to a signal corresponding to a component which we assume to

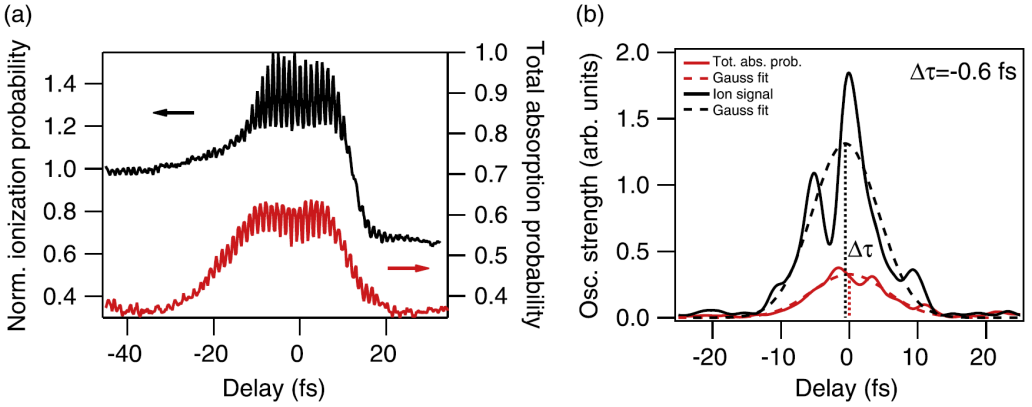

Figure 4.8: On the left side graph in black, normalized measured ionization probability as a function of the delay between XUV and IR pulses. On the right side one, the analysis of the signal in frequency domain. In red the total absorption probability as integrated with energies from 19 to 35 eV. The comparison between the maxima of the frequency domain signal gives the comparison between the measured and theoretical zero delay. Adapted from [8]

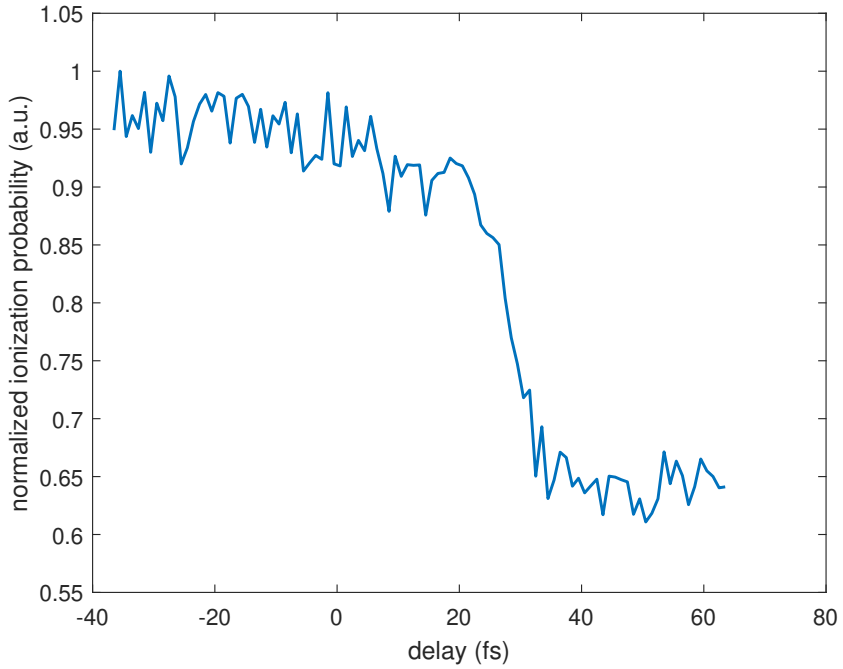

Figure 4.9: Measured ionization probability for helium as a function of the delay between the XUV and IR pulse. The delay is defined as the difference between the XUV and IR burst instant of time.

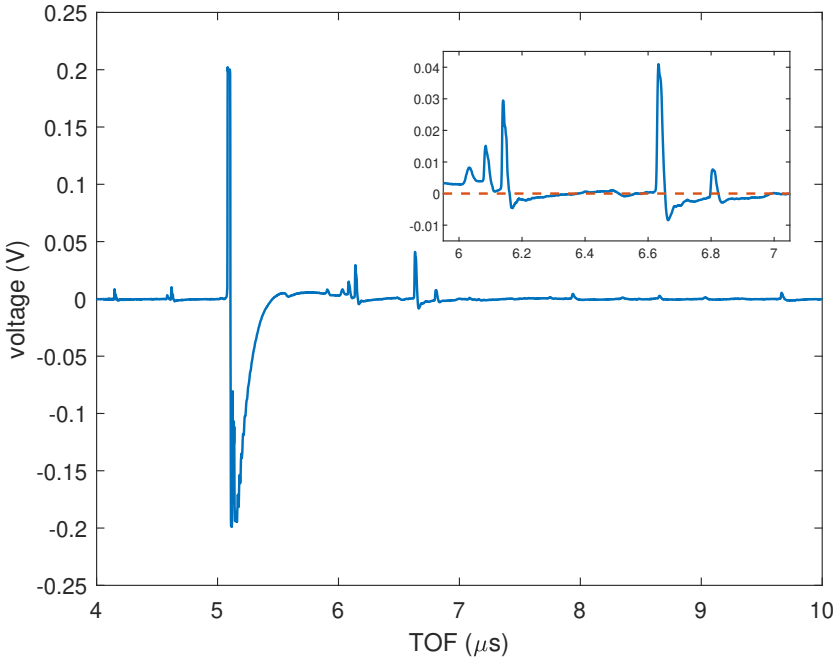

Figure 4.10: Time of flight spectrum as acquired from the phosphor screen and amplified with an amplifier. The acquisition introduces a strong negative overshoot, which has to be removed with a processing of the signal. In the box a zoom of the TOF spectrum around the peaks corresponding to the O^+, OH^+, H_2O^+, N_2^+ and O_2^+ ions.

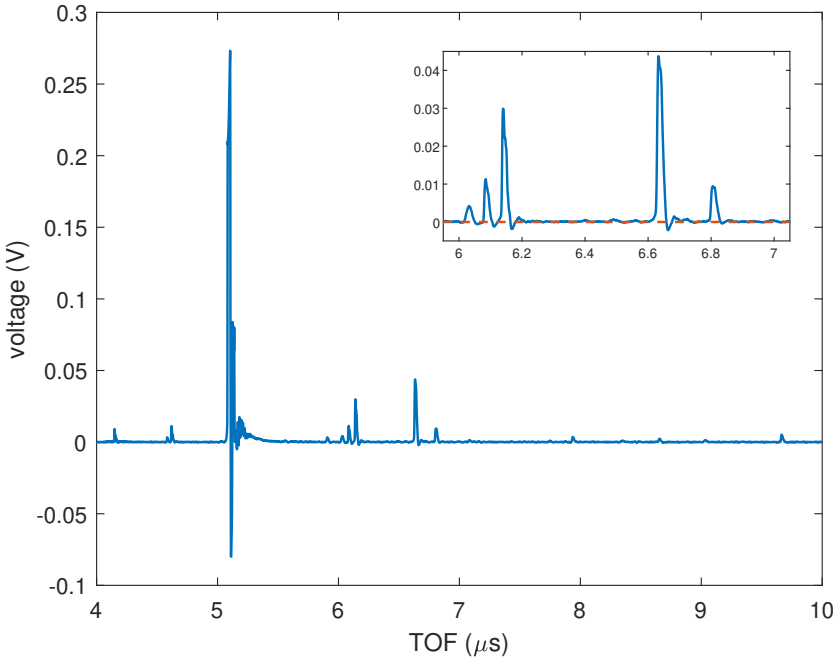

Figure 4.11: Time of flight spectrum acquired with an amplifier after the processing. The zoomed plot in both graphs highlights the peaks corresponding to O, OH, H_2O, N_2 and O_2 ions and it is possible to observe a much regular shape with respect to Figure 4.10 due to the baseline removal.

be constant in time; (iii) calibration of the mass to charge ratio axis.
In Figure 4.10 it is possible to see an example of a TOF spectrum acquired from the phosphor screen and amplified. The meaningful signal corresponds to the positive half of the voltage axis, while the negative part of the signal is due to the electronics of the acquisition. Moreover, in this specific case the signal coming from the helium peak, the most intense one, exceeds the limits of the acquisition board, which were set at 200 mV. This is the reason why, apparently, the meaningful signal and the negative overshoot have the same amplitude. As it is possible to observe from the other peaks, this is not true. The boxes showing a zoom of the spectrum highlight the peaks corresponding to the O^+, OH^+, H_2O^+, N_2^+ and O_2^+ ions. Figure 4.10 and Figure 4.11 show their shape before and after the baseline removal. By processing the signal in a similar way we expect to get the same result also for the signal coming from interesting ions thus being able to search for correlations between the photofragments signal and the delay between the pump and probe signals.
In Chapter 2 it has been shown which is the relation between the time of flight and the mass to charge ratio:

$$TOF \propto \sqrt{\frac{m}{q}} \tag{4.3}$$

In order to obtain a mass spectrum from a time of flight one, it is necessary to calibrate the mass axis by exploiting the knowledge of this relation. Since there are two free parameters:

$$TOF = a\sqrt{\frac{m}{q}} + b \tag{4.4}$$

where b accounts for the offset between the zero of the time of flight axis and the instant when the laser ionizes the target gas, it is possible to perform a two-points calibration. By knowing the mass corresponding to two peaks in the TOF spectrum:

$$\begin{cases} t_1 = a\sqrt{m_1} + b \\ t_2 = a\sqrt{m_2} + b \end{cases} \tag{4.5}$$

it is easy to obtain the a and b coefficients as

$$a = \frac{t_1 - t_2}{\sqrt{m_1} - \sqrt{m_2}} \tag{4.6}$$

$$b = -\frac{t_1 - t_2\sqrt{\frac{m_1}{m_2}}}{\sqrt{\frac{m_1}{m_2}} - 1} \tag{4.7}$$

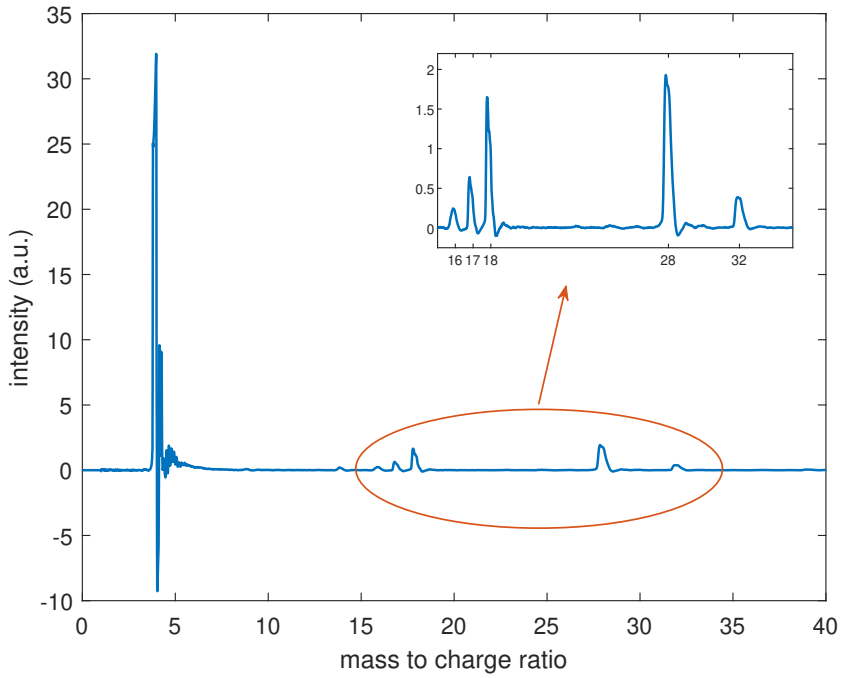

Figure 4.12: Mass to charge ratio spectrum obtained through a TOF spectrum, after the conversion. The higlighted peaks, circled in red and zoomed, correspond to the masses of ions in Table 4.2. Although the calibration has been done with just two peaks, the other ones correspond to the correct mass to charge ratios.

Following this procedure, the mass spectrum in Figure 4.12 has been obtained. The highlighted peaks correspond to singly charged ions listed in Table 4.2.
Although the calibration of the m/q axis has been done with just two points from the TOF spectrum, the other peaks correspond to the correct values of mass to charge ratio.

4.6 Mass Spectrum Calibration

The relationship between time of flight and mass to charge ratio as described in Section 4.5 contains a coefficient of proportionality between TOF and $\sqrt{m}$. Combining this result with the description of the VMI time of flight in Chapter 2, it is possible to see that this coefficient depends both on the length of the tube and on the voltage difference applied to accelerate the electrons or photofragments. Among these parameters, only the voltage applied to extractor plate, repeller plate and MCP are controllable since the length of the fly of the particles depends on the interaction position between the

Ion	Mass to Charge Ratio
O^+	16
OH^+	17
H_2O^+	18
N_2^+	28
O_2^+	32

Table 4.2: Values of the mass to charge ratio corresponding to the highlighted peaks in Figure 4.12

repeller and extractor plate. This position can slightly change in time, due to small movements of the VMI chamber with respect to the laser beam and viceversa. For this reason it is interesting to exploit a simulation software, *Simion*, to simulate the flight of a group of particles inside the VMI. We compared the a coefficient obtained with the experimental data on a certain day with the one obtained with a two-points calibration of the simulated times of flight. The voltages applied to the VMI during the experiment were set also on *Simion*, and different interaction positions have been tested in order to find the position where the simulated coefficient coincide with the experimental one.
By moving the group of particles in the x-axis of Figure 4.13, where the VMI repeller-extractor-ground structure is sketched, we saw that the coefficient of proportionality between time of flight and mass to charge ratio changed. As an example, three different interaction points are shown: one in a central position between the repeller and extractor plate, one at 4.3 mm to the right of this point and another 8.1 mm far from the central point. On *Simion* a group of particles, uniformely distributed in a sphere of radius 250 μm centred in those points, with 3000 particles with a mass to charge ratio of 4 and 3000 with $m/q = 28$ was flown and its time of flight was recorded. The two-points calibration is performed by using the average TOF of both groups of particles and the result has been compared with the experimental one.
The results are shown in Figure 4.14, where the colours of the simulated curve match the colours of the points shown in Figure 4.13. The best match between the experimental and simulated data is obtained in a position which is not centered, but around 4.3 mm on the right with respect to it. This result is valid for one specific experiment in one specific day, but this procedure could be adopted to check the interaction position every time it is needed. Moreover it gives us a very good indication of the nearly perfect alignment of spectrometer and laser.

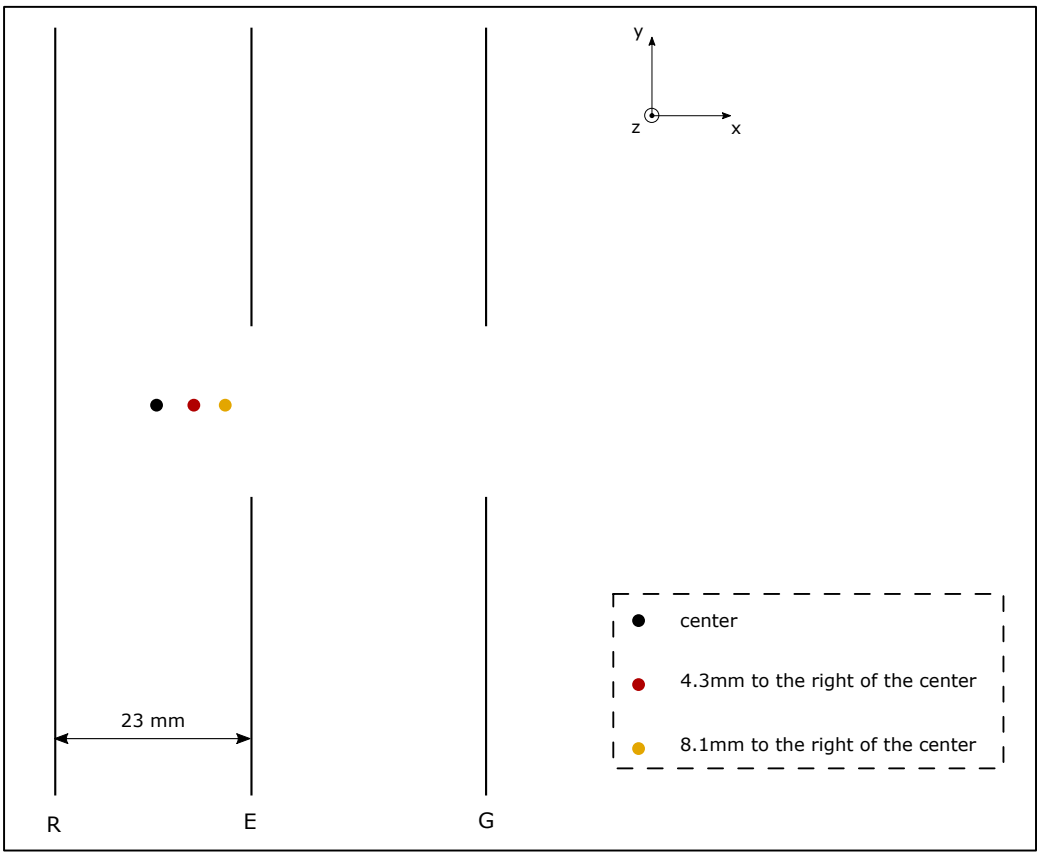

Figure 4.13: Sketch of the interaction region of the VMI. The three dots correspond to three different interaction positions from where the particles have been flown during the simulations. The red dot corresponds to the point which was found as the actual interaction positions for a set of data taken during an experiment of a certain day in our laboratory.

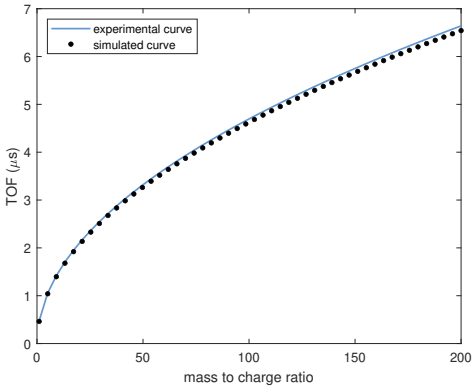

(a) Plot of the TOF-m/q relationship with the data simulated starting from the position corresponding to the black dot. The agreement is not good.

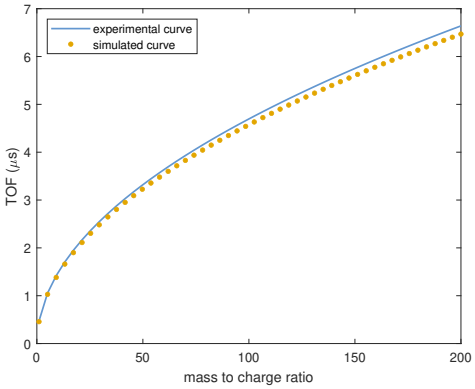

(b) Plot of the TOF-m/q relationship with the data simulated starting from the position corresponding to the yellow dot. Also here, the agreement is not good.

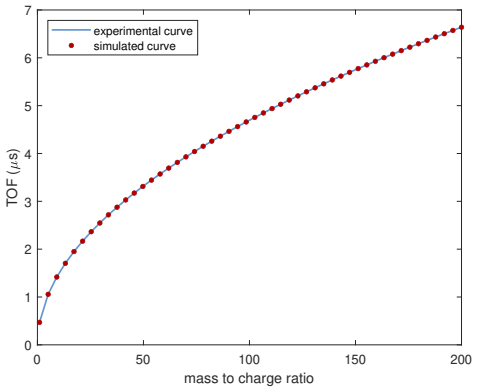

(c) Plot of the TOF-m/q relationship with the data simulated starting from the position corresponding to the black dot. This was found as the position with the best agreement with the experimental data.

Figure 4.14: The continuous line corresponds to the experimental relationship between time of flight and mass to charge ratio. The dotted ones to the simulated relationships. The colours of the dots correspond to the interaction positions depicted in Figure 4.13.

4.7 Mass Spectrum Resolution

Another interesting parameter which can be useful to be analyzed with the help of *Simion* in order to find the best working parameters is the time (or mass) resolution of the TOF spectra. In order to be able to distinguish two close peaks in the TOF, it is important to get a sufficient resolution, defined as

$$\text{time resolving power} = \frac{\text{TOF}}{\Delta\text{TOF}} \tag{4.8}$$

where ΔTOF is the width of the distribution of the times of flight of all the particles with a specific mass to charge ratio.
This parameter varies with the voltages set to the extractor and repeller plates, and for this reason it is important to find a good ratio between those two quantities which can provide a good resolving power. In order to investigate this problem, we simulated the flight of a group of particles placed in the position which was found with the analysis described in Section 4.6. These particles were uniformely distributed in a sphere of radius 250 μm. We chose to fly nine different group of particles, with 3000 particles per group, with nine different mass to charge ratios.
In our analysis we fixed the value of the voltage applied to the repeller (V_{rep} to the one used in the experiment performed the same day as the one in the previous section, which was 4.2 kV. We changed the value of V_{extr} starting from the value used in the experiment, which was $V_{extr} = 2.6$ kV and we changed it to find a maximum value of resolving power. In order to define resolving power, we chose to fit the distribution of times of flight of a certain group of particles with a gaussian distribution and we defined ΔTOF as:

$$\Delta\text{TOF} = 4\sigma_{\text{fit}} \tag{4.9}$$

where 4σ has been chosen to consider the whole peak of a certain mass, almost until it goes to zero.
Before analyzing how the resolving power changes with the ratio between V_{rep} and V_{extr}, we searched for the best V_{extr}. In order to do that, we used

$$\text{resolution} = \frac{\text{TOF}_{max} - \text{TOF}_{min}}{\text{TOF}_{average}} \tag{4.10}$$

as a parameter to define how good the resolution was for a particular value V_{extr}. This in order to perform a quicker but meaningful analysis. What we found was that there is a value which minimizes the value of the resolution, improving this value of orders of magnitude with respect to the working condition we adopted in the experiment. In the already described conditions, the

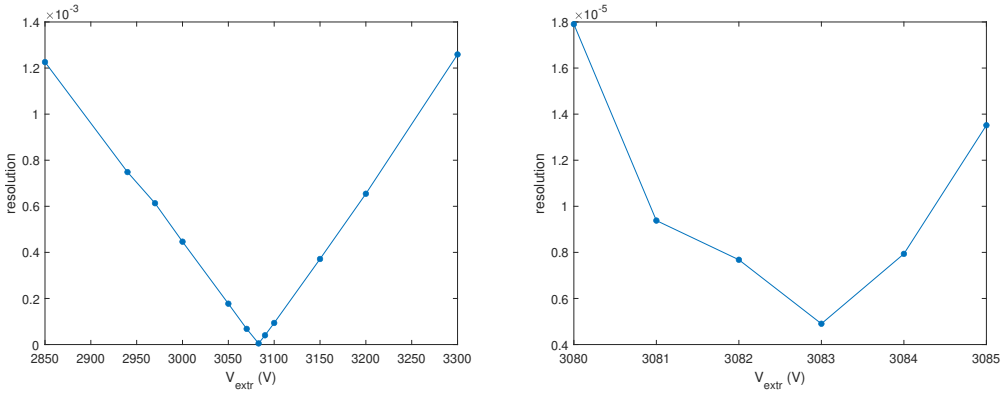

(a) Resolution as a function of V_{extr}

(b) Zoomed view of the resolution as a function of V_{extr} around the minimum

Figure 4.15: Plot of the simulated resolution as a function of the extractor plate voltage, for a group of particles with a mass to charge ratio corresponding to 150. The interaction position was chosen to be the one obtained in the last section.

simulated optimum value of V_{extr} was found at 3.083 kV, as shown in Figure 4.15.

Once the value of the optimum extractor voltage was known, we analyzed the distribution of simulated times of flight in two cases: $V_{extr} = 2.6$ kV and $V_{extr} = 3.083$ kV. As depicted in Figure 4.16, the width of the distribution of times of flight can be reduced by about three orders of magnitude. This reflects on a similar improvement in resolving power.

Actually, by plotting the average times of flight of the different groups of particles against the corresponding width of the distribution of TOFs (Figure 4.17), it is possible to observe that the resolving power does not depend on the mass to charge ratio of the flown particle, which translates into a straight line in the graph. The slope of this line, representing the resolving power, is actually improved by one order of magnitude by optimizing the extractor voltage.

Since the VMI extracting field parameters are not the only ones which contribute to the time resolution of the instrument, we don't expect to be able to achieve such an improvement, since the other instrumental responses are limiting the resolution, too, and probably to a bigger extent. Nonetheless, these simulations could help to improve further the conditions in order to get clean mass spectra and to be able to analyze them in the best possible conditions.

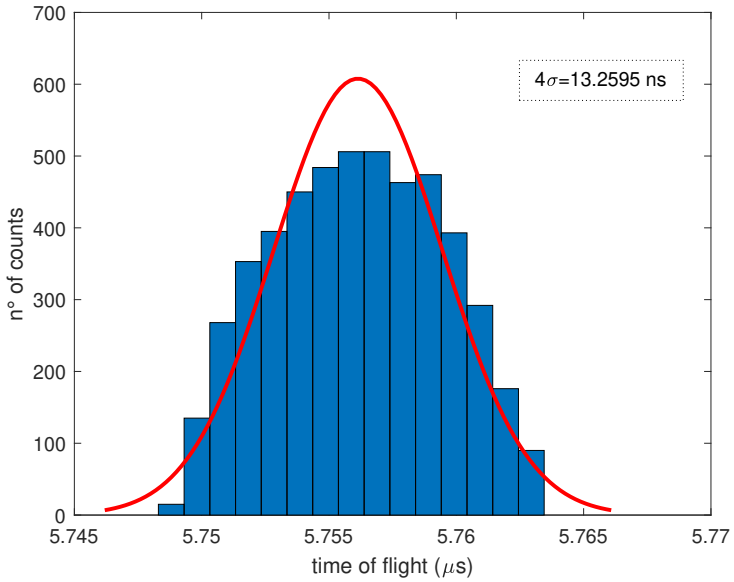

(a) Distribution of the times of flight with a non-optimized extractor voltage (2.6 kV)

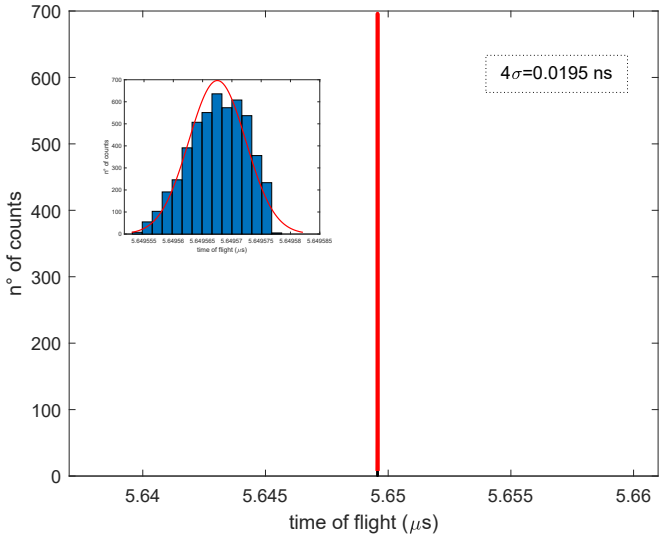

(b) Distribution of the times of flight with the optimized extractor voltage, 3.083 kV.

Figure 4.16: Histogram of the distribution of the times of flight for a group of particles with a mass to charge ratio of 150, for two different values of V_{extr}. In red, the gaussian fit used to compute the width of this distribution. It is possible to notice an improvement of three orders of magnitude of σ.

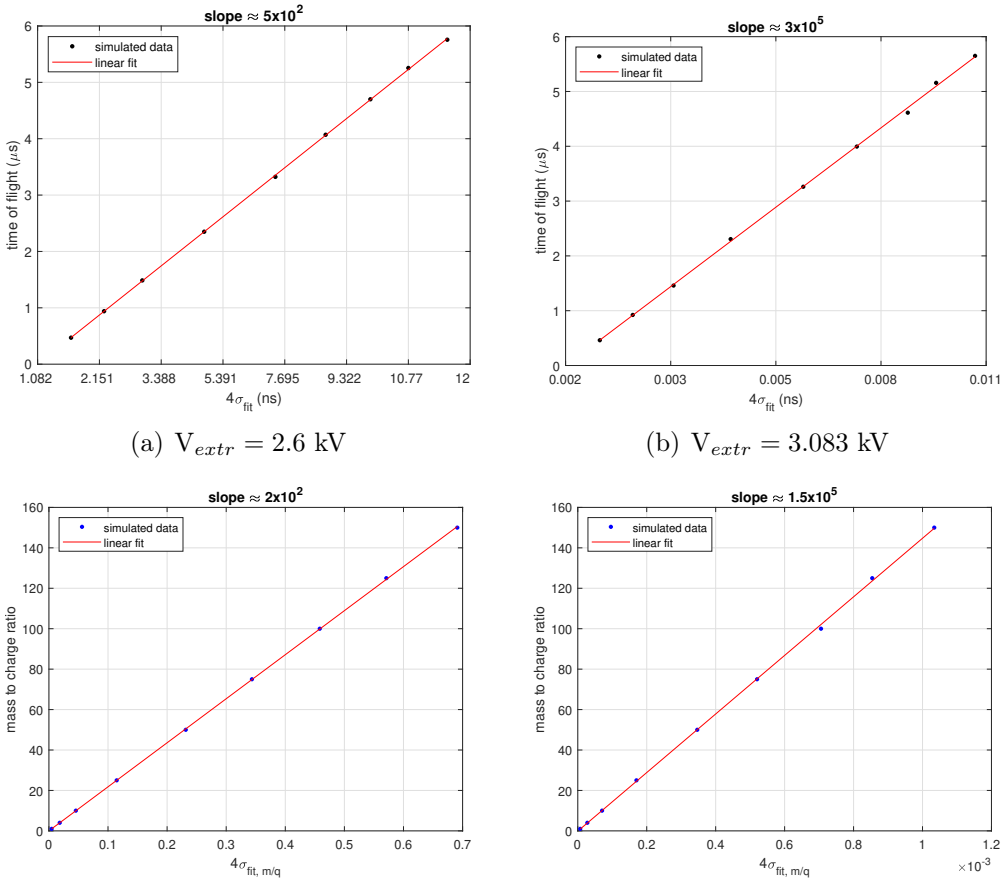

(a) $V_{extr} = 2.6$ kV (b) $V_{extr} = 3.083$ kV

(c) $V_{extr} = 2.6$ kV (d) $V_{extr} = 3.083$ kV

Figure 4.17: Plots of the relationship between average TOF and width of the TOF distribution and between m/q and width of m/q distribution. These relationships are well fitted by a straight line suggesting that the resolving power does not change with the mass to charge ratio.

4.8 Test with Adenine

Finally, in order to prove the correct functioning of the source and, in particular, of the oven, we measured mass spectra of adenine (see Figure 4.18). We increased the temperature until we found a good signal for the characteristic ions and photofragments. This temperature was about 240° C. As reported in Chapter 4, this sample temperature is still compatible with the correct functioning of the valve.

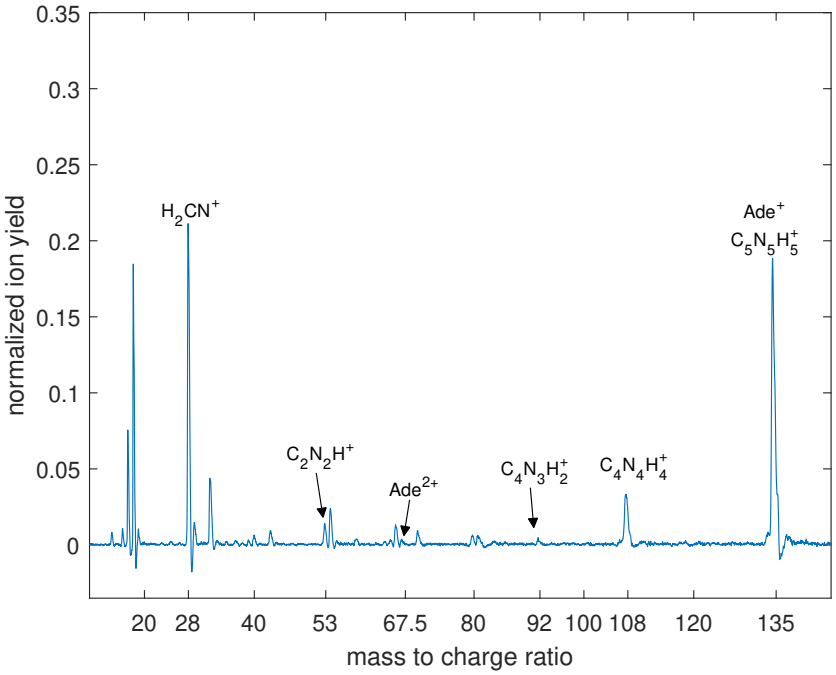

Figure 4.18: Mass spectra of adenine, acquired with a temperature of the sample around 240° C. It is possible to see the singly charged ion peak, the double charged ion peak (although much smaller) and some photofragments resulting from the interaction with the XUV and NIR pulses.

Conclusions and Future Perspectives

During my thesis work we have implemented and characterized a new source for generating gas-phase molecules and optimized the attosecond XUV-NIR beamline within which this source works. Here I present a summary of the work and the main conclusions.

1. **Development of a feedback system for the stabilization of the pump-probe delay**
   This system is based on an active control of the interference fringes produced by a He-Ne laser following the same optical path as the main beam. I implemented a software using LabView which, by acquiring those fringes and retrieving their phase, compensates for the phase shifts acting on a piezoelectric delay stage which is able to modify the path lengths difference. Unlike the previous setup, no additional optics were inserted in the He-Ne path, thus providing a true estimate of the stability of the delay. On a daily basis operation, we get a residual noise of about 30 as.

2. **Implementation of a new molecular source**
   The main drawbacks of molecular beam sources based on heating are the non-volatile character of many bio-relevant molecules and their propensity to decompose when heated up. In order to overcome these problems, we have implemented a source based on a graphite powder matrix. To heat the graphite pellet up we used a Thermocoax metallic resistive coil; its power is adjustable in order to reach a set temperature. The oven was coupled with a pulsed gas jet valve by Parker to drive the molecular beam into the spectrometer. We first built a synchronization line to temporally overlap the laser shot, the molecular beam and the spectra acquisition. Then, the temporal emission of the gas jet was characterized by using the signal from a noble gas (helium). We concluded that the optimized value for the aperture of the valve

was about 300 μs, guaranteeing a good density of molecules and a low pressure in the vacuum chamber. Finally, different acquisition methods have been tested, concluding that a good resolution and signal intensity is provided by the acquisition from the phosphor screen of the VMI and with a subsquent amplification.

3. **Calibration of the zero delay**
   In order to find the temporal overlap between the pump and probe pulses we tested a method based on the helium ion yield [8]. The results showed that this method is not feasible with our experimental setup, since the introduction of a Sn filter into the beam path resulted in the loss of the pump-probe delay stabilization. In a second approach, we used the RABBITT technique, exploiting the opportunity provided by the VMI. In conclusion, we demonstrated that this is the best way to precisely identify this overlap.

4. **Proof of concept**
   A first test was made with the spectra of the noble gas and residual gas in the VMI chamber. The comparison between the experimental data and the simulations performed with the *Simion* software helped us to identify both the interaction position inside the spectrometer and the optimized parameters for the voltages of the VMI electrostatic plates. We found an optimum ratio between the voltages of extractor and repeller plates of about 0.73, which is dependent on the actual interaction position inside the spectrometer. This paves the way for an analysis which can be periodically performed to get the best resolution in the spectra. Moreover, we tested the new oven by acquiring photofragments spectra of adenine. The temperature of the source was set to 240° C. We checked that lower values were not sufficient to generate a dense enough molecular beam, while higher values could disturb the correct functioning of the pulsed valve. The characteristic adenine photofragments observed in the spectra proved that the molecular beam source works as expected.

The successful implementation and optimization of this setup has opened the possibility to perform ultrafast pump-probe experiments in gas-phase molecules. Preliminary measurements on p-nitroaniline have started, with the purpose of investigating, in collaboration with the group of Prof. Fernando Martín Garcia from Universidad Autónoma de Madrid, charge migration in this molecule and related species.

Appendixes: Characterization Techniques for Ultrashort Pulses

Appendix A

FROG

Frequency-Resolved Optical Gating (FROG) is a method to characterize an ultrashort laser pulse [31]. For such a pulse, with a duration below nanoseconds, standard photodetectors are not suitable, since their response is too slow. Bandwidth of electronic devices is limited to a few hundreds of GHz, that means that they can't go below the picoseconds scale. This is why new methods have been implemented, and FROG is one of them.
Considering a linearly-polarized light pulse, and only the electric field of this pulse, we can write it as a scalar: its temporal expression is

$$E(t) = A(t)e^{i\omega_0 t} \tag{A.1}$$

that is a product between the complex amplitude $A(t)$ and the carrier wave with a central angular frequency ω_0. On the other hand, in the frequency domain, it is:

$$\tilde{E}(\omega) = \tilde{A}(\omega - \omega_0) = |\tilde{A}(\omega - \omega_0)|e^{-i\varphi(\omega-\omega_0)} \tag{A.2}$$

where $|\tilde{A}(\omega - \omega_0)|$ is the spectral intensity and $\varphi(\omega - \omega_0)$ is the spectral phase, both centered around the central angular frequency. One could choose whether to measure the pulse profile in the time or in the frequency domain, because they are connected just through a Fourier transform. Since there are no electronic devices capable to measure it in time domain, one possibility is to use a dispersive element (for example a grating or a prism) in order to spatially separate the different frequencies and then measure the intensity associated to each of the frequencies with a multichannel detector. By the way, this would only give us the information about the spectrum intensity:

$$\tilde{I}(\omega) = |\tilde{A}(\omega - \omega_0)|^2 \tag{A.3}$$

from which we can only retrieve the spectral amplitude. This is not enough to retrieve the shape of the pulse. This would need the information about the

spectral phase, which is essential to know the arrival time of each frequency, i.e. the *group delay*:

$$\tau_g(\omega) = \frac{d\varphi}{d\omega} \tag{A.4}$$

So, in order to retrieve the information about the time arrival of each frequency, we need to apply a gate g to the signal, such that the gated signal is:

$$A_{gated}(t,\tau) = A(t)g(t-\tau) \tag{A.5}$$

The Fourier transform of this signal is:

$$\tilde{A}_{gated}(\omega,\tau) = \int_{-\infty}^{+\infty} A(t)g(t-\tau)e^{-i\omega t}dt \tag{A.6}$$

which is called *Wavelet Transform*. Sliding the gate, it is possible to get the information about when the different frequencies will arise.
Anyway, a detector is only able to measure the intensity $S(\omega,\tau)$ of this signal, called *spectrogram*, that is:

$$S(\omega,\tau) = \left|\int_{-\infty}^{+\infty} E(t)g(t-\tau)e^{-i\omega t}dt\right|^2 = |\tilde{E}_{signal}(\omega,\tau)|^2 \tag{A.7}$$

where we have defined $E_{signal} = E(t)g(t-\tau)$. So, by measuring the spectrogram and assuming the gate function $g(t-\tau)$ to be known, it is possible to reconstruct the temporal profile of the pulse by starting from an initial guess and using an iterative algorithm.
Here is a summary of the steps of this algorithm:

1. Given an initial guess $E(t)$, we can gate it with the known $g(t-\tau)$ to obtain $E_{sign}(t,\tau)$.

2. The Fourier transform of this object is $\tilde{E}_{signal}(\omega,\tau)$.

3. Its amplitude can be corrected by using the experimentally-obtained spectrogram:

$$\tilde{E}'_{signal}(\omega,\tau) = \tilde{E}_{signal}(\omega,\tau)\frac{\sqrt{S(\omega,\tau)}}{|\tilde{E}_{signal}(\omega,\tau)|} \tag{A.8}$$

   since $\sqrt{S(\omega,\tau)} = |\tilde{E}_{signal}(\omega,\tau)|$.

4. Through the inverse Fourier transform, we obtain $E'_{signal}(t,\tau)$.

5. Then it is possible to integrate this gated signal over any possible value of τ, knowing that

$$\int E'_{signal}(t,\tau)d\tau = E'(t)\int g(t-\tau)d\tau \tag{A.9}$$

and obtaining the temporal shape $E'(t)$.

6. By comparing this result with the initial guess, the iterative process leads to convergence when they are close enough.

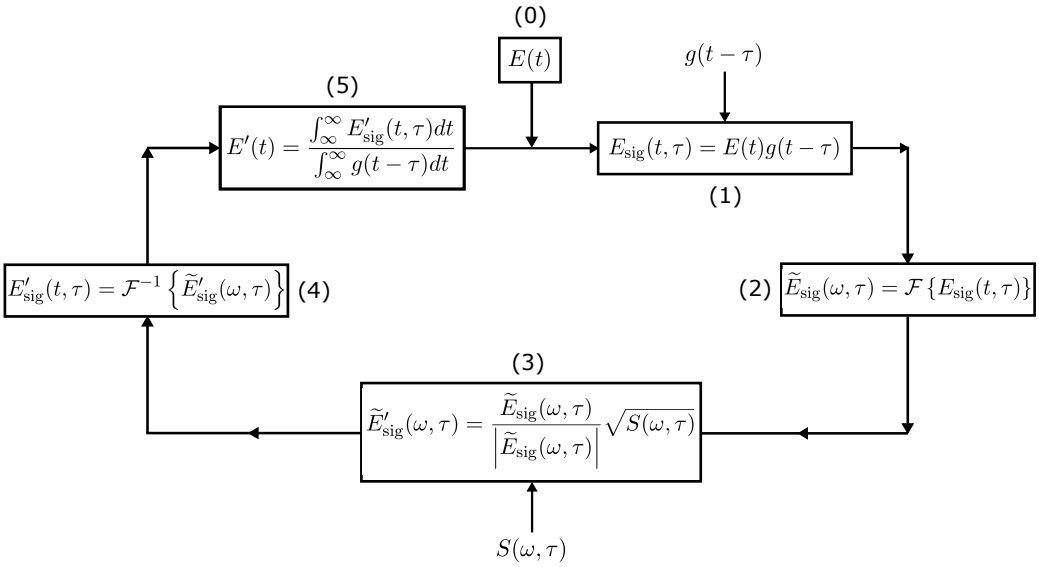

Figure A.1: Iterative algorithm behind FROG. The gate function needs to be known in order to compute point 1), while the experimental spectrogram is used in point 3). Adapted from [5].

Since the shape of the gating pulse can be chosen, several versions of FROG have been implemented. One example is second-harmonic generation (SHG) FROG. Here, a pulse and a delayed replica of itself are focused in a non-collinear way into a $\chi^{(2)}$ crystal, such that they generate their second harmonic. In this case, the electric field of the second harmonic field behaves as:

$$E_{SH}(t,\tau) \propto E(t)E(t-\tau) \tag{A.10}$$

and the spectrogram is:

$$S(\omega,\tau) = \left|\int_{-\infty}^{+\infty} E(t)E(t-\tau)e^{-i\omega t}dt\right|^2 \tag{A.11}$$

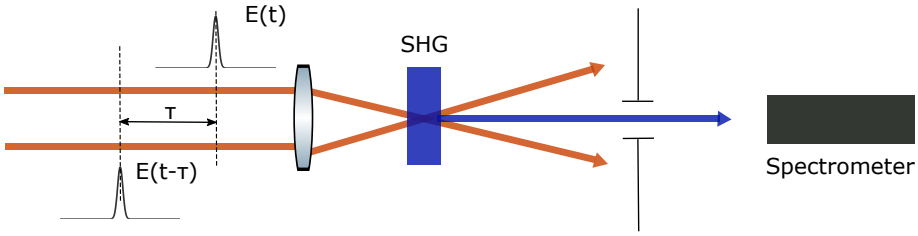

Figure A.2: Sketch of the SHG FROG. The two delayed replica produce a field whose spectrogram depends on the product $E(t)E(t-\tau)$, from which it is possible to retrieve the shape of the pulse.

Then, in this case, the gating pulse is the pulse itself: $g(t) = E(t)$.
The advantages of SHG FROG come from the fact that a $\chi^{(2)}$ process is quite efficient. Anyway, the phase matching bandwidth is proportional to the inverse of the length of the propagation of the beam into the non-linear crystal, setting an upper limit for the thickness of this crystal. Moreover,

$$S(\omega, \tau) = S(\omega, -\tau) \tag{A.12}$$

then this type of FROG can't distinguish between positive and negative chirp.

Appendix B

RABBITT

Reconstruction of Attosecond Beating By Interference of Two-photon Transition (RABBITT) is a technique developed to characterize an attosecond pulse train. It relies on a photoelectron spectrum taken on a noble gas and produced by a pump-probe scheme with an Attosecond Pulse Train (APT) followed by a dressing IR pulse. Since, as discussed in Chapter 1, high-order harmonic generation process can only produce odd harmonics, the spectra produced by just the attosecond pulse train will be of the form of:

$$E = (2q+1)\hbar\omega_{IR} - I_p \tag{B.1}$$

where E is the kinetic energy of the photoelectrons, $2q+1$ is the order of the harmonics and I_p is the ionization potential of the noble gas involved. The photoelectron produced by the XUV pulse can be treated, as a first approximation, as a free particle since $\hbar\omega_{XUV}$ is larger than the ionization potential. Then one or more IR photons, with energy ω_{IR}, can be absorbed producing new lines in the spectrum at energies corresponding to the even harmonics of the fundamental frequency ω_{IR}. These lines are called sidebands (SB) and are the result of a two-photons (or three-photons or more) process of ionization.
By measuring the photoelectron spectrum at different delays between the XUV and IR pulse it is possible to observe, in the sidebands, a periodic behaviour at frequencies which are even multiples of ω_{IR}. This is the result of a quantum interference between two possible equivalent paths leading the electron to the kinetic energy corresponding to a given sideband, and a semiclassical model explaining this result is presented in the next paragraph. The most efficient process, anyway, is the one leading to a $2\omega_{IR}$ oscillation being, as it will be showed, the result of a two-photons process. In this case the observed temporal behaviour will be of the form of:

$$S_{2q} = \alpha + \beta\cos[2\omega_{IR}\tau - \Delta\phi_{2q} - \Delta\theta_{2q}] \tag{B.2}$$

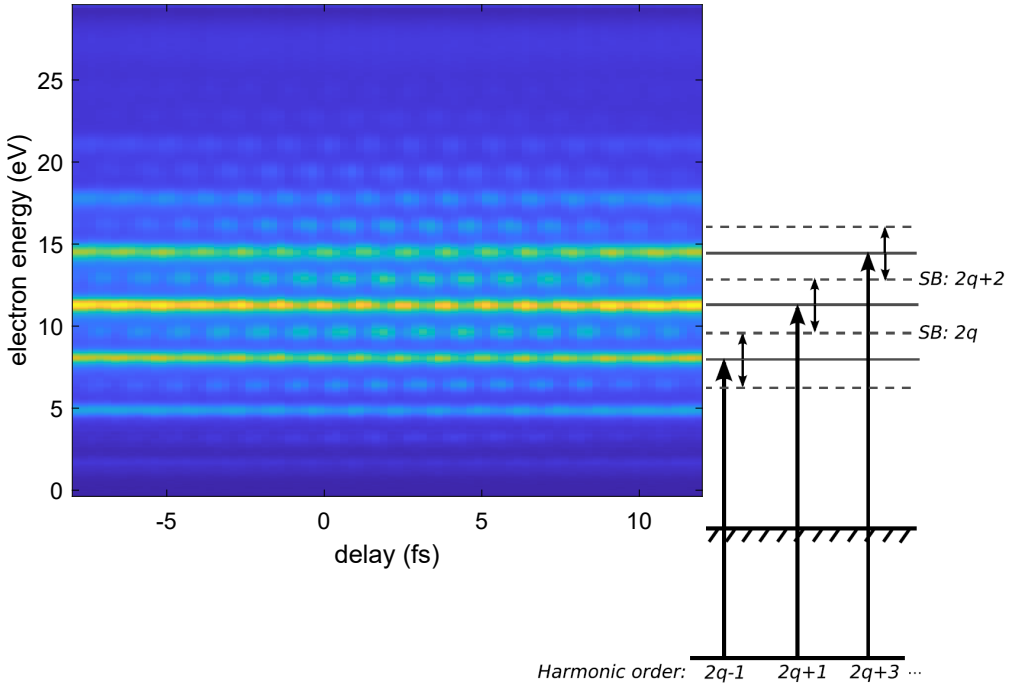

Figure B.1: RABBITT trace of Ar acquired in our laboratory. The energy levels scheme highlights the mainbands (MBs) as levels populated by the odd harmonics of the fundamental one. Multiphoton ionizations can populate the sidebands (SB), where it is also possible to see oscillations along the delay axis. Energy levels scheme adapted from [4].

where τ is the delay between the XUV and IR pulses, $\Delta\phi_{2q} = (phi_{2q+1} - \phi_{2q-1})$ is the phase difference between two consecutive harmonics ($2q-1$ and $2q+1$ multiples of the fundamental frequency) and $\Delta\theta_{2q}$ is an intrinsic atomic quantity, associated to the difference of the phases of the transitions amplitudes associated to the distinct quantum paths leading to the sideband. This last term of phase is interesting since it contains useful information about the shape of the pulse in the APT, as we are going to discuss.
In order to model the phenomenon used in the RABBITT technique, it is useful to follow a semiclassical approach, as discussed by Swoboda et al. [28]. In order to derive the expression of the amplitude of the multi-photon ionization, it is useful to start from the result for the single-photon ionization in a perturbative framework, exploiting the dipole approximation for the light-matter interaction [1]. The time-dependent Schrödinger equation in this case can be written as

$$i\hbar\frac{\partial\psi(\mathbf{r},t)}{\partial t} = \hat{\mathcal{H}}\psi(\mathbf{r},t) \tag{B.3}$$

where

$$\hat{\mathcal{H}} = \hat{\mathcal{H}}_0 + \hat{\mathcal{V}}(t) \tag{B.4}$$

Here, $\hat{\mathcal{H}}_0$ is the free atom hamiltonian and $\hat{\mathcal{V}}(t)$ is the interaction energy with the applied optical field, in the dipole approximation:

$$\hat{\mathcal{V}}(t) = -\hat{\mu}E(t) \tag{B.5}$$

being $\hat{\mu} = -\hat{r}$, in atomic units.
We assume eigenfunctions of free atom hamiltonian to be known, more specifically

$$\psi_n(\mathbf{r}, t) = u_n(\mathbf{r})e^{-i\omega_n t} \quad \text{where} \quad \omega_n = \frac{E_n}{\hbar} \tag{B.6}$$

Here E_n are the eigenvalues of the time-independent Schrödinger equation that is $\hat{\mathcal{H}}_0 u_n(\mathbf{r}) = E_n u_n(\mathbf{r})$. Since these eigenstates form a complete set, it is possible to express the solution to the equation

$$i\hbar\frac{\partial\psi(\mathbf{r}, t)}{\partial t} = (\hat{\mathcal{H}}_0 + \hat{\mathcal{V}})\psi(\mathbf{r}, t) \tag{B.7}$$

as a linear combination of these eigenstates, with a proper weighting coefficient:

$$\psi(\mathbf{r}, t) = \sum_l a_l(t)u_l(\mathbf{r})e^{-i\omega_l t} \tag{B.8}$$

By introducing Eq. B.8 into Eq. B.7, what it is obtained is

$$\begin{aligned} i\hbar\sum_l \frac{da_l}{dt}u_l(\mathbf{r})e^{-i\omega_l t} - i\hbar\sum_l -i\omega_l a_l(t)u_l(\mathbf{r})e^{-i\omega_l t} = \\ = \sum_l a_l(t)E_l u_l(\mathbf{r})e^{-i\omega_l t} + \sum_l a_l(t)\hat{\mathcal{V}}u_l(\mathbf{r})e^{-i\omega_l t} \end{aligned} \tag{B.9}$$

Since E_l in the right hand side of the last equation is clearly equal to $\hbar\omega_l$, two terms cancel each other out. Moreover, by multiplying both sides by $u_m^*(\mathbf{r})$ from the left and integrating over the whole space and making use of the orthonormality condition

$$\int u_m^*(\mathbf{r})u_l(\mathbf{r})d\mathbf{r} = \delta_{ml} \tag{B.10}$$

we obtain the evolution equation for the time-dependent weighting coefficients

$$i\hbar\frac{da_m}{dt} = \sum_l a_l(t)V_{ml}e^{-i\omega_{lm}t} \tag{B.11}$$

with $\omega_{lm} = \omega_l - \omega_m$ and where

$$V_{ml} = \int u_m^*(\mathbf{r})\hat{\mathcal{V}}u_l(\mathbf{r})d\mathbf{r} \tag{B.12}$$

which are the matrix element of the interaction hamiltonian. This equation cannot be solved exactly, so an approximated approach needs to be followed. By using perturbation techniques and thus introducing an expansion parameter λ, we can replace V_{ml} by λV_{ml} and expand $a_m(t)$ as

$$a_m(t) = a_m^{(0)}(t) + \lambda a_m^{(1)}(t) + \lambda^2 a_m^{(2)}(t) + ... \tag{B.13}$$

By equating the same powers of λ on both sides, we obtain a set of equation which connect the N-th order of expansion of the coefficients with the previous, $(N-1)$-th order

$$\frac{da_m^{(N)}}{dt} = \frac{1}{i\hbar}\sum_l a_l^{(N-1)} V_{ml} e^{-i\omega_{lm}t} \quad \text{with} \quad N = 1, 2, 3... \tag{B.14}$$

Now, since the actual incoming pulse has a finite time duration, it can't be described by a monochromatic electric field. The description of a pulse is given by a wave packet. Expressing this wave packet in Fourier series, that is

$$E(t) = \sum_f E(\omega_f) e^{-i\omega_f t} \tag{B.15}$$

we can obtain the expression for the general solution

$$a_m^N(t) = \frac{1}{i\hbar}\sum_f \sum_l \int a_l^{N-1}(t')\mu_{ml} E(\omega_f) e^{-i\omega_f t'} e^{-i\omega_{lm}t'} dt' \tag{B.16}$$

We consider now the specific case of two-photons ionization starting from an atom in ground state. This means that, at $t = 0$, $a_g^0(t) = 1$ while $a_l^0(t) = 0$ for $l \neq g$. We consider the first ionization, given by the XUV pulse, as a first order perturbation, while we will consider the further absorption of the IR photon as a second order perturbation. In this framework, the population of continuum state after perturbing the system with a harmonic frequency can be written as

$$a_n^1(t) = \frac{\mu_{ng} E(\omega_n)}{i\hbar} t \tag{B.17}$$

where μ_{ng} is the transition dipole matrix element from ground state to continuum state and t is the interaction time and gives an approximate value of the pulse duration.

Now, the interaction with the IR pulse can populate both the $n-1$ and the $n+1$ state, and its population can be found by assuming that it is a second order perturbation of the system. By considering, for example, the $n-1$ state, it is found that

$$\begin{aligned} a_{n-1}^{(2)}(t) =& \frac{1}{(i\hbar)^2}\frac{t^(2)}{2}[\mu_{n-1,n-2}\mu_{n-2,g}E(\omega_{IR})E(\omega_{n-2}) \\ &+ \mu_{n-1,n}\mu_{n,g}E(-\omega_{IR})E(\omega_n)] \end{aligned} \tag{B.18}$$

Now, by representing a combination of the various transition dipole moments with a factor M and considering the IR and XUV phase contribution, we get to an approximate expression of the last result:

$$a_{n-1}^{(2)}(t) \approx M\frac{E_{R0}E_{X0}}{(i\hbar)^2}\frac{t^2}{2}[e^{i(\phi_{IR}+\phi_{n-2})} + e^{i(-\phi_{IR}+\phi_n)}] \tag{B.19}$$

Finally, considering the sideband intensity, it will oscillate as

$$I_{n-1}^{(2\omega)} \propto \cos(2\phi_{IR} + \Delta\phi_{n-2,n}) \tag{B.20}$$

Since $\phi_{IR} = \omega_{IR}\tau$ where τ is the delay between the XUV and IR pulses, the oscillation has a frequency equal to $2\omega_{IR}$. As it can be easily showed by doing similar considerations, a three-photons process where two IR photons are involved would introduce a compoonent at $4\omega_{IR}$, a four-photons process a component at $6\omega_{IR}$ and so on; anyway, these processes are way less efficient. As far as $\Delta\phi_{n-2,n}$ is concerned, it is the phase difference between the harmonic spectral phases ϕ_{n-2} and ϕ_n. By retrieving this phase from the experimental photoelectron spectra, it is possible to reconstruct the pulse shape.

Bibliography

[1] Robert W. Boyd. *Nonlinear Optics, Third Edition*. 2008.

[2] J Breidbach and LS Cederbaum. "Migration of holes: Formalism, mechanisms, and illustrative applications". In: *The Journal of chemical physics* 118.9 (2003), pp. 3983–3996.

[3] Francesca Calegari et al. "Ultrafast electron dynamics in phenylalanine initiated by attosecond pulses". In: *Science* 346.6207 (2014), pp. 336–339.

[4] JM Dahlström, Anne L'Huillier and A Maquet. "Introduction to attosecond delays in photoionization". In: *Journal of Physics B: Atomic, Molecular and Optical Physics* 45.18 (2012), p. 183001.

[5] Filippo Daniele and Giacomo Piazza. "Ultrafast dynamics in carbon dioxide measured by using sub-15-fs extreme-ultraviolet pulses". Master's Thesis. Politecnico di Milano, 2019.

[6] Mara Galli. "Real-time tracking of electron dynamics in large molecules". PhD thesis. Politecnico di Milano, 2019.

[7] Holger Hennig, Jörg Breidbach and Lorenz S Cederbaum. "Electron correlation as the driving force for charge transfer: charge migration following ionization in N-methyl acetamide". In: *The Journal of Physical Chemistry A* 109.3 (2005), pp. 409–414.

[8] Jens Herrmann et al. "Multiphoton transitions for delay-zero calibration in attosecond spectroscopy". In: *New Journal of Physics* 17.1 (2015), p. 013007.

[9] David J Jones et al. "Carrier-envelope phase control of femtosecond mode-locked lasers and direct optical frequency synthesis". In: *Science* 288.5466 (2000), pp. 635–639.

[10] Peter M Kraus et al. "Measurement and laser control of attosecond charge migration in ionized iodoacetylene". In: *Science* 350.6262 (2015), pp. 790–795.

[11] Alexander I. Kuleff. "Ultrafast electron dynamics following ionization". Habilitation Thesis. 2012.

[12] Alexander I Kuleff and Lorenz S Cederbaum. "Charge migration in different conformers of glycine: The role of nuclear geometry". In: *Chemical Physics* 338.2-3 (2007), pp. 320–328.

[13] Alexander I Kuleff and Lorenz S Cederbaum. "Ultrafast correlation-driven electron dynamics". In: *Journal of Physics B: Atomic, Molecular and Optical Physics* 47.12 (2014), p. 124002.

[14] Manuel Lara-Astiaso et al. "Attosecond pump–probe spectroscopy of charge dynamics in tryptophan". In: *The journal of physical chemistry letters* 9.16 (2018), pp. 4570–4577.

[15] Franck Lépine, Misha Y Ivanov and Marc JJ Vrakking. "Attosecond molecular dynamics: fact or fiction?" In: *Nature Photonics* 8.3 (2014), p. 195.

[16] Aude Lietard et al. "Characterization of a seeded pulsed molecular beam using the velocity map imaging technique". In: *AIP Conference Proceedings*. Vol. 1786. 1. 2016, p. 060004.

[17] Aude Lietard et al. "Characterization of a seeded pulsed molecular beam using the velocity map imaging technique". In: *AIP Conference Proceedings*. Vol. 1786. 1. 2016, p. 060004.

[18] Matteo Lucchini. "Molecular dynamics imaging bu attosecond pulses". PhD thesis. Politecnico di Milano, 2011.

[19] M. Nisoli et al. "Toward a terawatt-scale sub-10-fs laser technology". In: *IEEE Journal of Selected Topics in Quantum Electronics* 4.2 (1998), pp. 414–420.

[20] Mauro Nisoli, Sandro De Silvestri and Orazio Svelto. "Generation of high energy 10 fs pulses by a new pulse compression technique". In: *Applied Physics Letters* 68.20 (1996), pp. 2793–2795.

[21] Mauro Nisoli et al. "Attosecond Electron Dynamics in Molecules". In: *Chemical Reviews* 117.16 (2017), pp. 10760–10825.

[22] Stefan Pabst et al. "Decoherence in attosecond photoionization". In: *Physical review letters* 106.5 (2011), p. 053003.

[23] François Piuzzi et al. "A simple laser vaporization source for thermally fragile molecules coupled to a supersonic expansion: application to the spectroscopy of tryptophan". In: *Chemical Physics Letters* 320.3-4 (2000), pp. 282–288.

[24] F Remacle et al. "Electronic control of site selective reactivity: a model combining charge migration and dissociation". In: *The Journal of Physical Chemistry A* 103.49 (1999), pp. 10149–10158.

[25] Giuseppe Sansone et al. "Electron localization following attosecond molecular photoionization". In: *Nature* 465.7299 (2010), pp. 763–766.

[26] JP Simons et al. "Bio-active molecules in the gas phase". In: *Physical Chemistry Chemical Physics-Cambridge-Royal Society of Chemistry* (2004), E7–E7.

[27] Donna Strickland and Gerard Mourou. "Compression of amplified chirped optical pulses". In: *Optics communications* 56.3 (1985), pp. 219–221.

[28] Marko Swoboda et al. "Intensity dependence of laser-assisted attosecond photoionization spectra". In: *Laser physics* 19.8 (2009), pp. 1591–1599.

[29] Minh-Huong Ha-Thi et al. "An efficient indirect mechanism for the ultrafast intersystem crossing in copper porphyrins". In: *The Journal of Physical Chemistry A* 117.34 (2013), pp. 8111–8118.

[30] Andrea Trabattoni. "Attosecond electron dynamics in complex molecular systems". PhD thesis. Politecnico di Milano, 2014.

[31] Rick Trebino et al. "Measuring ultrashort laser pulses in the time-frequency domain using frequency-resolved optical gating". In: *Review of Scientific Instruments* 68.9 (1997), pp. 3277–3295.

[32] R Weinkauf et al. "Elementary processes in peptides: electron mobility and dissociation in peptide cations in the gas phase". In: *The Journal of Physical Chemistry* 99.28 (1995), pp. 11255–11265.